Metals and Ceramics Division

Heavy Vehicle Propulsion Materials Program
Quarterly Progress Report for
October through December 2005

D. R. Johnson
Technical Project Manager

Prepared for
U.S. Department of Energy
Assistant Secretary for Energy Efficiency and Renewable Energy
Office of FreedomCAR and Vehicle Technologies Program
VT 05 01 020

Prepared by the
OAK RIDGE NATIONAL LABORATORY
Oak Ridge, Tennessee 37831-6066
Managed by
UT-Battelle, LLC
for the Department of Energy
Under contract DE-AC05-00OR22725

CONTENTS

Materials for Advanced Fuel Systems

Mechanical Reliability of Piezo Stack Actuators (ORNL)

Coating Technology for Complex Shapes (ORNL)

Materials for Exhaust Aftertreatment

Materials for Exhaust Aftertreatment (Caterpillar Inc.)

Characterization of Catalyst Microstructures and Deactivation Mechanisms (ORNL)

NO_x Sensor Development (ORNL and Ford Motor Company)

Catalysis via First Principles (ORNL)

Durability of Diesel Engine Particulate Filters (ORNL and Cummins, Inc.)

NO_x Reduction Technology by Urea SCR (ORNL)

Materials for Air Handling and Thermal Management

Austenitic Stainless Steel Alloys for Exhaust Manifold (ORNL and Caterpillar Inc.)

Friction and Wear Reduction in Diesel Engine Valve Trains (ORNL)

Materials for Structural Components

Advanced Machining and Sensor Concepts (University of Michigan)

Synergistic Process-Enhanced Grinding (ORNL)

Materials for Hot Section Components

NDE of Diesel Engine Components (Argonne National Laboratory)

Life Prediction of Diesel Engine Components (ORNL and Caterpillar)

Engineered Surfaces for Diesel Engine Components (Caterpillar)

Lightweight Valve Train Materials (Caterpillar Inc.)

Engineered Modification of Ceramics (NIST)

Characterization of Physical and Mechanical Properties

Testing Standards (NIST)

IEA Annex on Materials for Transportation Applications (ORNL)

IEA – Rolling Contact Fatigue (ORNL)

Emerging Technologies

Mechanical Characterization - Nanoengineered Materials (North Carolina A&T State University)

Nanocrystalline Materials via Machining (Purdue University)

Deformation Processes for the Next Generation Ceramics (ORNL)

Mechanical Reliability of PZT Piezo-Stack Actuators

A. A. Wereszczak and H. Wang
Oak Ridge National Laboratory

Objective/Scope

The use of piezoelectric stack actuators as diesel fuel injectors has the potential to reduce injector response time, provide greater precision and control of the fuel injection event, and lessen energy consumption (e.g., for use in homogeneous charge compression ignition, HCCI, engines). Though piezoelectric function is the obvious primary function of lead zirconium titanate (PZT) ceramic stacks for fuel injectors, their mechanical reliability can be a performance and life limiter because PZT is both brittle, lacks high strength, and may exhibit fatigue (i.e., slow crack growth) susceptibility. That brittleness and relatively low strength can be overcome with proper design though. This project combines in-situ micromechanical testing, microstructural-scale finite element analysis, probabilistic design sensitivity, and structural ceramic probabilistic life prediction methods to systematically characterize and optimally design PZT piezoelectric stack actuators that will enable maximized performance and operational lifetime.

Technical Highlights

The goal for diesel fuel injectors is to achieve maximum stroke within the electric, thermal, and mechanical limitations of the piezoceramics comprising the piezo stack. PZT-5A (or equivalent "soft PZTs") piezoceramics are desirable candidates for the piezostacks because they tend to have an inherently high charge constant and Curie temperature of ~ 400 pC/N and 340°C, respectively.

Acquisition of materials and consideration of existing CerSaT test instrumentation is underway. Soft PZTs are being acquired and their physical properties determined. Microstructural examination and fractography is planned to identify potential strength- and fatigue-limiting flaw populations. The interfacing of a piezo linear amplifier (used to drive small and large piezo stacks) with a universal test machine, dynamic indentation tester, and resonant ultrasound spectroscope is underway.

Discussions are underway to partner the project with a diesel engine manufacturer. Characterization, reliability analysis, and ultimately performance predictability of piezostacks is also a focus of this project, but having direct guidance from a manufacturer will ensure that our R&D has relevance.

Status of FY 2006 Milestones

Create and develop a general finite element model that predicts operational stresses in a PZT piezo stack actuator and that enables probabilistic life prediction estimation. [09/06]
On schedule.

Communications/Visits/Travel

Interest to visit UCLA's G. Carman exists to discuss his group's work on piezoceramics and identify means to collaborate.

Publications
None.

References
None.

Coating Technology for Complex Shapes

T. N. Tiegs, D. C. Harper, F. C. Montgomery, J. O. Kiggans, and C. A. Blue
Oak Ridge National Laboratory

Objective/Scope

High Density Infrared (HDI) technology is relatively new to the materials processing area and is gradually being exploited in materials processing. For many applications in heavy-duty vehicles, superior properties, such as corrosion and wear resistance, are only required at the material surface. The project using HDI technology will be exploratory and will examine the application of wear-resistant coatings based on hard-metal type compositions.

Technical Highlights

Earlier work had shown that adherent coatings of hardmetal compositions could be applied to a variety of metal substrates (D-2 tool steel, 4140 alloy steel, and cast iron). As reported previously, samples were fabricated that used ceramic particles only (e.g. WC or TiC) for the coating with no binder addition. The idea was that the sintering temperature for these plain carbides is significantly higher than the melting point of the substrates. Consequently, because no binder additions (i.e. Ni or Ni_3Al) are present, sintering and cracking would be inhibited, which was a problem with earlier samples. Finally, this would allow the coating to heat up to a sufficiently high temperature so that the underlying substrate would melt and be wicked into the coating by capillary action.

Previous testing showed a significant improvement of the hardness in the as-fabricated coatings with WC-Co. Additional examinations of coatings with alternate binders were done to correlate coating process parameters with the alternate binders. Hardness results for WC-Ni and WC-Ni_3Al coatings are shown in Figs. 1and 2. As observed previously, for the same coating composition, differences in hardness were observed for the three different metal substrates. Evidently, the mixing effects between the substrate and the coating during the high temperature HDI exposure have a significant effect on the hardness and are different for the different binders. Co does not readily form compounds with Fe. However, Ni and Al readily react with Fe to form a series of intermetallics. The observed high hardness at the coating-substrate interface with the Ni and Ni_3Al binders indicate the formation of intermetallics that would contribute to the hardness.

Status of Milestones

Because of budget constraints, the project was terminated after the first quarter.

Communications/Visits/Travel

None.

Problems Encountered

None.

Publications

T. N. Tiegs, F. C. Montgomery, D. C. Harper, and J. O. Kiggans, "Ceramic-Based Coatings On Metals Bonded By High Intensity Infrared Heating," to be published in Ceram. Eng. Sci. Proc., Am. Ceram. Soc., Westerville, OH (2006)

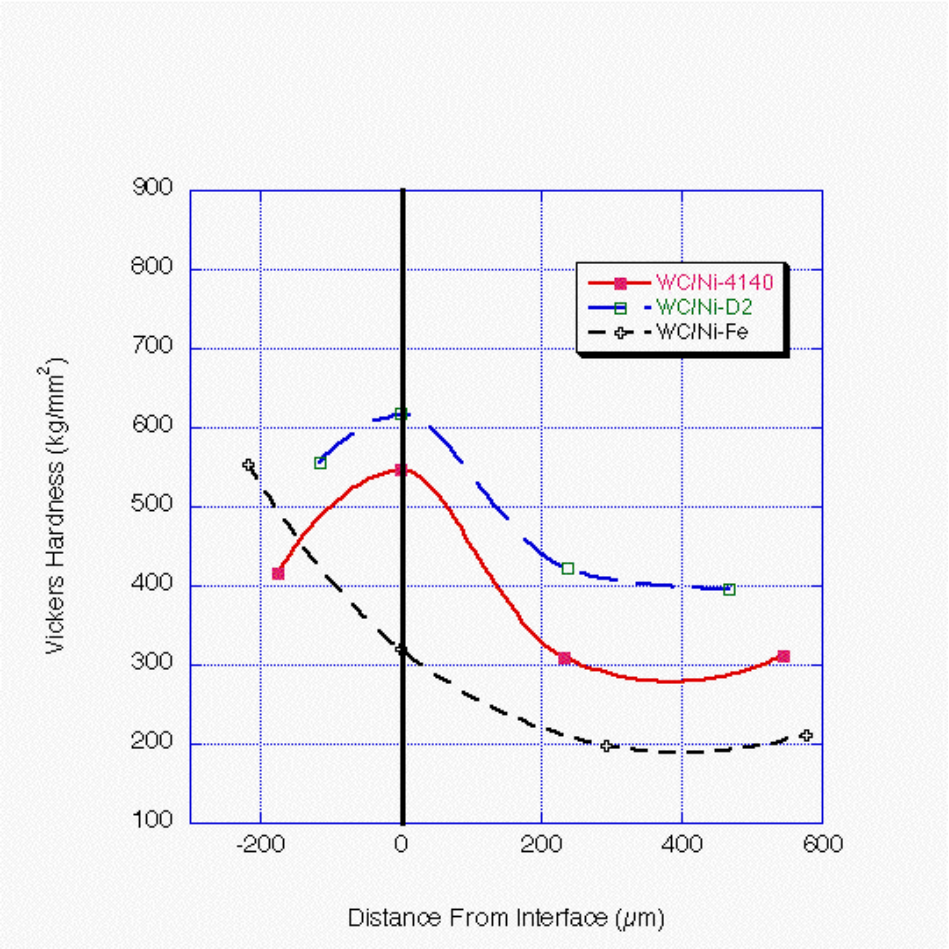

Fig. 1. Hardness improvements with HDI-treated WC-Ni surface coatings on 4140 alloy steel, D2 tool steel and cast iron.

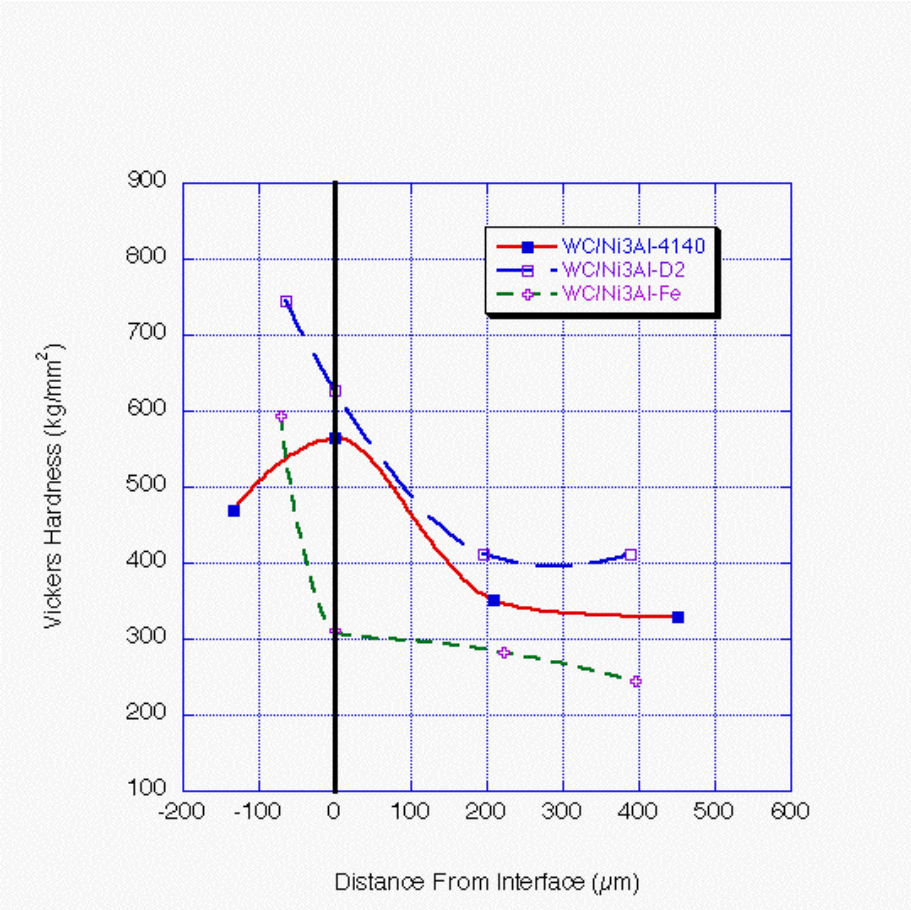

Fig. 2. Hardness improvements with HDI-treated WC-Ni_3Al surface coatings on 4140 alloy steel, D2 tool steel and cast iron.

Materials for Exhaust Aftertreatment

Corey Shannon, Herbert DaCosta, Matt Stefanick, Ron Silver and Craig Habeger
Caterpillar Inc.

Objective/Scope

The objective of the effort is to develop and evaluate materials that will be utilized in aftertreatment systems for diesel engine applications. These materials include catalysts for CO and hydrocarbon oxidation, NOx reduction, and filtration media to improve particulate abatement capabilities in the exhaust system. The project is a part of Caterpillar strategy to meet EPA requirements for regulated diesel emissions in 2010 and beyond.

This year's focus is to assess durability of various catalyst technologies in terms of phosphorous, sulfur and thermal degradation, and to identify diesel particulate trapping materials that have high durability and filtration efficiency to comply with future emission regulations for heavy-duty diesel engines.

Technical Highlights

Diesel Particulate Filter (DPF)

A catalyzed diesel particulate filter (DPF) obtained from a supplier was loaded with particulate matter on the diesel fuel-burner bench and regenerated. This process was repeated three times on the filter to determine regeneration efficiency, Figure 1a. Results are inconclusive as only one DPF was tested in this manner. However, trends can be seen from this test: filtration efficiency decreases and backpressure increase slightly after DPF regeneration, Figure 1b.

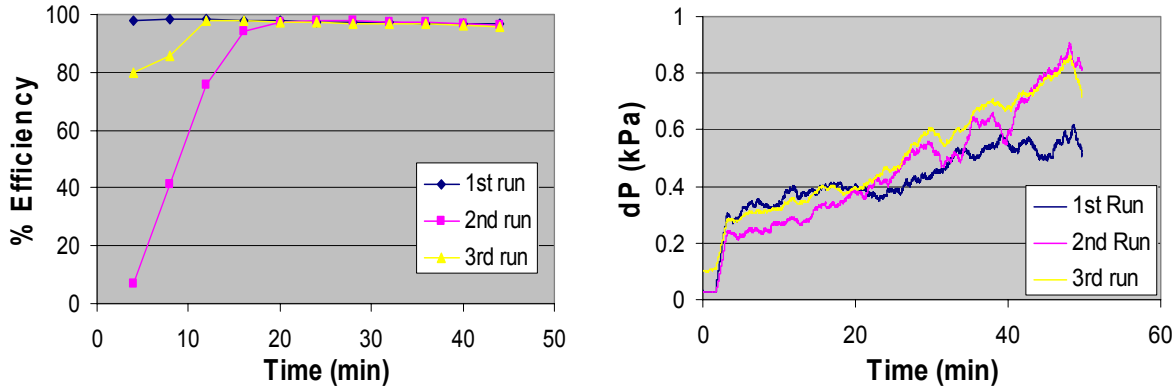

a) b)

Figure 1. a) The test repeatability of filtration efficiency of the DPF; b) the backpressure as a function of time for the same three filtration tests

Plans for the next quarter include the continuation of thermal durability and regeneration efficiency tests on the DPF materials.

Catalyst Durability

Oxicat durability:

A set of oxidation catalysts (oxicats) were evaluated for CO and HC lightoff performance before and after aging via phosphorus exposure using a diesel fuel burner. The phosphorus had only a mild effect on the oxicat activity, with the worst impact being a 20°C increase in CO lightoff after an exposure of 19 g/L P. The lightoff curves shifted toward higher temperature with increasing phosphorus exposure without changing shape, which is typical of a decline in activity due to physical blockage of active sites. The results were compared to previous tests that measured the P effect on NOx reduction over Lean NOx Traps (LNTs) and Selective Catalytic Reduction (SCR) catalysts. CO and HC oxidation over the tested catalysts are affected by phosphorus to about the same extent as NOx reduction over SCR catalysts. Phosphorus impacts LNT performance more than either oxicats or SCRs.

Results in Figures 2a and 2b respectively show the effect of phosphorus (P) exposure on the HC and CO lightoff performance of a Pt catalyst. The lightoff temperature (T_{50}, the temperature at which 50% conversion is obtained) of the catalyst increased by about 8°C for HC and 15°C for CO when exposed to 5.5 g/L P. The lightoff temperatures increase with increasing exposure levels of P. A second catalyst core was exposed to 3.6 g/L P, and results are in line with those from the first core. All of the samples, which were aged in the lab on the diesel fuel burner, have lightoff curves that are similar in shape to the fresh benchmark. The shift in the curves with increasing phosphorus is typical of a decline in activity due to physical blockage of active sites. Most likely, the accumulated P blocks some of the sites where HC or CO is adsorbed. The actual P concentration that a catalyst will see is a function of the catalyst volume, the concentration of P in the oil, and the engine oil consumption rate.

The impact of P on oxicats was compared to its effect on Lean NOx Traps (LNTs) and Selective Catalytic Reduction catalyst (SCR). First the temperature for 90% CO conversion over the fresh catalyst was obtained, then amount of CO converted at that same temperature for a P aged catalyst was determined. The procedure was repeated for each level of P exposure, and then again for the HC. Results for LNT and SCR catalysts were determined based on fresh vs. aged NOx reduction. Oxicat conversion of CO and HC is affected by P to about the same extent as NOx reduction over vanadia based or zeolite SCR catalysts. The impact of P on LNTs is greater than that for oxicats or SCRs. In all cases, P is physically blocking adsorption sites.

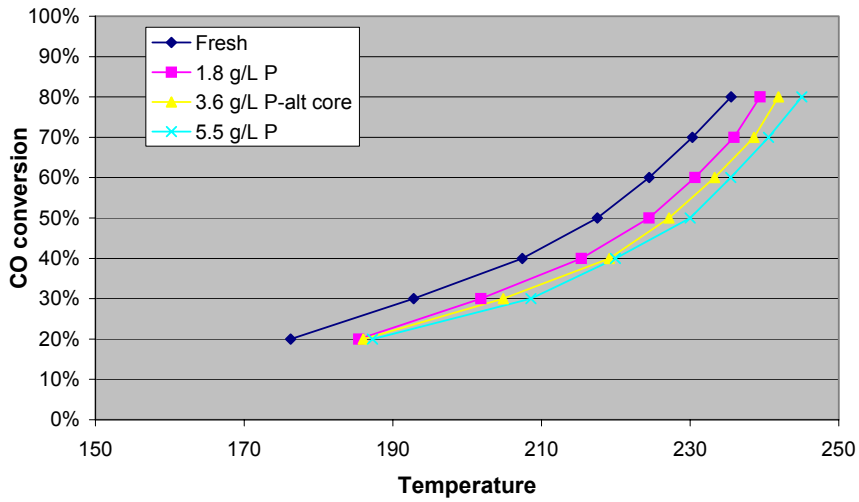

a)

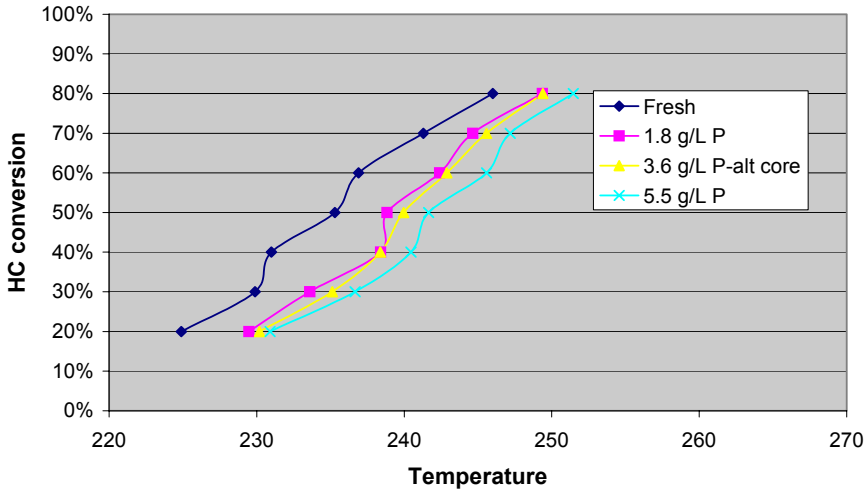

b)

Figure 2. The effect of phosphorus (P) exposure on the (a) COand (b) HC lightoff performance of a Pt catalyst.

Plans for the next quarter include a comparison of the impact of equivalent concentrations of phosphorus exposure (grams phosphorus exposed/liter catalyst) on catalyzed DPFs.

Future Plans

1. Continue searching for and testing new substrate materials for DPF filters.
2. Load samples of catalyzed DPFs with varying levels of P to determine durability relative to fresh performance.
3. Age SCR catalysts with a combination of P, sulfur and thermal aging to determine impact on durability.

Travel

None

Presentations/Publications

None

Status of FY 2006 Milestones

1. Tested 1" x 3" core samples un-catalyzed and catalyzed DPF for soot regeneration.
2. The durability study of various catalyst technologies (oxidation catalyst, NOx adsorber and urea-SCR) for P and S degradation has been progressed as scheduled.

Characterization of Catalyst Microstructures and De-activation Mechanisms

L. F. Allard, D. A. Blom, C. K. Narula, M. A. O'Keefe, J. Hoard, and M. Jose-Yacaman
Oak Ridge National Laboratory

Objective/Scope

The objective of the research is to characterize the microstructures of catalyst materials of interest for the treatment of NO_x emissions in diesel and lean-burn gasoline engine exhaust systems. The research heavily utilizes new capabilities and techniques for ultra-high resolution transmission electron microscopy with the HTML's aberration-corrected electron microscope. The research is focused on understanding the effects of reaction conditions on the changes in morphology of heavy metal species on "real" catalyst support materials (typically oxides), and the understanding of the structures of model mono-, bi- and multi-metallic catalyst systems of known particle composition. With the former systems, these changes are being studied utilizing samples treated in both steady-state bench reactors and a special *ex-situ* catalyst reactor system especially constructed to allow appropriate control of the reaction. Model samples of nanoparticles of controlled composition on carbon or oxide supports are also being studied in collaboration with the catalysis group at the University of Texas-Austin (Prof. M. Jose-Yacaman and students).

Technical Progress

The understanding of the way in which matter organizes into clusters with thousands of atoms is one of the most important and challenging problems in catalysis and nanotechnology. When two species of atoms with different radii are involved, the expected packing will be more complicated. A number of structures are anticipated, ranging from quasicrystals and amorphous crystals to well-ordered superlattices and core-shell structures [1]. A number of these structures has been predicted by theoretical calculations and observed by a number of authors [2], and it is one of the most active and fascinating topics in nanotechnology. It has been known for several years that the addition of a second metal into monometallic nanoparticles significantly changes some of their properties, e.g. optical properties, catalytic properties, electronic properties, etc. [3-7]. When two or more different elements compose one nanoparticle, the differences in atomic radii are going to influence the way the atoms organize into a crystal. However, very little is known about the crystal structure of bimetallic nanoparticles in the size regime from 0.5 to 2nm [5]. For bimetallic nanoparticles composed of a noble metal and a transition metal, recent experimental results indicate that an icosahedral phase structure is preferred over the others [6]. In the present work, Prof. Yacaman and his group are conducting a complete study of the structure, size, shape, optical response and catalytic properties of single, bimetallic and multimetallic nanoparticles. In collaboration with our lab at ORNL, we are systematically studying nanoparticles of Au, Ag, Pt, Pd and their alloys, which are the most interesting systems because of their catalytic applications.

The comparatively low melting point of gold (1064°C) compared with platinum (1769°C) probably means that the material is *not* suitable for use in three-way catalysts that operate at high temperatures (typically >600°C) of stoichiometric-burn exhausts in under-floor catalyst positions, and even less so in close-coupled catalyst positions (~1000°C). However, low

temperature start-up performance of catalysts remains an area in which improvement is sought. PGM-based TWCs lack low temperature start-up, as well as suffering prolonged idling problems, resulting in the catalyst monolith not operating until the light-off temperature (~300°C) required for oxidation of hydrocarbons is attained. Gold-based catalysts have the ability to be active at relatively low temperatures and can potentially be used in conjunction with the TWC in automotive catalyst systems to overcome this cold engine problem. In addition, Au-based catalysts have shown activity for the lean-burn reduction of NO_x at both high and relatively low temperatures. Some interesting results of our studies of Au-Pd nanoparticles using the ACEM are presented below.

Figure 1a shows a HA-ADF image of a nanoparticle of AuPd (1:1 in atomic composition), supported on a uniformly thin carbon film, in which surface roughness is observed; that roughness is consistent with DFT calculations of similar particles, e.g. one shown in Fig. 1b. This particle's structure developed as a result of simulated heating of a well-ordered AuPd decahedral particle having roughly 500 atoms (Fig. 1c), with subsequent rapid cooling. Both particle and calculations were obtained in conditions of rapid cooling similar to those that are used in real catalysis. Such computations allow the prediction of complex surface structures that can be active sites for a number of different reactions. The experimental particle image of Fig. 1a suggests a strong match to the model structure.

Figure 2b is an intensity trace over the row of atoms as indicated in Fig 2a. A profile over a single (presumed Pd) atom on the carbon film indicated a peak intensity above background of 400 counts. The discrete jumps of this intensity suggest integral numbers of atoms in the respective columns, but the central intensity peak, if all Pd, represents an unreasonable number of Pd atoms extending above the general surface, so it is likely that one or more Au atoms contribute to the intensity of this column. Full STEM image calculations of a model particle structure taking into account Au and Pd concentrations to match the experimental images should clarify the structure.

Status of Milestones
On schedule

Communications/Visits/Travel
None this period

Publications
None

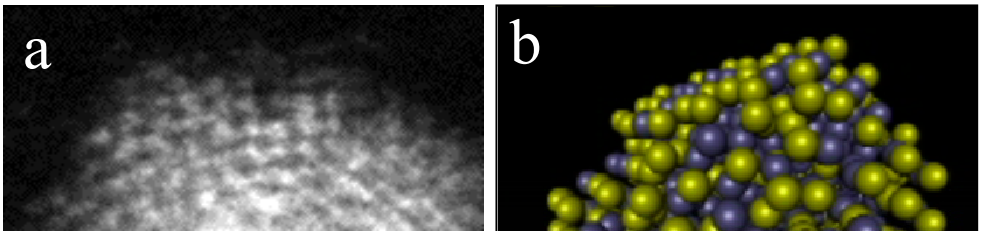

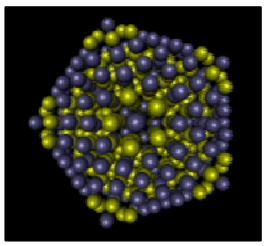

Fig. 1.a) HA-ADF image of particle with nominal Au1Pd1 composition. b) DFT computation of Au1Pd1 nanoparticle, originally created as a perfectly ordered multiply-twinned particle, then heated to 1000K and cooled to RT. The latter, disordered, configuration is a reasonable match to the observed particle, with numerous irregular surface sites.

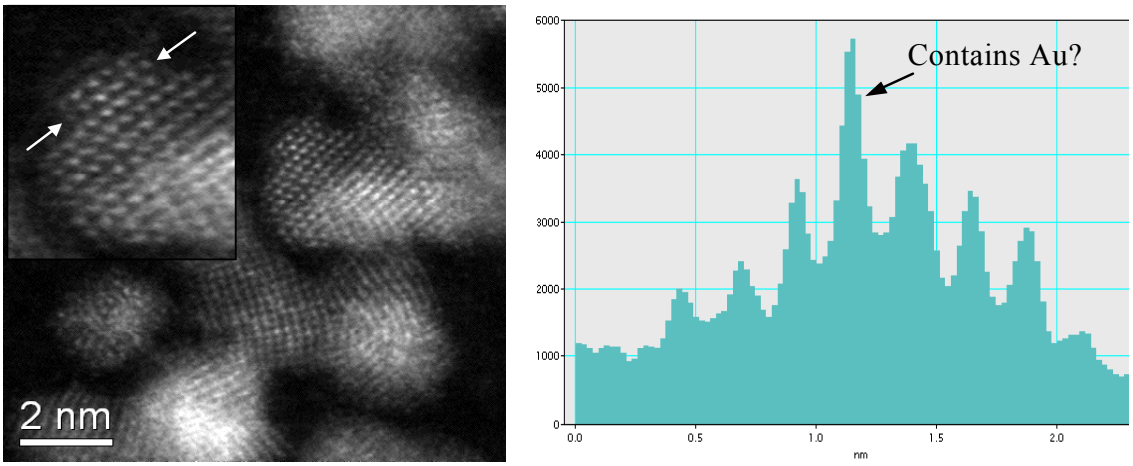

Fig. 2.a) HA-ADF image of Au1Pd5 nanoparticles. b) Profile of intensity of atom row indicated in the inset image of (a). The height of the central atom column suggests one or more Au atoms must be present in the column. Image smoothed using a 3 x 3 low-pass filter.

References

[1] D. Enache et al. *Science*, **311**, 362 (2006)
[2] R. Pratti and M. Rossi, *J. Catalysis* **176**, 552 (1998)
[3] A.M. Venezia, V. La Parola, V. Nicolì and G. Deganello, *J. Catalysis* **212**, 56-62 (2002)
[4] L. Guczi, et al., *Surface and Interface Analysis*, **34**(1) 72-75 (2002)
[5] J.L. Rodriguez-Lopez J.L., et al., *Physical Review Letters* **92**(19) 2004
[6] M. Jose-Yacaman, et al., *J.Vac. Sci. & Tech. B*, **19**(4) 1091-1103 2001
[7] J.L. Rodriguez-Lopez, J.M. Montejano-Carrizales and M. J. Yacaman, *Appl. Surf. Sci.*, **219**(1-2) 56 (2003)

NO_x Sensor Development

David L. West, Fred C. Montgomery and Timothy R. Armstrong
Oak Ridge National Laboratory

CRADA No. ORNL 01-0627
with Ford Motor Company

Objective

The proposed project seeks to develop technologies and materials that will facilitate the development of NO_x and ammonia sensors. The development of low-cost, simple NO_x will facilitate the development of ultra-low NO_x emission engines, directly supporting the OHVT goals.

Technical Highlights

There were three main technical highlights:

1. A new electrode architecture with was developed that appeared to significantly reduce drift during long term operation. Some sample results are presented in Fig. 1, which shows the change in measured resistance over ~40 hr. of simulated operation at 600 ^{o}C. The new architecture ("Improved design") displays a remarkably stable resistance in comparison to that observed with the original architecture.

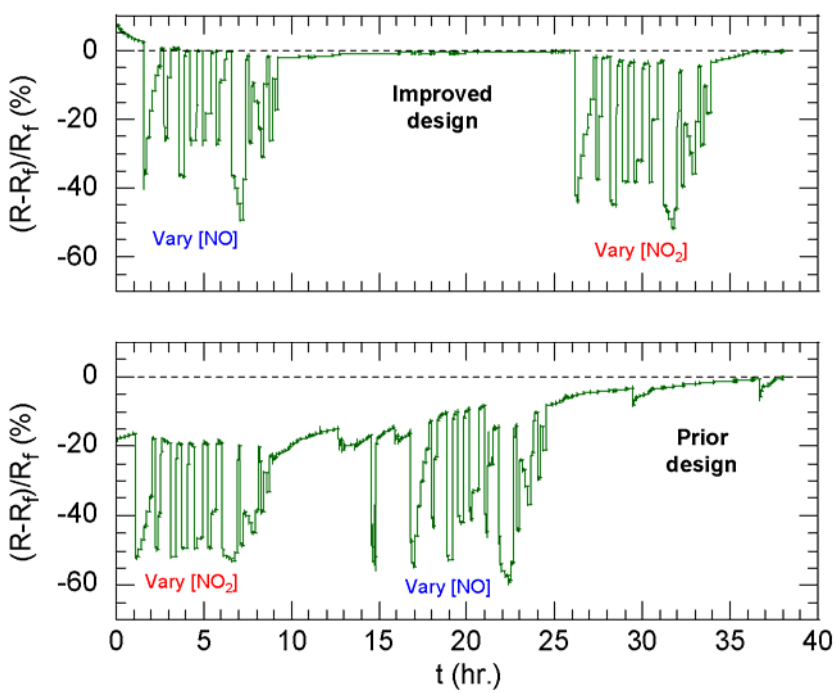

Figure 1: Drift observed during long-term operation at 600°C and 10°C dewpoint.

2. Pursuant to the CRADA partner's (Ford) decision to adopt selective catalytic reduction (SCR) as the go-forward NO_x remediation strategy we have begun to characterize element responses to NH_3. [The SCR system will react NO_x with NH_3 (derived from urea hydrolysis); therefore, the behavior of these sensing elements in the presence of NH_3 is of concern.] Figure 2a shows that at certain levels of applied electrical stimulus the response to NH_3 can be minimized. Unfortunately, as Fig. 2b shows, this level of applied electrical stimulus does not correspond to the "total NO_x" condition.

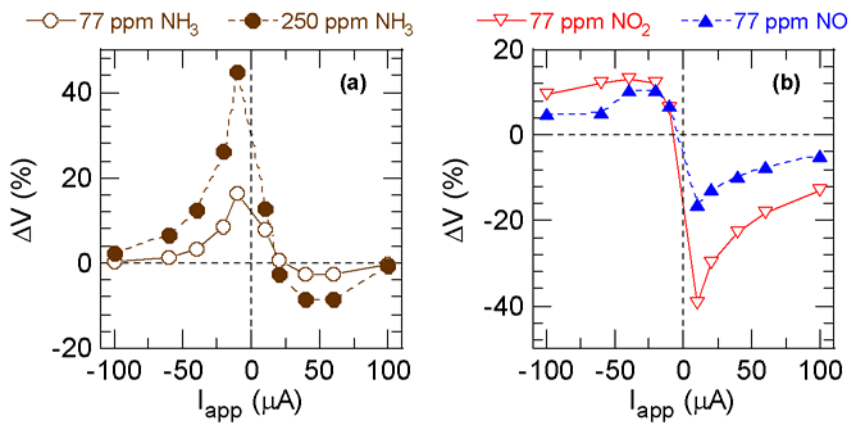

Figure 2: Effect of applied current on responses to NH_3 (a) and NO_x (b). Data collected at 650°C, 7 vol % O_2, 10°C dew point.

3. The capability to add the potential interferents CO and C_3H_6 (a representative hydrocarbon) was added to the test system.

Future Plans

- Fully characterize the cross-sensitivity of these sensing elements to CO, C_3H_6, and H_2O
- Modify existing test rig so that higher moisture concentrations (diesel exhaust is typically 3–12% H_2O) can be obtained.
- Investigate extending the processing window of the new electrode architecture to higher temperatures. (The new electrode architecture uses an Ag-Pd alloy that cannot be processed at temperatures > 950°C
- Supply prototype elements to Ford for use in dyno testing

Status of FY2006 milestones

(1) Detailed understanding of sensing mechanism **(01/06)**
Samples have been supplied to both GA Tech (IR, Raman spectroscopy) and to Northwestern University (impedance spectroscopy).

On track.

(2) Evaluate cross-sensitivities, including H_2O from 1 to 10 vol%. **(06/06)**.
Six-port mixing unit has been set up, and higher humidity addition systems are being evaluated currently.

On track.

(3) Evaluate stability in real exhausts. **(03/06)**.

Dyno testing is currently being set up at Ford SRL.

On track.

(4) Investigate use of time-varying electrical stimulus (**06/06**).

Preliminary results did not indicate that signal stability was enhanced with this technique.

Completed (12/05)

Communications/Visits/Travel

- Biweekly teleconferences were held with LLNL and Ford during the quarter.
- Meeting was held with Thom Orlando (Georgia Tech) in November 2005 to review Georgia Tech's progress on characterizing surface NO_x reactions with Raman and IR spectroscopy.

Problems Encountered

None

Publications

None

Intellectual Property Filed

- "$LaCrO_3$ electrodes for NO_x sensing elements," IDEAS #05-55 filed October 2005.

References

[1] J. Kašpar, P. Fornasiero, and N. Hickey, "Automotive catalytic converters: Current status and some perspectives," *Catalysis Today* **77**, 419–449, 2003.

Catalysis via First Principles

C. Narula, W. Shelton, Y. Xu, M. Moses, D. Blom and L. Allard
Oak Ridge National Laboratory

Objective/Scope

This research focuses on an integrated approach between computational modeling and experimental development, design and testing of new catalyst materials, that we believe will rapidly identify the key physiochemical parameters necessary for improving the catalytic efficiency of these materials. The results will have direct impact on the optimal design, performance, and durability of supported catalysts employed in emission treatment; e.g., lean NO_x catalyst, three-way catalysts, oxidation catalysts, and lean NO_x traps etc.

The typical solid catalyst consists of nano-particles on porous supports. The development of new catalytic materials is still dominated by trial and error methods, even though the experimental and theoretical bases for their characterization have improved dramatically in recent years. Although it has been successful, the empirical development of catalytic materials is time consuming and expensive and brings no guarantees of success. Part of the difficulty is that most catalytic materials are highly non-uniform and complex, and most characterization methods provide only average structural data. Now, with improved capabilities for synthesis of nearly uniform catalysts, which offer the prospects of high selectivity as well as susceptibility to incisive characterization combined with state-of-the science characterization methods, including those that allow imaging of individual catalytic sites, we have compelling opportunity to markedly accelerate the advancement of the science and technology of catalysis.

Computational approaches, on the other hand, have been limited to examining processes and phenomena using models that had been much simplified in comparison to real materials. This limitation was mainly a consequence of limitations in computer hardware and in the development of sophisticated algorithms that are computationally efficient. In particular, experimental catalysis has not benefited from the recent advances in high performance computing that enables more realistic simulations (empirical and first-principles) of large ensemble atoms including the local environment of a catalyst site in heterogeneous catalysis. These types of simulations, when combined with incisive microscopic and spectroscopic characterization of catalysts, can lead to a much deeper understanding of the reaction chemistry that is difficult to decipher from experimental work alone.

Thus, a protocol to systematically find the optimum catalyst can be developed that combines the power of theory and experiment for atomistic design of catalytically active sites and can translate the fundamental insights gained directly to a complete catalyst system that can be technically deployed.

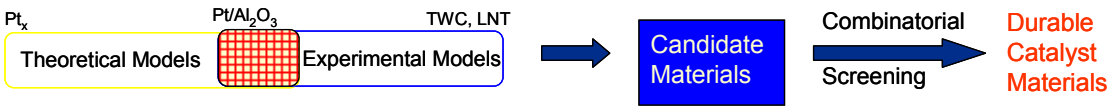

Although it is beyond doubt computationally challenging, the study of surface, nanometer-sized, metal clusters may be accomplished by merging state-of-the-art, density-functional-based,

electronic-structure techniques and molecular-dynamic techniques. These techniques provide accurate energetics, force, and electronic information. Theoretical work must be based electronic-structure methods, as opposed to more empirical-based techniques, so as to provide realistic energetics and direct electronic information.

A computationally complex system, in principle, will be a model of a simple catalyst that can be synthesized and evaluated in the laboratory. It is important to point out that such a system for experimentalist will be an idealized simple model catalyst system that will probably model a "real-world" catalyst. Thus it is conceivable that "computationally complex but experimentally simple" system can be examined by both theoretical models and experimental work to forecast improvements in catalyst systems.

Our goals are as follows:

- Our theoretical goal is to carry out the calculation and simulation of realistic Pt nanoparticle systems (i.e., those equivalent to experiment), in particular by addressing the issues of complex cluster geometries on local bonding effects that determine reactivity. As such, we expect in combination with experiment to identify relevant clusters, and to determine the electronic properties of these clusters.
- Our experimental goal is to prepare and characterize metal carbonyl clusters, decarbonylated metal clusters, sub-nanometer metal particles, and metallic particles (~5 nm) on alumina (commercial high surface area, sol-gel processed, and mesoporous molecular sieve). The characterization of such catalyst is now possible with the availability of ACEM at ORNL. We will then evaluate these systems for CO conversion efficiencies to determine the species that participates in CO oxidation catalysis.
- This approach will allow us to identify the catalyst sites that are responsible for CO, NOx, and HC oxidation. We will then address support-cluster interaction and design of new durable catalysts systems that can withstand the prolonged operations.

Technical Highlights

In the previous report, we summarized theoretical modeling is based on DFT studies of Pt clusters to understand the relationship between cluster size, structure, composition, and reactivity. This coupled with first-principles thermodynamics provides insights into the effects of oxidizing atmosphere (O_2) – finite (T, p_{O_2}), structure, composition, redox potential on particle size. The results provide guidance for investigations of larger / supported clusters. The next steps of this work will model supported clusters, based on input from experimental results, and their interactions with CO, NO_x, and HC.

Experimentally, we reported the synthesis a series of Pt and Re clusters and particles supported on morphologically different γ–aluminas. The microstructural characterization reveals structural differences in 1-3 atom, 10-20 atom, and larger (1.5nm and above) clusters. We have initiated evaluation of these catalysts for their CO, oxidation capability and we plan to evaluate NO_x, and HC oxidation capability also. Guided by the theoretical models and experimental results, we will synthesize new set of catalyst materials with higher durability under operating conditions.
Our results on theoretical and experimental work are summarized in following paragraphs.

Platinum-Alumina System:
As reported previously, we synthesized Pt/γ–alumina clusters by impregnation of γ–alumina with $H_2PtCl_6 \bullet 6H_2O$ followed by calcinations in air at 500ºC. High magnification images obtained using the ACEM in the HAADF-STEM mode indicate the atomic make up of these 1-1.5 nm particles and confirm the presence of smaller platinum clusters, see Figure 1. Theoretical models suggest that Pt particle in this size range are different from bulk particles and are partially oxidized. However, there might be some clusters with at least one metallic atom.

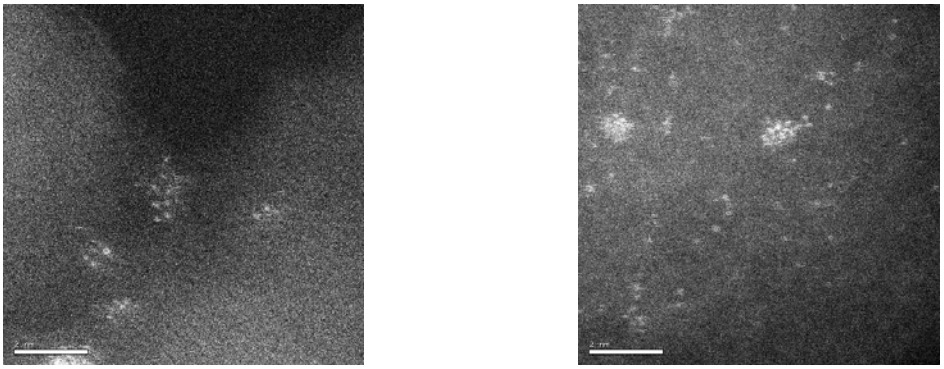

Figure 1: ACEM HAADF-STEM images of 2% Pt/ γ-Al_2O_3

We evaluated a sample of this catalyst employing a new reactor that was installed and became operational in the last quarter. This reactor is specially designed for ethane oxidative dehydrogenation reactions.

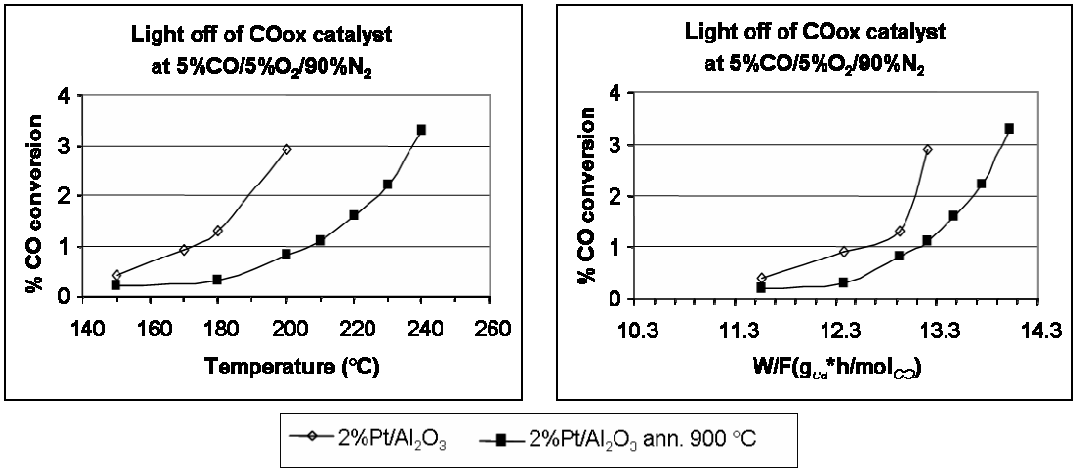

Figure 2: Pt/γ-Al_2O_3 catalyst Light-off as a function of temperature (left) and W/F (right)

The catalyst was placed in a 5 ml reactor and exposed to a gas flow of 100 cc/minute containing 5% CO, 5% O_2, and 90% N_2. The temperature of the reactor was gradually increased till the CO oxidation became noticeable (light-off condition). The reaction was immediately stopped and catalyst sample was collected. The CO conversion as a function of temperature is shown in figure 2. CO oxidation initiates between 140-170 ºC and is about 3% at 200°C.

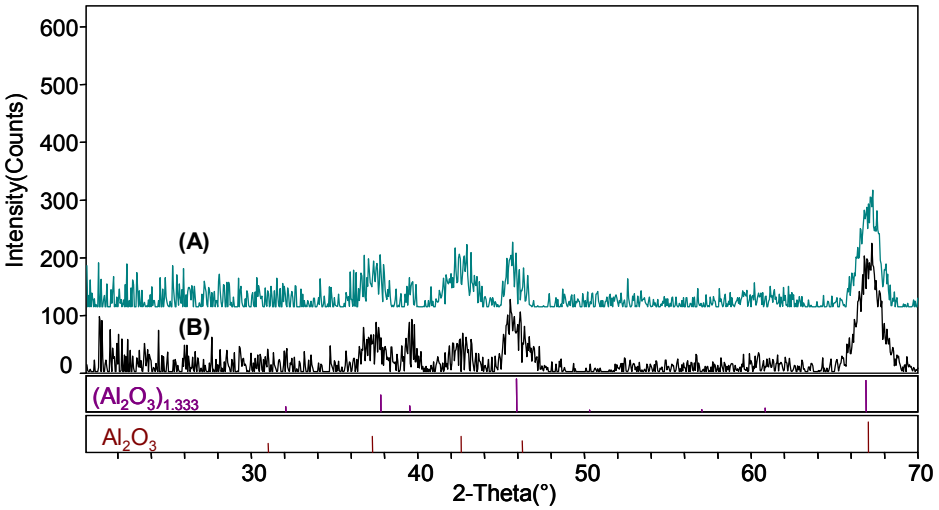

Figure 3: XRD of 2% Pt/γ-Al_2O_3 catalyst (A) fresh and (B) tested

The X-ray powder diffractions of fresh and tested samples are identical suggesting that no new crystalline phases form upon exposure to CO at light-off temperatures.

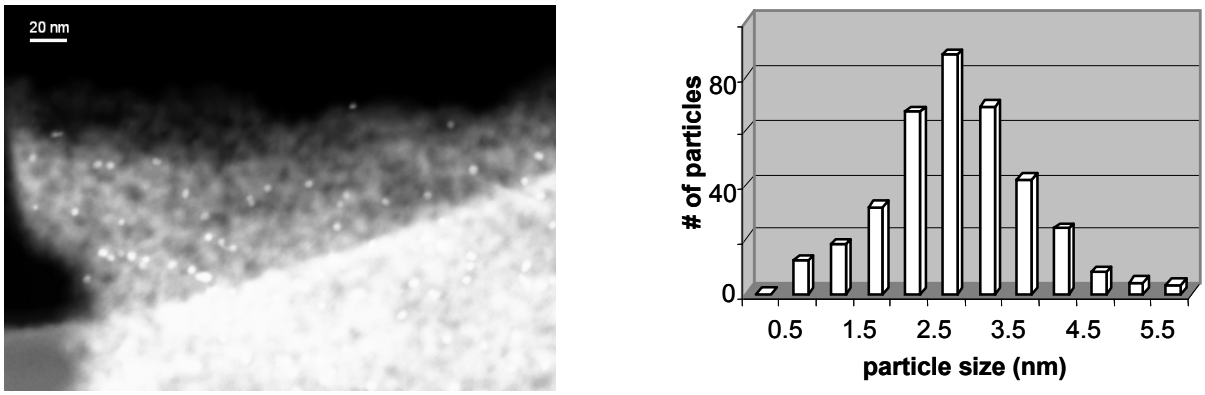

Figure 4: STEM image of 2%Pt/γ-Al_2O_3 catalyst after CO oxidation test (left) and Pt particle size distribution (cf. Figure 1)

The STEM image of catalyst sample collected from the reactor after CO light-off shows that rapid sintering of Pt particle has occurred under such mild conditions. The Pt particle size distribution is in 0.5-5.5 nm range with almost Gaussian distribution and center at about 2.5 nm. In this particle size range, the large particles (above 2nm) should have metallic cores.

The large particle size 2%Pt/γ-Al_2O_3, obtained by annealing the catalyst material at 900 °C in ambient atmosphere led to increase in particle size to 40 nm (calculated from XRD by Scherrer formula). The CO oxidation for this catalyst initiated between 180-200ºC and was 3% at 240ºC [Figure 2].

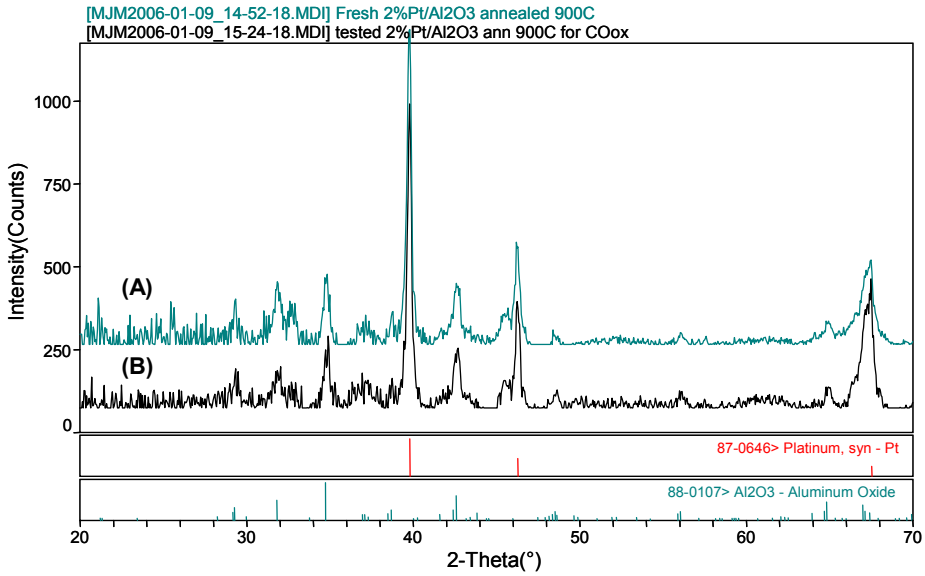

Figure 5: XRD of 2% Pt/γ-Al_2O_3 catalyst annealed at 900ºC (A) fresh and (B) tested

The X-ray powder diffractions of fresh and tested samples are identical suggesting that no new crystalline phases form upon exposure to CO at light-off temperatures.

These results suggest following:

- Small cluster of supported Pt are more reactive towards CO oxidation than large clusters at low temperatures as evident from low light-off temperature of small clusters.
- Small clusters of Pt react with CO and generate species that are labile and hence susceptible to coarsening at relatively low temperatures.

We have begun using Density Functional Theory (DFT) based methods to investigate the adsorption of several atomic and molecular species relevant to CO oxidation, including O, O_2, CO, and CO_2, on several small Pt and Pt oxide clusters. The results obtained so far indicate that the ability of the Pt and Pt oxide clusters to bind these species is strongly dependent on their size as well as their extent of oxidation (summarized in Figure 5).

The adsorption energies of O, O_2, and CO_2 on pure Pt_x clusters display similar and complex patterns, having a maximum at Pt_2 followed immediately by a minimum at Pt_4. The adsorption energies then percolate toward the level on the bulk Pt surface. The CO_2 adsorption energy is much weaker than that of O or O_2, both on the clusters and on the bulk surface. The adsorption energy of CO, on the other hand, rises monotonically with cluster size, so cluster size may serve as a predictor of CO adsorption strength on Pt clusters.

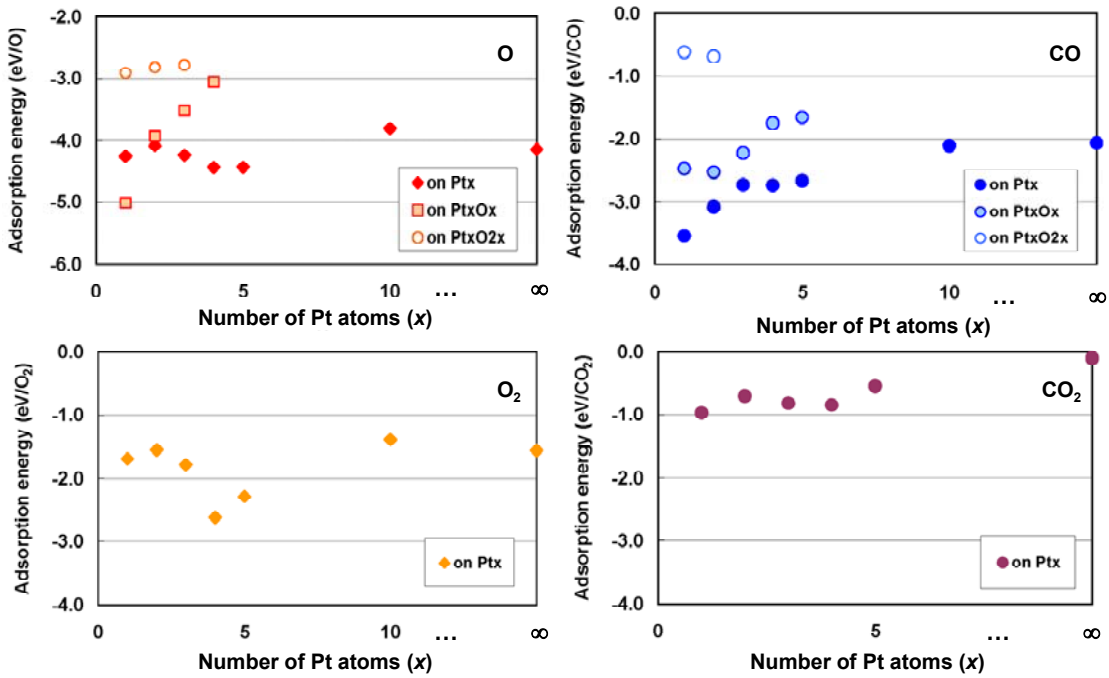

Figure 6: The adsorption energies of O, O_2, CO, and CO_2 on pure Pt (Pt_x) and Pt oxide (Pt_xO_x and Pt_xO_{2x}) clusters, plotted against the number of Pt atoms in the clusters, *x*.

The effect of oxidation on adsorption has been investigated for O and CO. Clearly, the more heavily oxidized the cluster is, the weaker the adsorption of O and CO becomes: The adsorption energies on Pt_xO_x are weaker than those on the pure Pt_x but stronger than those on Pt_xO_{2x}. Interestingly, the adsorption energies of O and CO on the oxidized clusters also show strong size dependence. We speculate that oxidation of small Pt clusters may weaken the adsorption of other atoms and molecules on them as well.

These results are interesting since the experimental results show that 10-20 atom Pt clusters rapidly increase in size in the presence of CO at relatively low temperatures. We are carrying out experiments to understand this result.

Rhenium-Alumina System:

Since Pt-carbonyl cluster chemistry on alumina is not well-developed, we chose Re-carbonyl clusters supported on alumina as surrogates for Pt-alumina clusters of less than 10 atoms. In previous report, we described the synthesis of rhenium-alumina systems by two methods, namely, decarbonylation of $H_3Re_3(CO)_{12}/\gamma\text{-}Al_2O_3$ and decomposition of $ReCl_5$ impregnated $\gamma\text{-}Al_2O_3$. STEM images of $H_3Re_3(CO)_{12}/\gamma\text{-}Al_2O_3$ treated in H_2 at 400 °C to decarbonylate the clusters were also obtained using the ACEM. Images at high magnification indicated uniform clusters with diameters of ca. 0.4 – 0.8 nm. The instability of the microscope caused sample drift hindering efforts to captures images of atomic resolution. Rhenium has a 1.37 Å radius, which suggests that the clusters are composed of 1-3 Re atoms.

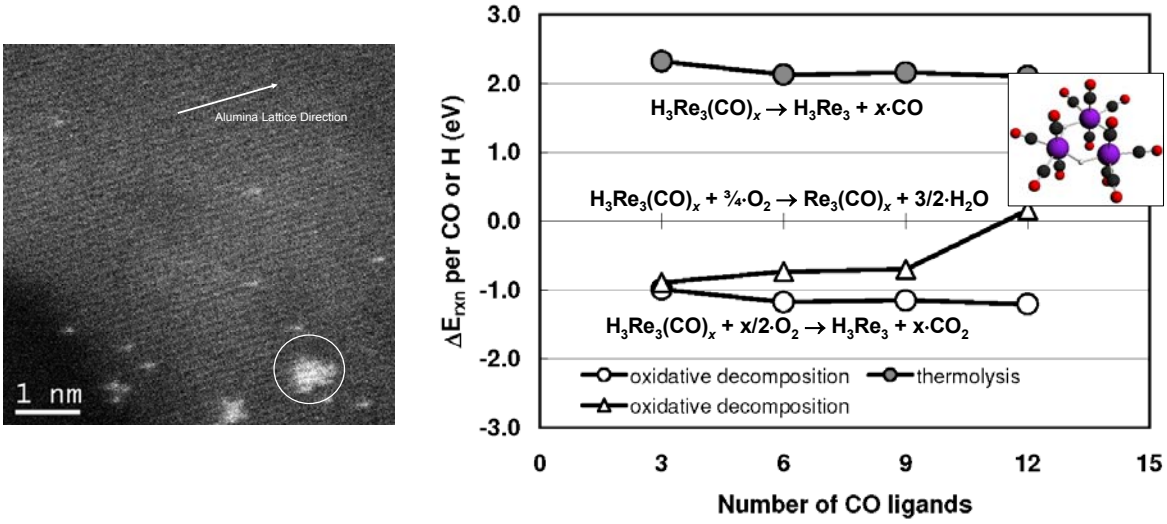

Figure 7: ACEM. Images at high magnification (left) and the reaction heats of the thermal and oxidative decomposition of the $H_3Re_3(CO)_{12}$ organometallic precursor in gas phase (right).

To begin to understand the properties of the Re clusters obtained by the decarbonylation of the $H_3Re_3(CO)_{12}$ precursor, we have performed DFT analysis of the decomposition chemistry of the precursor. Figure 7 shows the three reactions from top to bottom, thermal decarbonylation, oxidative dehydrogenation, and oxidative decarbonylation. Negative heats denote exothermicity. The inset shows the structure of the precursor (purple atoms=Re; black atoms=C; red atoms=O; white atoms=H). Preliminary results suggest that thermally breaking the ligands off the precursor is energetically less favorable if oxygen is available to burn them off instead. In addition, it appears to be easier to break off the carbonyl groups (CO) than the hydrides (H). This suggests that the Re clusters obtained from the decarbonylation of the $H_3Re_3(CO)_{12}$ precursor may in fact be Re hydride clusters.

Re/γ-Al_2O_3 synthesized by $ReCl_5$ impregnation on commercial γ-Al_2O_3 and subsequent calcining led to small (1-1.5 nm) clusters. Microstructural characterization on the ACEM shows two types of areas. In one type of areas, 10-20 atom clusters of essentially 1 nm were observed that were reminiscent of our Pt/γ-Al_2O_3 materials. While these clusters are not completely random in the atomic arrangement, 3D metallic order is not observed. The second area shows smaller less uniform clusters and single atom structures.

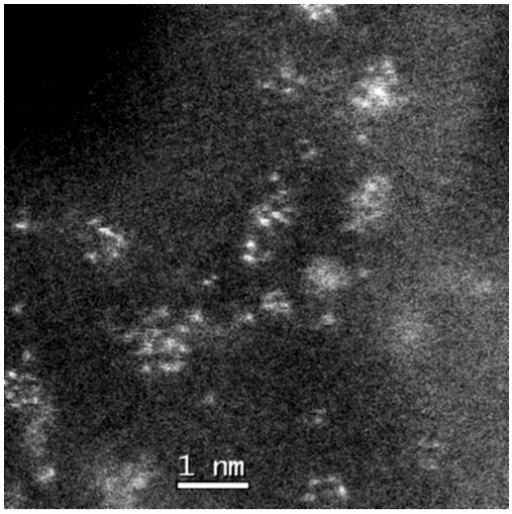

Figure 8: ACEM Images of 2% Re/γ-Al_2O_3 synthesized by $ReCl_5$ impregnation

The CO oxidation on 1-3 atom Re supported on γ–alumina initiated between 230-240ºC and was 3% at 260ºC [Figure 9]. Part of the increase in light-off temperature is due to higher space velocity.

In contrast, the CO oxidation on 10-20 atom Re supported on γ–alumina initiated between 180-200ºC and was 3% at 240ºC [Figure 9]. As compared 10-20 atom Pt/ γ–alumina clusters, the high light-off temperature is probably due to differences in reactivity.

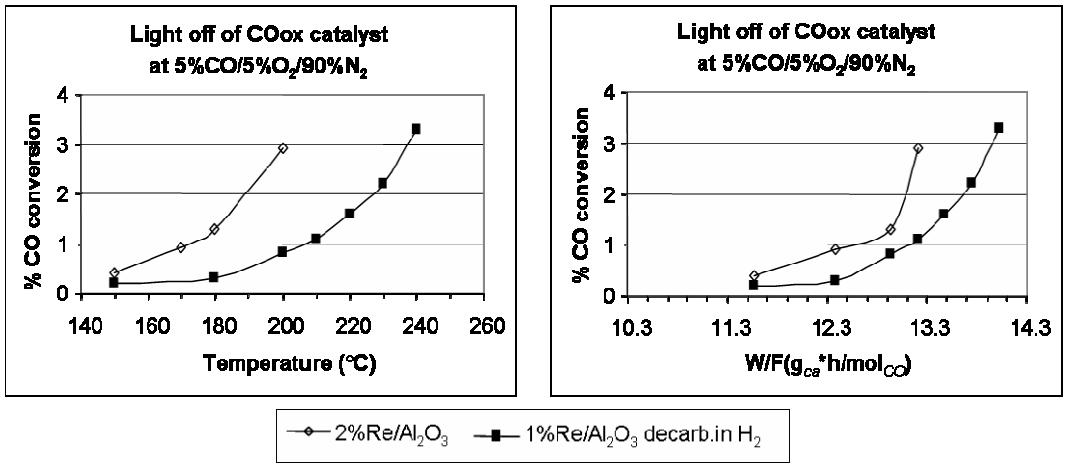

Figure 9: Pt/γ-Al_2O_3 catalyst Light-off as a function of temperature (left) and W/F (right)

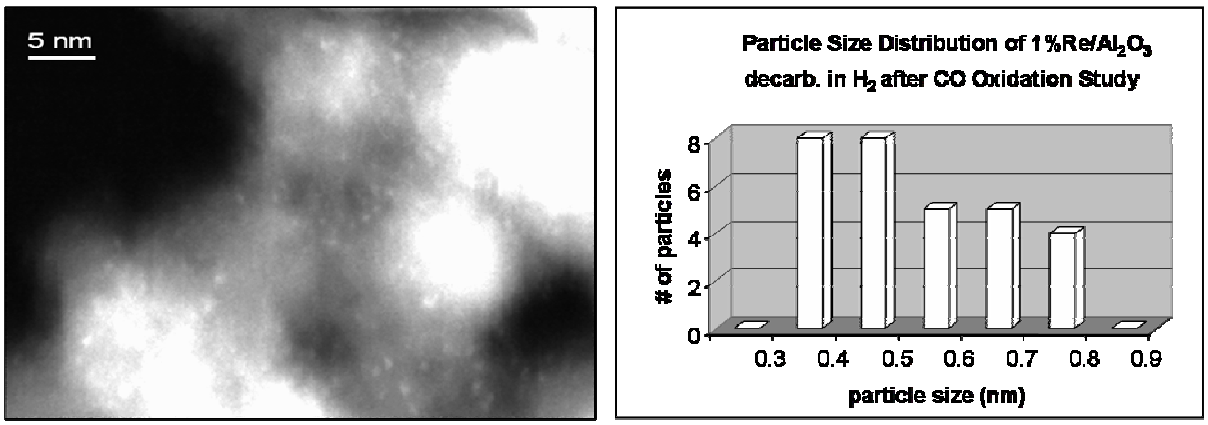

Figure 10: STEM image of 1%Re/γ-Al_2O_3 (by decarbonylation in H_2) catalyst after CO oxidation test (left) and Pt particle size distribution (cf. Figure 1)

The STEM image of the 1%Re/γ-Al_2O_3 (by decarbonylation method in H_2) catalyst sample collected from the reactor after CO light-off shows that no rapid sintering of the Re particle has occurred under these conditions. The Re particle size distribution is in 0.3-0.8 nm range and centered at about 0.5 nm. In this particle size range, the clusters are still likely made up of 1-3 Re atoms. This result is different from the one observed for Pt/γ-Al_2O_3 where particles sintered at low temperature in the presence of CO. As reported previously, these clusters are oxidized although the exact structure of oxide is unknown (cationic or neutral). It is likely that oxidized Re clusters supported on alumina are quite active in catalyzing CO oxidation reaction under the test conditions. We will carry out CO oxidation experiments on reduced Re clusters.

While a STEM image of the 2% Re/γ-Al_2O_3 catalyst after the CO light-off study was difficult to capture, it was clear that rapid sintering of the 10-20 atom clusters did not occur.

The lack of Re particle sintering suggests that different mechanisms are involved for CO oxidation over Pt and Re cluster catalysts. Our planned experiments will help us determine the nature of species involved in CO oxidation.

Next Steps:
We plan to carry out the following tasks:

- We plan to complete CO oxidation studies of already synthesized Pt and Re clusters on alumina to determine the metal species involved in CO oxidation. The results will be compared with the results from theoretical calculation. If consistent, we will proceed with the evaluation of the catalysts for NO_x and hydrocarbon oxidation.

- We will synthesize Pt clusters on sol-gel and molecular sieve alumina and. This will create a matrix of samples with varying Pt particles size and oxidation on alumina substrate with increasing surface area and pore structure. Following tables summarize the already prepared and characterized samples (i.e. commercial, sol-gel, and molecular sieve support materials, the catalysts prepared are shown by √√). We will carry out CO, NOx and HC oxidation on these samples to study the effect of morphological changes in substrates leading to changes in metal substrate interactions.

	Commercial γ-Al_2O_3	**Sol-Gel γ-Al_2O_3**	**Molecular Sieve γ-Al_2O_3**
$[Pt_6(CO)_{12}]^{2-}$	√	√	√
Decarbonylated Pt	√	√	√
Pt_n	√√	√	√
Pt_x	√√	√	√
$H_3Re_3(CO)_{12}$	√√	√	√
Decarbonylated Re	√√	√	√
Re_n	√√	√	√
Re_x	√√	√	√

- As the next step in our computational efforts, we will study the thermochemistry of CO and NO oxidation on Pt and Pt oxide clusters in order to demonstrate if and how reaction energetics vary as a function of cluster size and the extent of oxidation. We will also begin to investigate the properties of Pt clusters on oxides and to extend our thermodynamic model to include support effects.

  At the same time, we will begin to study Pt and Pt oxide clusters on Alumina supports. These investigations will help us gain a better understanding of the structural and catalytic properties of the supported Pt clusters and by comparing these results to our earlier work on Pt and Pt clusters we will be able to gain an understanding of the effect of the support on these important properties.

Communication/Visitors/Travel

Y. Xu presented a paper at AIChE annual meeting in Cincinnati

Publications/Presentations

1. Y. Xu, W. A. Shelton, W. F. Schneider, Theoretical Aspects of Oxide Particle Stability and Chemical Reactivity, in *Synthesis and Application of Oxide Nanoparticles and Nanostructures*; Wiley, in press.

2. Y. Xu, W. A. Shelton, and W. F. Schneider, "The thermodynamic equilibrium compositions, structures, and reactivities of support-confined Pt_xO_y (x=1-3) clusters predicted from first principles," submitted to *Journal of the American Chemical Society*.

3. Y. Xu (speaker), W. A. Shelton, and W. F. Schneider, The oxidation of platinum clusters: Size dependence, thermodynamics, and effect on reactivity, AIChE Annual Meeting, Cincinnati, OH 10/2005.

Durability of Diesel Engine Particulate Filters

Edgar Lara-Curzio, Amit Shyam, H-T. Lin and Randy Parten
Oak Ridge National Laboratory

Objectives/Scope

To develop/implement test methods to characterize the physical and mechanical properties of ceramic Diesel particulate filters (DPFs), and to implement a probabilistic-based analysis to quantify their durability and reliability.

Highlights

The temperature dependence of the fracture toughness of porous cordierite was determined between 20°C and 900°C.

Technical Progress

During the reporting period work continued to assess the effect of temperature and environment on the fracture toughness of porous cordierite and its resistance to crack growth. The fracture toughness was determined by the double-torsion test method. It was found that the fracture toughness decreases with temperature from 0.45±0.02 MPa√m at 20°C to 0.35±0.01 MPa√m at 500°C and that it increases with temperature from 500°C to a value of 0.45±0.00 MPa√m at 900°C. The thermal expansion behavior and the increase in the Young's modulus of this material with temperature are in part responsible for the temperature dependence of the fracture toughness. The elastic modulus and thermal expansion of porous cordierite exhibit a hysteretic behavior upon heating and cooling which is caused by closing and opening of microcracks. As the material is heated, microcracks that formed during cooling from the processing temperature begin to close and continue to close up to 1000°C. The closure of microcracks results in an increase in the elastic modulus of the material. The contribution of other deformation mechanisms on the temperature dependence of the fracture toughness of porous cordierite is under investigation.

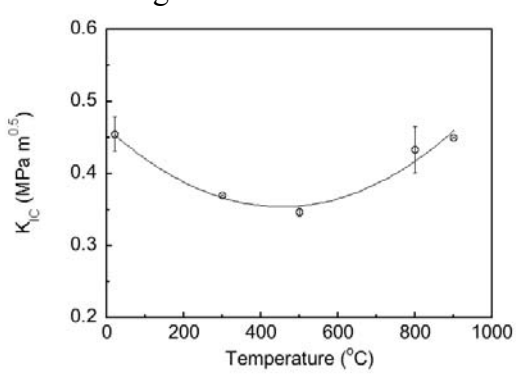

Figure 1. Effect of temperature on the fracture toughness of porous cordierite.

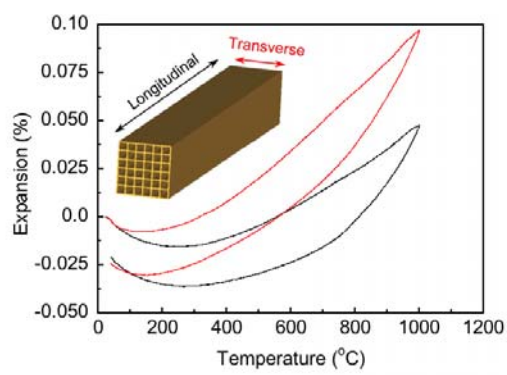

Figure 2. Thermal expansion of porous cordierite as a function of temperature.

Milestones

Report the effect of water vapor on the rate of slow-crack growth, static and dynamic fatigue of cellular cordierite filters at elevated temperatures (March 2006). (On track)

Meetings

Monthly teleconferences with Cummins and Corning personnel were held during the reporting period.

NO_x Reduction Technology by Urea SCR

Nidia C. Gallego and Cristian I. Contescu
Oak Ridge National Laboratory

Objective

The goal of this program was to evaluate the potential of carbon monoliths as supports for low temperature NO_x-reduction catalysts by urea-SCR in after-treatment units of diesel vehicles. The biggest challenge of urea-SCR mobile applications is to improve the low-temperature performance of catalysts. Research on ammonia-SCR catalysts for stationary diesel-fueled power plants has shown that replacing TiO_2, the traditional support of vanadia catalysts, with activated carbon afforded a significant decrease in the reaction temperature; carbon-supported catalysts were also more tolerant to sulfur poisoning in the low temperature range (150-250ºC). This is due to better dispersion of the active phase on the large surface area of carbons and weaker interaction of the support with the active vanadium oxide phase. However, the potential of using carbon as a catalyst support for urea-SCR units in mobile diesel applications has not been evaluated.

The work on the project started in October 2005. In the first two months, an extensive search of recent literature reports was performed, for down-selection of suitable catalyst compositions, including the nature of active phase and support charateristics. The literature search revealed that metal oxide catalysts (Fe_2O_3, Cr_2O_3, V_2O_5, CuO, NiO) supported on activated carbons with large surface area exhibit high dispersion of the oxide phase, and therefore high catalytic activity. Urea (or ammonia) selective catalytic reduction (SCR) is possible beginning from temperatures in the range of about 150 – 200°C. It was planned that similar catalysts would be prepared and tested in this project, using as a support a high surface area carbon fiber monolith support, developed previously in ORNL. In order to correctly develop the impregnation procedure of the catalytically active phase on the carbon support, the pH response of the un-modified support needs to be characterized. Preliminary work was started on using the acid-base titration method developed in 2005 at ORNL for characterization of pK distribution of functional groups on carbon supports. Also, the chemicals required for preparation of these catalysts were ordered during the month of December.

In addition, the work was initiated for modification and adaptation of an existing gas flow test unit to the requirements of catalytic tests. Two options were identified, namely either adding specific IR gas detectors (including ammonia) to an existing NOx removal system, or upgrading an existing test rig and mass spectrometer unit, currently used for gas breakthrough measurements, to meet the needs of catalytic tests. The second option was preferred because it offered more flexibility. During the month of December 2005, a series of accurately prepared gas mixtures with known compositions was ordered in view of calibration of the gas concentration measurements on the catalyst testing lines. Also, the sampling system and the vacuum lines of the mass spectrometer unit were serviced for minor repairs and maintainance.

The project was discontinued in early January 2006 due to budget reallocation.

Austenitic Stainless Steel Alloys for Exhaust Manifold

P. J. Maziasz, John P. Shingledecker, and N. D. Evans
Oak Ridge National Laboratory
M. J Pollard
Caterpillar, Inc.

Objective/Scope

This is the 2nd ORNL CRADA project with Caterpillar, which is focused on commercialization of the new CF8C-Plus cast austenitic stainless steel, which was developed during the first ORNL/CAT CRADA. CF8C-Plus stainless steel is a cost-effective material upgrade for much more performance, durability and temperature capability relative to current heavy-duty diesel engine exhaust components made from SiMo ductile cast iron. In FY 2005, this project completed the initial properties data base needed for alternate materials selection, and component design or redesign, including fatigue, thermal fatigue, and creep, and studies of aged materials. Longer term creep-testing and fatigue studies at much lower frequencies are underway, together with new tests directly related to specific component applications, like turbocharger housings. This CRADA (Cooperative Research and Development Agreement) project (ORNL02-0658) was extended beyond the initial 3-year term last year, and will be completed in July 2007. Requests for more detailed information on this project should be made directly to Caterpillar, Inc.

Highlights

Caterpillar, Inc.

Stainless steel diesel turbocharger housings have been made by Caterpillar's supplier, and are now being evaluated and tested.

The large CF8C-Plus cast gas-turbine housing has been sectioned and found free of defects and hot-tears, and mechanical testing is underway.

ORNL

Initial tensile and creep testing on new commercial heats of CF8C-Plus Cu/W show a significant advantage at 750°C and above.

CF8C-Plus steel shows a significant advantage in creep resistance at 750°C compared to the Diado KN2 cast austenitic stainless steel; both are being evaluated as upgrade alternatives to SiMo cast iron for diesel engine turbocharger housings. ORNL testing continues this quarter.

Technical Progress, 1st Quarter, FY2006

Background

Current cast iron heavy diesel engine exhaust manifolds and turbocharger housings are being pushed beyond their temperature capabilities as normal duty cycles approach or exceed 750°C; the rapid and severe thermal cycling contributes to increased failures. The new cast CF8C-Plus austenitic stainless steel is now being commercialized and evaluated for this and many other high-temperature applications. Caterpillar, Inc. and ORNL are completing the systematic and

thorough properties data base required by designers to optimize component design, and are characterizing the properties of trial or prototype commercially cast stainless steel components.

Approach

Multiple commercial heats of CF8C-Plus have been cast by several commercial foundries, including static sand and centrifugal casting methods. Now, both large and small prototype CF8C-Plus components are being cast. In July, 2004, a large turbine housing for an industrial gas-turbine was cast by MetalTek, International, Inc. from an 8000 lb heat of the new CF8C-Plus stainless steel. In 2005, three foundries obtained trial-licenses for CF8C-Plus steel, including MetalTek and Stainless Foundry and Engineering. By the end of 2005, over 31,000 lb of CF8C-Plus components have been cast, including exhaust manifolds and thin-walled piping. In 2005, new commercial heats of CF8C-Plus Cu/W were made, and found to have more tensile strength and more creep resistance than CF8C-Plus at 750°C and above. The outstanding castability and freedom from post-cast heat-treatments are distinct advantages for CF8C-Plus and CF8C-Plus Cu/W steels.

Technical Progress – Caterpillar, Inc.

The large industrial gas-turbine housing cast of CF8C-Plus stainless steel by MetalTek (6,700 lb), has been sectioned and inspected. No hot tearing at the side flange was found. This observation is significant because fully austenitic alloys like CF8C-Plus are often suspected of being more susceptible to hot tearing than similar steels with a much higher -ferrite content (standard CF8C steel has 15-25%). CF8C-Plus steel has better fluidity and castability than standard CF8C steel. NDT analysis also showed no evidence of hot tears.

Mechanical properties specimens have been from this cast turbine housing, and the initial mechanical testing began this quarter.

Some stainless steel diesel-engine turbocharger housings have been made for a small quantity off-road diesel engine application. Due to current supplier agreements, these parts were cast from commercially available KN2 stainless steel. This prototyping effort was done to give designers at Caterpillar confidence with cast stainless steel as well as some experience with the necessary design changes for cast stainless. Direct creep-rupture tests to compare CF8C-Plus and KN2 stainless steels are in-progress at ORNL.

Technical Progress - ORNL

In 2005, a new commercial heat of modified CF8C-Plus steel, with further additions of Cu and W, was made for ORNL by MetalTek. The initial tensile testing of as-cast material found that the Cu and W additions significantly boosted the YS relative to CF8C and CF8C-Plus at 600-850°C, particularly above 750°C. Tensile testing and preliminary fatigue testing (very high cycling frequency) of as-cast material are complete. Aging continued at ORNL this quarter on these steels, and creep, and slower cycle-rate fatigue and creep-fatigue studies began this quarter. Data from creep-rupture testing at 750°C is shown below, with the Cu and W additions have a large effect on reducing the minimum creep rate and prolonging the secondary creep regime relative to CF8C-Plus steel.

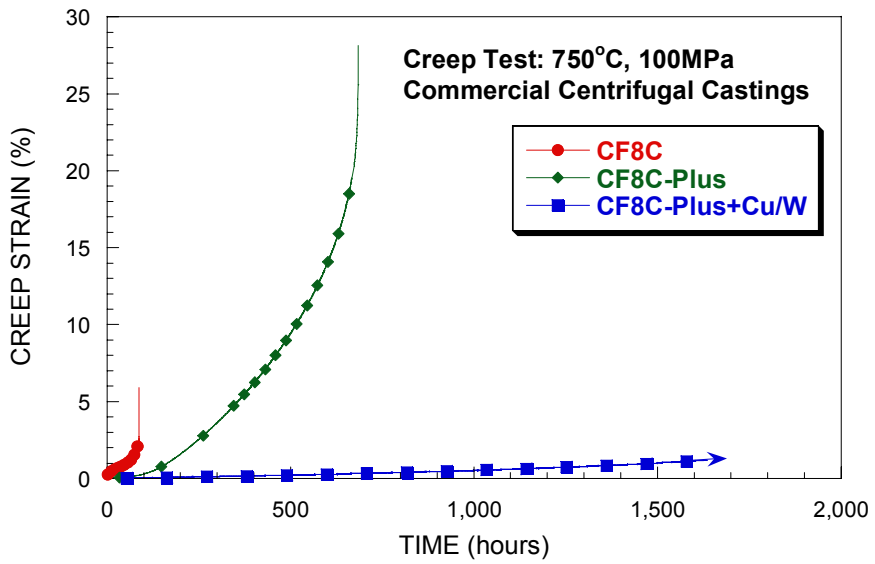

Figure 1 – Plots of creep-strain versus time for heats of standard CF8C, CF8C-Plus and the new CF8C-Plus Cu/W, all tested in at 750°C at ORNL. Clearly the CF8C-Plus Cu/W has much more creep resistance, with an extended secondary creep-regime and a very low secondary creep rate.

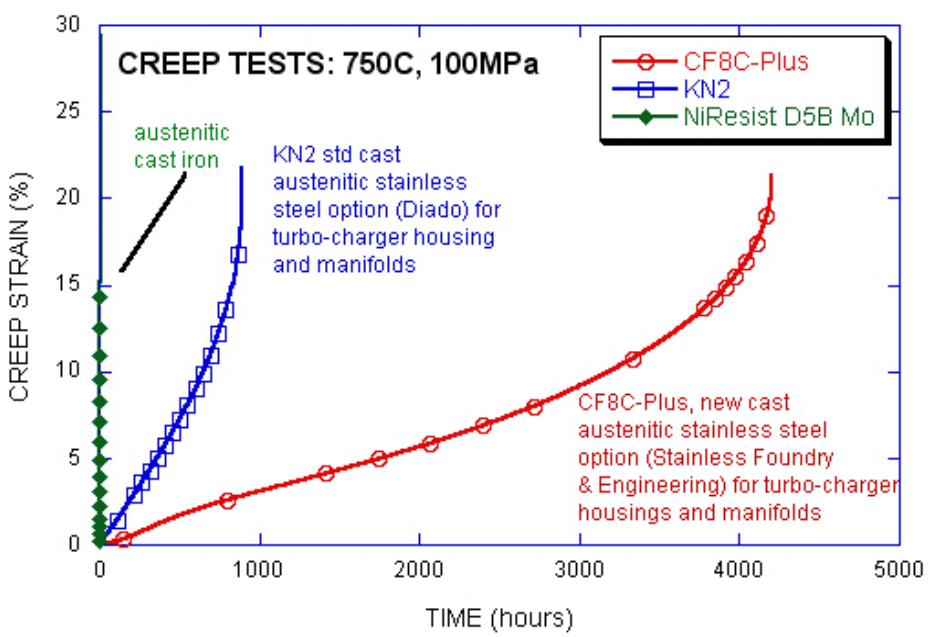

Figure 2 – Comparison of Ni-resist austenitic cast iron, a potential upgrade relative to SiMo cast iron for diesel or natural gas reciprocating engine exhaust components, and two cast austenitic stainless steels being considered as upgrade materials for turbocharger housings, KN2 (Diado in Japan) and CF8C-Plus (Stainless Foundry & Engineering in Waukesha, WI). ORNL creep-rupture testing at 750°C and 100 MPa in air.

In 2005, ORNL began testing and characterization of the Diado KN2 cast austenitic stainless steel (Fe-19Cr-12Ni-0.7Nb-0.3C, Si,S steel) and comparision to CF8C-Plus steel, in support of efforts to upgrade turbocharger housings from SiMo cast iron to cast stainless steel by Caterpillar's component supplier. Last quarter, both cast stainless steel were shown to good room temperature tensile properties, both in the as-cast and in the aged (1000h/750°C) condition. This quarter, preliminary creep-rupture testing at 750oC, shows that the CF8C-Plus has about 4 times longer rupture life than the KN2 steel, and that both stainless steels have much more rupture resistance than Ni-resist austenitic cast iron. Testing will continue next quarter.

Communications/Visits/Travel

Detailed team communications between ORNL and Caterpillar occur regularly. The new 3 year CRADA began on July 21, 2002, when the previous CRADA ended and is scheduled to end on July 21, 2005. The two-year ORNL/Caterpillar CRADA extension was done last year until July 21, 2007.

Status of Milestones (ORNL for DOE)

FY2006 (1) Complete properties measurements of new CF8C-Plus Cu/W heats, including static and centrifugally cast materials, at 700-850°C (02/06). On-track for completion. (2) Expand commercialization opportunities and complete licensing of CF8C-Plus to commercial foundries and other end-users (08/06). On track, but reductions in FY2006 funding seriously curtail this effort.

Publications/Presentations/Awards

Awards:

The Review Panel for FY2005 DOE Heavy Vehicles Materials Program Merit Review and Peer Evaluation Meeting, held September 13-15, 2005 at ORNL (Oak Ridge, TN) awarded this CRADA project the highest overall score (3.4 out of a maximum of 4.0) in the Heavy Vehicles Propulsion Materials sub-program element. This project also received the highest individual evaluation category grades for Relevance (3.5), Technical Accomplishments (3.75), and Technology Transfer (3.25).

Publications:

J.P. Shingledecker, P.J. Maziasz, N.D. Evans, and M.J. Pollard, "Alloy Additions for Improved Creep-Rupture Properties of a Cast Austenitic Alloy," pp. 129-138 of Creep Deformation and Fracture, Design, and Life Extension, eds. R.S. Mishra, J.C. Earthman, S.V. Raj, and R.Viswanathan, Materials Science & Technology 2005 (2005).

Presentations:

P.J. Maziasz, J.P. Shingledecker, N.D. Evans and M.J. Pollard, "Alloying Additions for Improved Creep-Rupture Properties of a Cast Austenitic Stainless Steel," presented at the Symposium on Creep Deformation and Fracture, Design, and Life Extension, at Materials Science & Technology 2005, held Sept. 25-28, 2005 in Pittsburgh, PA.

Friction and Wear Reduction in Diesel Engine Valve Trains

Peter Blau and Jun Qu
Oak Ridge National Laboratory

John Truhan
University of Tennessee, Knoxville, TN

Objective/Scope

The objective of this effort is to enable the selection and use of improved materials, surface treatments, and lubricating strategies for value train components in energy-efficient diesel engines. Depending on engine design and operating conditions, between 5 and 20% of the friction losses in an internal combustion engine are attributable to rubbing between valve train components. Wear and consequent leaks around valve seats can reduce cylinder pressure and engine efficiency. Contacting surfaces in the valve train include the valve heads, seats, tappets, guides, and stems. This effort is designed to address key rubbing interfaces within the valve train where there are opportunities to employ advanced materials and surface treatments to reduce friction and save energy.

A two-pronged, interdisciplinary approach is planned to address both materials and lubrication-related aspects. The first task involves the design and construction of a laboratory testing apparatus to simulate the kinds of thermal, chemical, and mechanical contact environments that are characteristic of valves and valve seats. The second task involves improving the performance of the valve stem as it oscillates within its guide. This task takes into consideration not only the valve stem and guide materials, but also the thin film of lubricant that must ensure low-friction as the valves actuate and yet should not creep down the valve guide and into the seat area.

Technical Highlights

This project is new for FY 2006, so this first quarterly report provides a summary of the background and rationale for the tasks in the research plan.

Task 1. *Design and Use of a High-Temperature, Controlled Environment, Valve Material Testing System*. Following a study of the literature, and after consulting engine designers, a testing system to apply the mechanical forces and motions experienced by valves under high-temperatures and gaseous operating environments will be designed and built. Material performance criteria will be developed based on detailed examination of the nature of repetitive impact contact damage in thermochemically active environments, and current valve materials will be used to benchmark performance. In FY 2007, promising new materials, including composites and surface-engineered materials, will be investigated. Relationships will be established between composition, microstructure, and modes of contact damage. Recommendations will be made for the selection of materials and surface treatments that offer the best performance in next-generation, energy-efficient engines.

Task 2. *Materials and Lubrication Optimization for High-Performance Valve Guides*. The model for boundary lubrication developed under a prior DOE-sponsored project will be modified

to account for valve stem and guide contact conditions. This process will begin with a series of macro-scale friction experiments on conformal surfaces separated by thin lubricating films. Results will be extended to model the more complex, reciprocating conditions experienced with valves. Both current and future stem and guide materials will be used to test the validity of the model as a design tool for establishing the limits of lubrication and the specification of surface finishes for best low-friction, reliable performance.

Progress. In preparation for Task 1, a literature study of the modes of surface damage for valves and valve seats in common valve materials has been initiated. Several possible contact geometries for the high-temperature, repetitive impact tester are being explored, as are the means to control the gas flow, temperature and environmental monitoring and containment.

In preparation for Task 2, a sled-type, flat plate friction testing apparatus has been designed and is in the final stages of construction. It is intended to enable the study of the macroscopic behavior of boundary lubricating films under controlled conditions and better understand the valve stem/guide interface.

Future Plans

1) Continue the study of valve degradation modes as a function of material type.
2) Continue design work on the elevated temperature, repetitive-impact testing system.
3) Complete the fabrication of the boundary lubrication testing apparatus.

Travel

None this period.

Status of Milestones

1) Complete low-speed friction experiments that will serve as the basis for modeling the boundary-lubrication characteristics of valve stems and guides. **(03/06)***
2) Construct a valve seat simulator and establish baseline material performance data under high-temperature, engine-like conditions. **(09/06)***

* An unexpected reduction in the FY 2006 funding for this project is likely to delay completion of these milestones. Dates will be updated within the coming quarter.

Publications and Presentations

None.

Advanced Machining and Sensor Concepts

Albert Shih
University of Michigan

Objective/Scope

The objective of this research is to investigate new technologies for cost-effective machining of Ti alloys. Experiments of high-throughput drilling of Ti-6Al-4V at 156 mm^3/s material removal rate using 4 mm diameter WC-Co spiral point drill has been achieved with good drill life. The turning test of Ti using new TiC-based tool material is continued.

Technical Highlights

Experiments of high throughput drilling of Ti-6Al-4V were continued. The thrust force, torque, tool wear mechanism, hole surface roughness, and chip morphology for high material removal rate (MRR) drilling have been investigated. Supplying the cutting fluid via through-the-drill holes has proven to be a critical factor for drill life. Feed is identified as another important process parameter. The balance of cutting speed and feed is essential to achieve long drill life and good hole surface roughness. The performance of professionally prepared TiC (91%)-Ni_3Al (9%) metal matrix ceramic (MMC) tool insert for turning CP Ti was tested with limited tool life.

1. High throughput drilling

To achieve the desired MRR, high cutting speed and feed per revolution of drill are required [1]. The drilling of Ti-6Al-4V at high cutting speed has been reported in 2005 Annual Report. The effect of feed in drilling and the drill life are studied extensively. This research investigates the balance of cutting speed and feed in high throughput drilling to achieve long drill life and good hole surface roughness.

1.1. Experimental setup and design

High throughput drilling test was conducted at High Temperature Materials Lab at ORNL using a Cincinnati Saber machine with 4 mm diameter Kennametal K285A01563 WC-Co spiral point drill (WC-Co Spiral). The workpiece was a 6.35 mm thick Ti-6Al-4V plate. This machine has the high speed spindle and through-the-spindle high pressure coolant system. The cutting fluid was 5% CIMTECH 500, a synthetic metalworking fluid. The cutting fluid was supplied internally through the drill body because externally supplied cutting fluid did not help drilling at high speed. The feed was gradually increased from 0.051 to 0.076, 0.102, and 0.152 mm/rev at corresponding drill rotational speed to maintain the same 0.75 m/min feed rate and 156 mm^3/s MRR.

A Hitachi S-4700 scanning electron microscope (SEM) was used to examine the tool wear. Energy dispersive spectroscopy (EDS) method was applied to further study the tool wear mechanism. The holes were cut in half to measure the roughness of hole surface using the Taylor Hobson Talysurf model 120 stylus surface profilometer with 0.8 mm cutoff length and 100:1 bandwidth ratio. For each drilling test, the first three holes were measured. For each hole, three roughness readings were taken, approximately 45° apart circumferentially.

1.2. Drill life, thrust force, torque, and hole surface roughness

Supplying the cutting fluid via through-the-drill holes is essential to drill life in high throughput drilling. At 183 m/min cutting speed and 0.051 mm/rev feed, the internal cutting fluid supply significantly increased the drilling life to 101 holes from 10 holes in dry drilling.

Adjusting the feed also has a significant impact on drill life. Feed is a process parameter which has been overlooked by drilling researchers in the past. Advanced spiral point drill geometry design and new tool material enable the drill to take a higher cutting force and the use of larger feed, which corresponds to lower cutting speed. As shown in Fig. 1, at 0.076 mm/rev feed, the thrust force was at about 200 N and the drill life was 153 holes. Increasing the feed to 0.102 mm/rev only raised the thrust force to about 260 N for the new drill and 330 N at the end of drill life (204 holes). Advanced drill geometry design can withstand such increase in cutting forces. The lower cutting speed at higher feed helps to reduce the drill temperature, which is beneficial to the drill life.

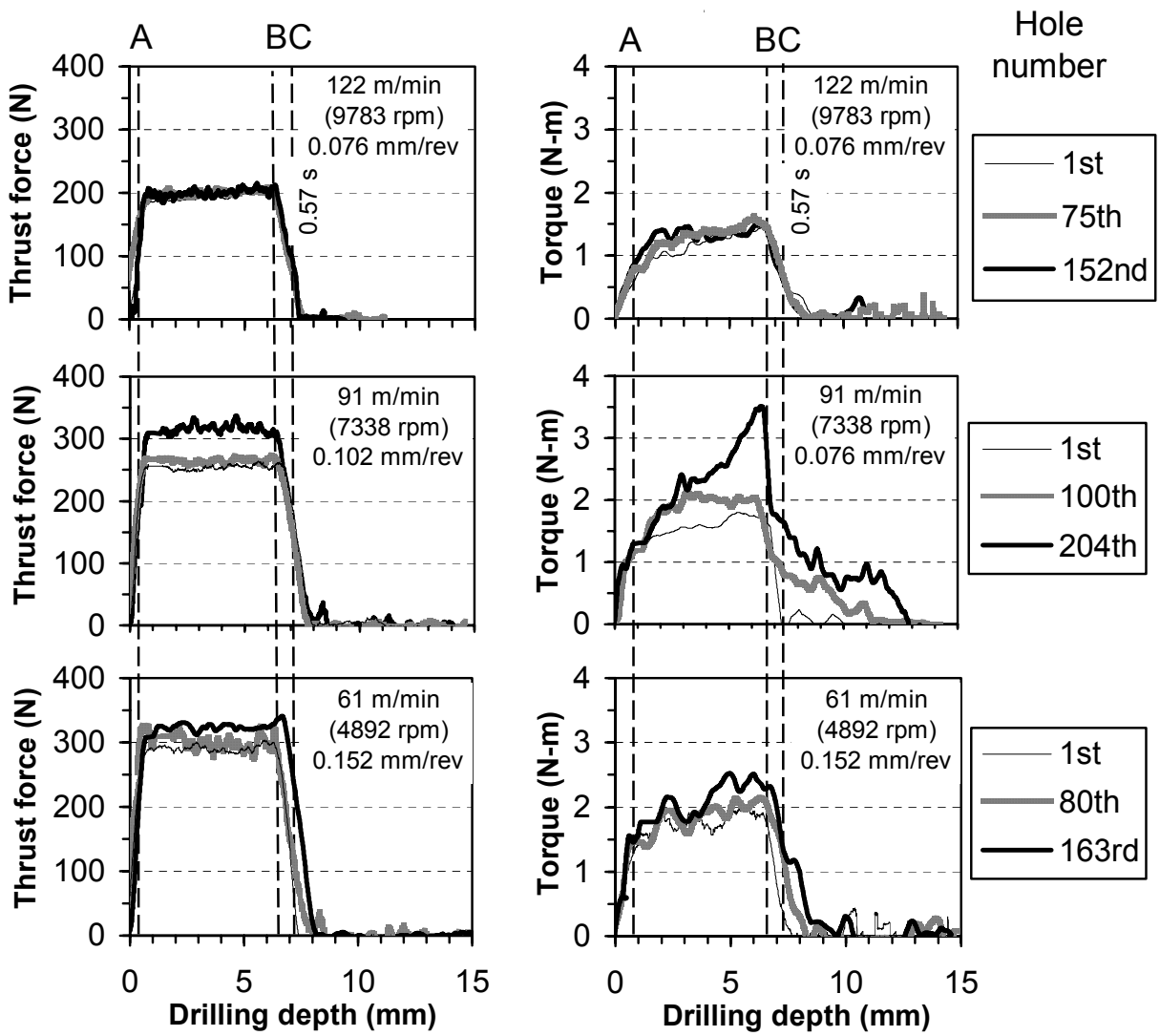

Fig. 1. Thrust force and torque of WC-Co Spiral drill for high throughput drilling at 0.75 m/min feed rate and 156 mm^3/s material removal rate with internal cutting fluid supply.

This study also found that there was a limit of drill life associated with the increase of feed. As the feed increased to 0.152 mm/rev, the drill life (164 holes) started to deteriorate due to the high cutting force.

The drill which had good drill life also produced holes with lower surface roughness. Fig. 2 shows the hole surface roughness vs. drill life (number of holes) for high throughput drilling tests. All tests have the same MRR, 156 mm^3/s. The range of upper and lower surface roughness of the first three holes is presented. In Exp. IV, the internal cutting fluid supply helps to improve the surface finish. The long drill life positively correlates to the good initial hole surface finish.

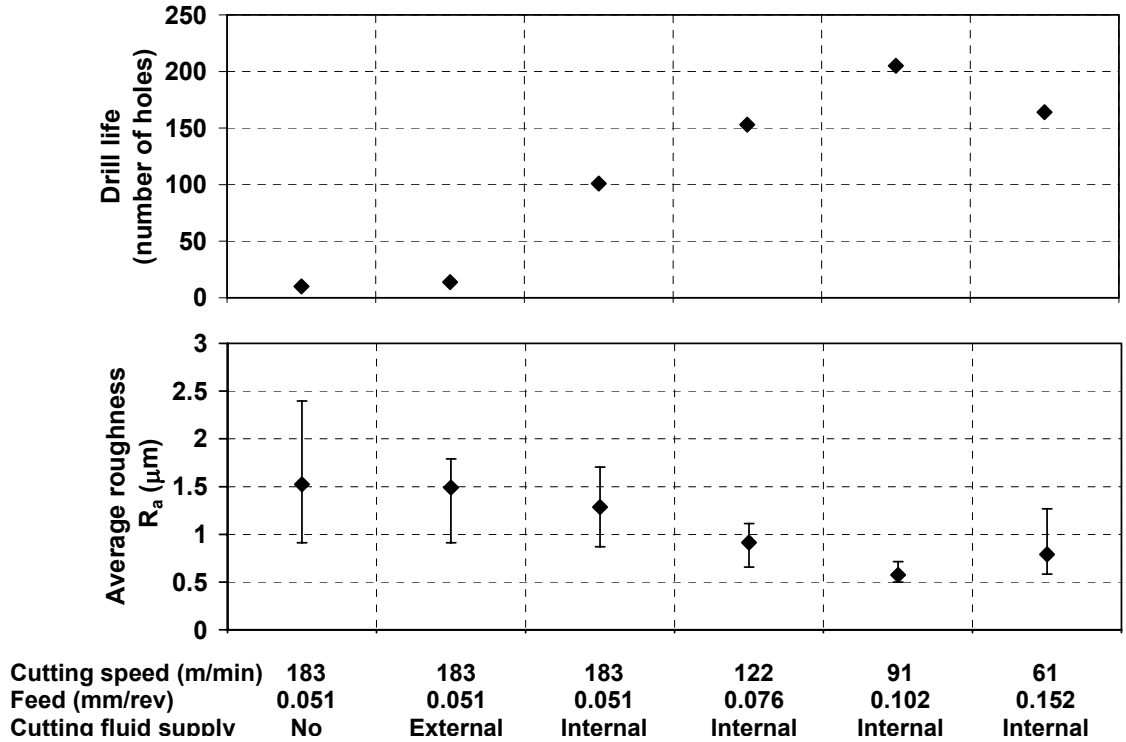

Fig. 2. Hole surface roughness under high throughput drilling with the same material removal rate (156 mm^3/s) using WC-Co Spiral drill.

1.3. Chip light emission and morphology

As shown in Fig. 3(a), chip light emission or sparks could be observed in some Ti drilling tests. Due to the low thermal conductivity of Ti, the chip temperature is high and subsequently creates the oxidation or burning [2-4]. With WC-Co Spiral drill, drilling at 183 m/min cutting speed and 0.051 mm/rev feed, chips sparked in almost every hole drilled in dry drilling and drilling with external cutting fluid supply. When the cutting fluid was supplied internally through the drill at the same cutting speed and feed, no chip light emission could be observed initially. In the 80th hole (out of 101 holes drilled), when the drill wear reached a threshold level of specific energy input, the chip light emission started to occur. For three drilling conditions at 122, 91, and 61 m/min cutting speed, the chip light emission occurred in the 120th, 125th, and 140th hole, respectively. This shows that drilling at the highest and lowest feed under the same MRR, the drill failed quickly after the start of chip light emission. This light emission is usually associated with the chip welding, which could be identified by the difficulty to remove the chip in the flute near the drill tip.

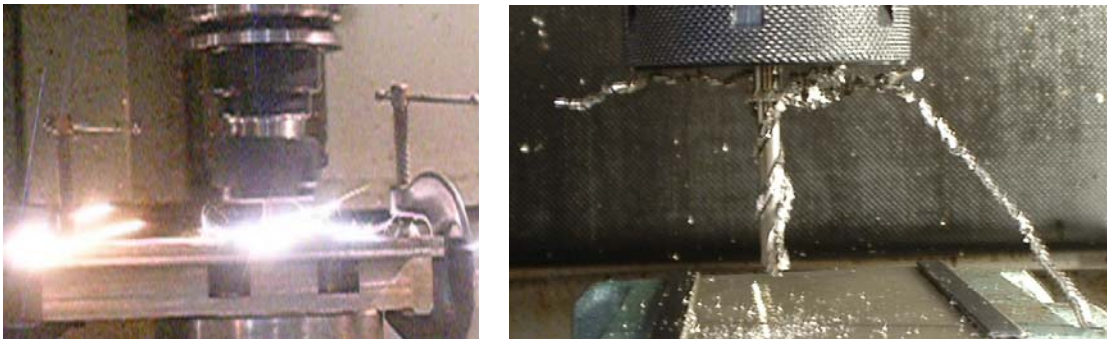

(a) (b)

Fig. 3. Drilling of Ti-6Al-4V: (a) sparks during drilling and (b) drill body entangled by chips.

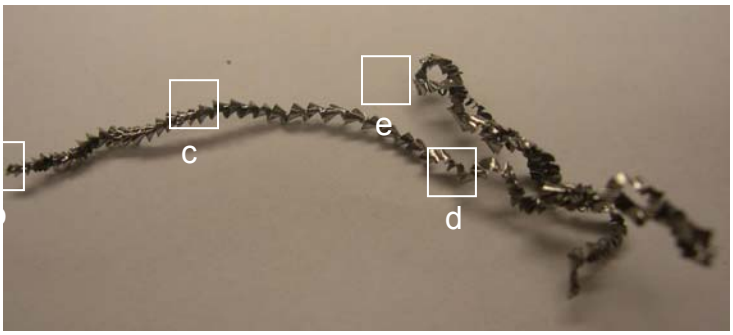

(a)

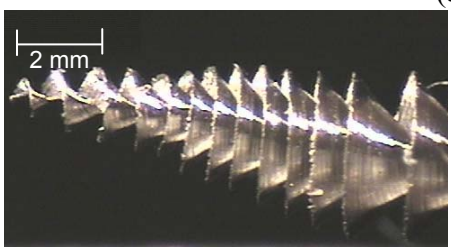

(b)

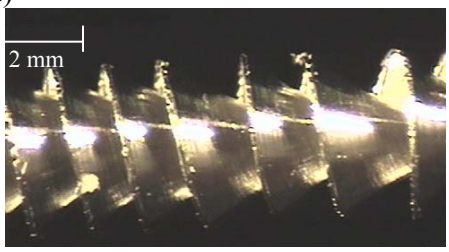

(c)

(d)

(e)

Fig. 4. Chip morphology of Ti-6Al-4V generated by WC-Co Spiral drill: (a) whole chip, (b) initial spiral cone (c) steady-state spiral cone, (d) transition between spiral cone and folded long ribbon, and (e) steady-state folded long ribbon.

After drilling, the Ti chip could be entangled around two flutes of the drill and bend by the tool holder, as shown in Fig. 3(b). This is called chip entanglement, which is due to the difficulty for smooth chip ejection. With internal cutting fluid supply, chip entanglement occurred after the 95th, 130th, 150th, and 150th hole at 183, 122, 91, and 61 m/min cutting speed, respectively.

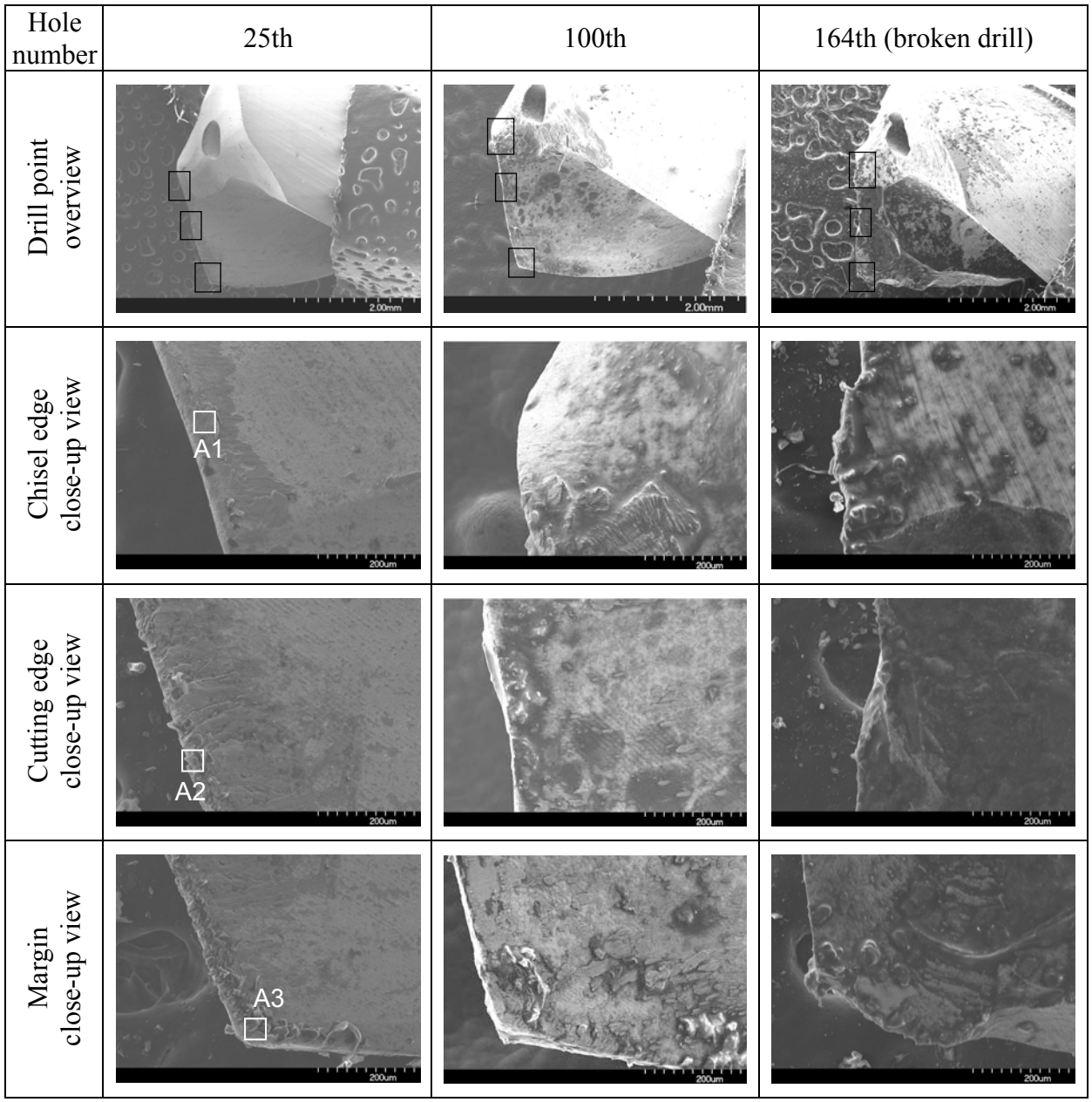

Fig. 5. SEM micrographs of tool wear of the WC-Co Spiral drill at 61 m/min cutting speed and 0.152 mm/rev feed with internal cutting fluid supply.

The same chip morphology, a continuous chip with three regions of initial spiral cone followed by the steady-state spiral cone and folded long ribbon chip, can be seen in all Ti drilling tests in this study. An example of the chip generated by WC-Co Spiral drill is shown in Fig. 4(a). The close-up view of the initial spiral cone, generated at the start of drilling from the beginning of contact to the full engagement of cutting edge, is illustrated in Fig. 4(b). After the cutting edge engaged the workpiece, the steady-state spiral cone chip morphology, as shown in Fig. 4(c), was generated. Due to the increased resistance to eject the chip, the spiral cone was changed to folded ribbon chip morphology. Close-up view of the chip transition region and the folded ribbon chip are shown in Figs. 4(d) and (e), respectively.

1.4. Tool Wear

SEM micrographs of the progressive wear of a WC-Co Spiral drill for high throughput drilling at 61 m/min cutting speed and 0.152 mm/rev feed with internal cutting fluid are presented in Fig. 5. The drill was removed from the machine and examined after drilling 25, 100, and 164 holes. The drill broke in the drill body in drilling the 164th hole while leaving the drill tip in the workpiece. It enabled the observation of the drill wear at the end of drill life.

Four SEM micrographs, the overview of drill point and the close-up views of the chisel edge, middle of cutting edge, and intersection of the margin and cutting edge, as shown by boxes in the overview of the drill tip, are presented after drilling 25, 100, and 164 holes. After drilling 25 holes, minimal drill wear could be recognized. The chisel edge was sharp with slight work-material buildup, as marked by A1. The middle of cutting had slight material buildup, as marked by A2. Relatively more significant, but not severe, material buildup was observed at the intersection of cutting edge near the margin due to the relatively high cutting speed in this area. The EDS x-ray of areas A1, A2, and A3 showed identical outcome in elemental analysis, as illustrated in a representative result in Fig. 6. It had Ti, Al, and V, the composition of the Ti-6Al-4V alloy, which indicated the adhesion of work-material on the drill. It also had W and C, the composition of the tool material, and O, representing the oxidation at high drilling temperatures.

After drilling 100 holes, as shown in Fig. 5, the tool wear was obvious. On the chisel edge, residual Ti work-material buildup on the surface became more apparent. Similar material buildup was observed in the middle and outside corner of the cutting edge. The corner of the drill margin and cutting edge remained sharp, indicating the drill was still capable of effective drilling.

The drill tip at the time of drill breakage at 164 holes was not melted but had fractured significantly. Close-up views showed that the chisel edge and middle cutting edge were both fractured. The corner of drill margin and cutting edge was also severely fractured and no longer sharp. The drill had lost the shape for effective drilling. The cutting forces were expected to be high and a broken drill was expected.

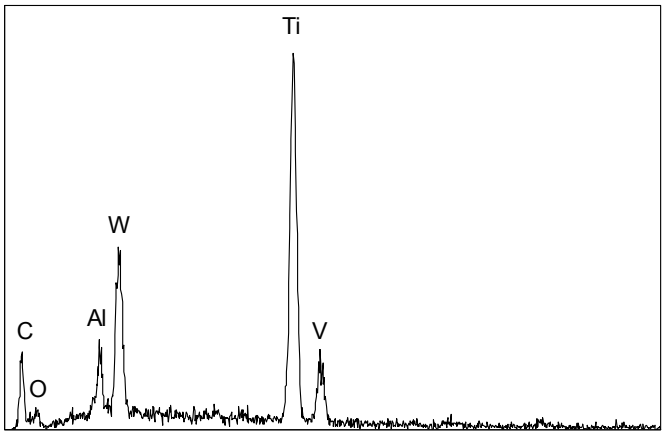

Fig. 6. EDS analysis of regions with chip buildup: A1, A2, andA3.

2. Turning test with professionally prepared TiC-Ni_3Al (9%) material

This research is the continuation of investigation of TiC-Ni_3Al for Ti machining tool material. TiC-Ni_3Al (9%) has a low porosity than that of TiC-Ni_3Al (5%). It could increase the tool life at low cutting speed. However, the tool life was still short at high cutting speed, 195 m/min, compared with WC-Co tool. Since high cutting forces were observed for the manually prepared TiC-Ni_3Al tool test in previous study, the tool insert with its surface and cutting edge professionally prepared by Kennametal is tested in this research.

2.1. Turning test results

The cutting forces at 195 m/min cutting speed, 0.25 mm/rev feed, and 1.02 mm depth of cut are summarized and compared with a WC-Co tool in Fig. 7. Consistently, the TiC-Ni_3Al tools showed high cutting forces. With the same chemical composition, the better preparation of tool insert slightly lowered the cutting forces of the TiC+Ni_3Al (9%) tool, but still generated higher cutting forces than the WC-Co tool.

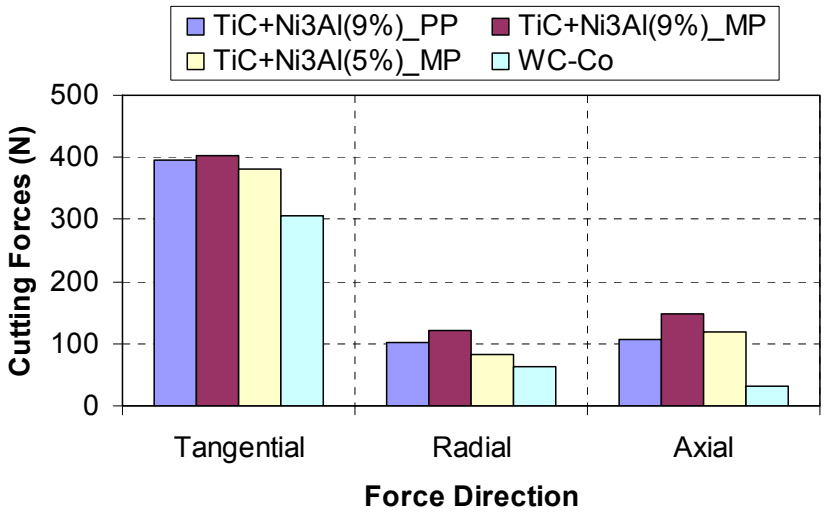

Fig. 7. Cutting forces of TiC-Ni_3Al and WC-Co tools in machining of Ti at 195 m/min cutting speed, 0.25 mm/rev feed, and 1.02 mm depth of cut (PP: tool ground by Kennametal, MP: tool manually prepared).

Table 1 summarizes the tool life of the TiC-Ni_3Al tools compared with a WC-Co tool at 195 m/min cutting speed. It is clear that even with professionally prepared tool edge and surface, the tool life of TiC-Ni_3Al (12.3/21.5 s) was still not comparable to that of WC-Co (69 s). The catastrophic breakage at the tool corner, as shown in Fig. 8, was the failure mode for all TiC-Ni3Al tools. The brittleness of the material needs to be overcome before its application as a successful cutting tool material.

Table 1. Tool life in machining Ti at 195 m/min cutting speed, 0.25 mm/rev feed, and 1.02 mm depth of cut

Tool material	TiC-Ni_3Al (9%)_PP	TiC-Ni_3Al (9%)_MP	TiC-Ni_3Al (5%)_MP	WC-Co
Tool life (s)	12.3/21.5	9.2/33.7	15.3	69

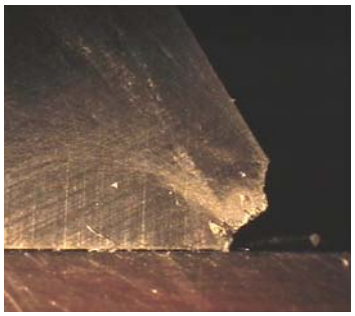

Fig. 8. Broken TiC-Ni_3Al (9%) with Kennametal ground insert geometry, after cutting 21.5 s at 195 m/min cutting speed, 0.25 mm/rev feed, and 1.02 mm depth of cut.

Future Work

The research will continue in the thermal-mechanical coupled finite element modeling of Ti drilling with the collaboration of Third Wave Systems. The temperature measurement using the inverse heat transfer method will be attempted for high throughput drilling conditions. As the next step, the research will be expanded to the field of high-throughput milling of Ti.

Status of Milestones

Milestone 1: Experimental study of Ti drilling.

Status: Extensive tests of Ti drilling have been conducted and reported. The 183 m/min cutting speed and 156 mm^3/s material removal rate have been achieved in drilling Ti-6Al-4V using 4 mm diameter WC-Co spiral point drill. The high throughput drilling of Ti alloy is proved technically feasible.

Milestone 2: 3D finite element modeling of titanium drilling process.

Status: This work is continuing. A new version of Third Wave drilling has been released and is testing at University of Michigan.

Milestone 3: Investigation of TiC-based cutting tool material.

Status: Exploratory tests of two TiC-Ni_3Al cermets with 5% and 9% matrix material have been conducted. The performance of the tool inserts with surface and cutting edge professionally prepared has been tested with some good but not outstanding results. The brittleness of the TiC-Ni_3Al is identified as the main direction to improve for its future application as tool material.

Milestone 4: Measure of Ti drilling temperature.

Status: The inverse heat transfer method was developed to analyze the tool temperature in Ti drilling. High drill temperature was observed in drilling Ti, particularly at high cutting speed.

Communications/Visit/Travel

Rui Li and Paul Becker visit BorgWarner Turbo at Asheville, NC, on Nov. 2, 2005.
Albert Shih visited Oak Ridge National Lab on Dec. 13, 2005.

Publications

R. Li and A. J. Shih, "Finite Element Modeling of 3D Turning of Titanium," *International Journal of Advanced Manufacturing Technology* (in print).

R. Li, A.J. Shih, 2005, "Inverse Heat Transfer Solution of Tool Temperature in Titanium Drilling," *Journal of Manufacturing Science and Engineering* (submitted).
R. Li, P. Hegde, A.J. Shih, 2006, "High Throughput Drilling of Titanium Alloys," *International Journal of Machine Tools and Manufacture* (submitted).

References

[1] D.A. Stephenson, J.S. Agapiou, Metal Cutting Theory and Practice, Marcel Dekker, New York, 2005.
[2] J. Cantero, M. Tardío, J. Canteli, M. Marcos, M. Miguélez, 2005, "Dry Drilling of Alloy Ti-6Al-4V," International Journal of Machine Tools and Manufacture 45, 1246-1255.
[3] M. Bakkal, C.T. Liu, T.R. Watkins, R.O. Scattergood, A.J. Shih, 2004, "Oxidation and Crystallization of Zr-based Bulk Metallic Glass due to Machining," Intermetallics 12, 195-204.
[4] M. Bakkal, A.J. Shih, S.B. McSpadden, C.T. Liu, R.O. Scattergood, 2005, "Light Emission, Chip Morphology, and Burr Formation in Drilling the Bulk Metallic Glass," International Journal of Machine Tools and Manufacture, 45, 741-755.

Synergistic Process-Enhanced Grinding

R. H. Chand
Oak Ridge National Laboratory

Objective/Scope

The objective of this effort is to understand, develop, and apply synergistic process-enhanced grinding (SPEG) to improve the efficiency of grinding advanced materials while ensuring surface quality. The three tasks involved in meeting this objective comprise a systematic approach: evaluate current technology, develop new technology, and acquire an understanding of the fundamental principles that underlie that technology.

Technical Highlights

Description and Rationale for the New Project in Synergistic Process-Enhanced Grinding: This effort began in FY 2006 and this is the first quarterly report. Therefore, it is appropriate to describe the background and rationale before presenting a summary of progress.

New, high-performance truck engines exact greater demands on structural materials – from fuel injectors to valves and exhaust gas recirculation system components. The cost of machining high-performance materials by traditional methods can be a barrier to their widespread use. While advances in the science of machining during the last two decades have created the means to fabricate and finish high-performance materials like ceramics, titanium alloys, and metal matrix composites, considerable challenges still remain to understand machining on a fundamental level and to apply that knowledge to cost-effectively achieve the level of high surface quality required for precision components. Challenges are particularly great for grinding, where multiple sharp points on a rapidly-spinning grinding wheel cut, plow, and impact the material on the surface of the workpiece. The interactions between the workpiece, the abrasive grinding medium, the coolant, and the machine tool are complex, making research and process modeling difficult.

It is the premise of the new project that the productivity of grinding can be enhanced by combining it with thermal, mechanical, chemical, and electrical processes. Such synergistic interactions can be used weaken the surface and enhance chip formation. Examples of novel approaches that combine one or more traditional machining operations with other processing techniques include laser-enhanced machining, electrochemical in-process wheel dressing (ELID), magnetic fluid grinding, and chemo-mechanical planarization (CMP). These and other synergism-enhanced machining processes offer opportunities to attack the challenges of cost-effective, high through-put machining of diesel engine components. It is therefore the goal of this project in Synergistic Process Enhanced Grinding (SPEG) to develop innovative methodology for machining difficult-to-grind materials, like ceramics and composite, and to understand the fundamental materials-related aspects of this new methodology. Three tasks have been identified in this regard:

Task 1: Conduct a comprehensive investigation of the current state of the art in SPEG methods, especially as related to the preparation of advanced materials like ceramics and composites being considered for diesel engine components. Experience gained from leading the DOE, Cost-

Effective Ceramic Machining project in the 1990s will be used to expedite completion of this task. This study will include identification of both U.S. and non-U.S. developments, including where the leading research efforts and applications of technology are being implemented.

Task 2: Modify one or more existing machine tools at ORNL to conduct instrumented, SPEG experiments on ceramics, cermets, and/or metal matrix composites that are candidates for diesel engine components. Correlations between process parameters and the quality of the resulting surfaces, assessed by metrology and microscopy, will be performed. The selection of the SPEG technique to be developed will be based on the information acquired during the accomplishment of Task 1. Modification of the grinding equipment will be initiated during FY 2006 and continue into FY 2007 when initial trials will be conducted on selected materials.

Task 3: Develop and use a high-speed, instrumented scratch testing system to study the microstructural response of advanced materials like ceramics and composites to the high deformation rates they experience during grinding. This activity will be based on ORNL's extensive experience in developing ASTM scratch hardness testing standards and in conducting dynamic hardness tests. The apparatus to be developed will have the capability of applying heat or coolants to the surface while scratching occurs. The response of advanced materials to high strain rate, single or multiple-point scratches should provide a deeper understanding the SPEG process. The completion of the instrument and an initial series of experiments are planned for the end of FY 2006.

Progress:

Task1: A comprehensive assessment of grinding processes has begun. Claus Daniel, an ORNL Wigner Fellow and expert in development of laser surface modification methods, is assisting in gathering information for this initial assessment.

Task 2: While we wait for the progress of task 1, plans are being drawn to start experiments to establish base lines using current commercial practices and to develop methodology based on use of low surface speed to achieve greater (3 to 7 times conventional) material removal rate.

Task 3: Literature search is continually being conducted on scratch testing of ceramic materials by a diamond indenter.

Future Plans

(1) Continue to compile a background survey of methods, both commercial and experimental, used to enhance the efficiency of grinding hard materials. This will include laser-enhanced methods.
(2) Proceed to test low surface speed machining methodology and other methods as they are identified by task 1.
(3) Begin design of a high speed scratch test.

Travel

None this quarter.

FY 2006 Milestones

1) Complete survey of non-traditional machining processes that combine synergistic effects to enhance materials removal. **(06/06)**

2) Complete construction of a high strain-rate scratch testing system to enable basic grinding studies under environmentally-controlled conditions. (**09/06**)

Presentations and Publications

None this quarter (new project).

NDE Development for Ceramic Valves for Diesel Engines

J. G. Sun and J. S. Tretheway*

Argonne National Laboratory
***Caterpillar, Inc.**

Objective/Scope

Emission reduction in diesel engines designated to burn fuels from several sources has lead to the need to assess ceramic valves to reduce corrosion and emission. The objective of this work is to evaluate several nondestructive evaluation (NDE) methods to detect defect/damage in structural ceramic valves for diesel engines. One primary NDE method to be addressed is elastic optical scattering. The end target is to demonstrate that NDE data can be correlated to material damage as well as used to predict material microstructural and mechanical properties. There are two tasks to be carried out: (1) Characterize subsurface defects and machining damage in flexure-bar specimens of NT551 and SN235 silicon nitrides (Si_3N_4) to be used as valve materials. Laser-scattering studies will be conducted at various wavelengths using a He-Ne laser and a tunable-wavelength solid-state laser to optimize detection sensitivity. NDE studies will be coupled with examination of surface/subsurface microstructure and fracture surface to determine defect/damage depth and fracture origin. NDE data will also be correlated with mechanical properties. (2) Assess and evaluate subsurface damage in ceramic valves to be run in bench test and in a single-cylinder-engine test. All valves will be examined at ANL prior to test, during periodic scheduled shut downs, and at the end of the planned test runs.

Technical Highlights

Work during this period (October-December 2005) focused on acquiring and analyzing laser-scattering NDE data for SN235P Si_3N_4 and TiAl intermetallic natural-gas valves that were tested in a cyclic-impact rig for 20 or 25 hours.

1. Laser-Scatter NDE Evaluation of Rig-Tested Si_3N_4 and TiAl Valves

In the previous period (July-September 2005), twenty-five (25) finish-machined SN235P Si_3N_4 and eleven (11) as-processed TiAl intermetallic valves were evaluated/inspected by ANL's automated laser-scatter NDE system. The SN235P valves consisted of 13 intake and 12 exhaust natural-gas valves, and the 11 TiAl valves were natural-gas exhaust valves. Figure 1 is a photograph of the 23 SN235P and 9 TiAl valves after the processing. These valves will be used by Caterpillar in an engine duration test.

During this period we received and analyzed 5 TiAl and 15 SN235P valves that were proof tested in a cyclic-impact rig at Caterpillar for 20 or 25 hours. The detailed information of rig test and NDE scan for these valves is listed in Table 1. As indicated, only valve-head surface was scanned for SN235P Si_3N_4 valves, while both head and stem surfaces were scanned for TiAl valves because of apparent damage on these surfaces for TiAl valves. NDE data were analyzed and compared with photomicrographic surface images for these valves.

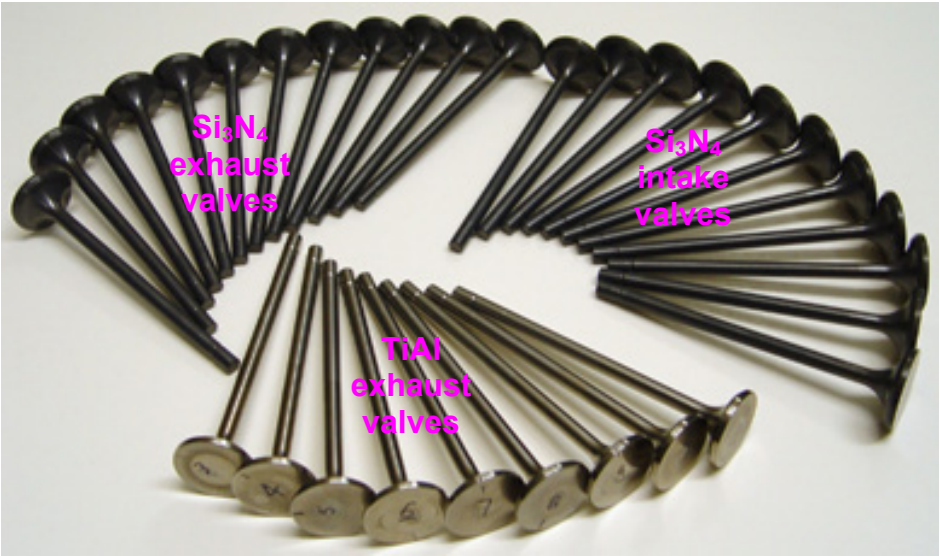

Fig. 1. Photograph of 23 SN235P Si_3N_4 and 9 TiAl intermetallic engine valves.

Table 1. List of rig-test and NDE-scan parameters for TiAl and Si_3N_4 engine valves.

No.	Valve type	Valve #	Rig test duration (h)	NDE scan
1	TiAl exhaust	1	20	head, stem
2	TiAl exhaust	2	20	head, stem
3	TiAl exhaust	3	25	head, stem
4	TiAl exhaust	4	25	head, stem
5	TiAl exhaust	11	20	head, stem
6	Si_3N_4 intake	1	20	head
7	Si_3N_4 intake	8	20	head
8	Si_3N_4 exhaust	9	20	head
9	Si_3N_4 exhaust	11	20	head
10	Si_3N_4 exhaust	17	20	head
11	Si_3N_4 exhaust	19	20	head
12	Si_3N_4 intake	20	20	head
13	Si_3N_4 intake	21	20	head
14	Si_3N_4 intake	25	20	head
15	Si_3N_4 intake	28	20	head
16	Si_3N_4 exhaust	29	20	head
17	Si_3N_4 exhaust	32	20	head
18	Si_3N_4 intake	33	25	head
19	Si_3N_4 exhaust	36	20	head
20	Si_3N_4 intake	41	25	head

For the 15 SN235P Si_3N_4 valves listed in Table 1, laser-scatter scans did not reveal any subsurface damage in the valve head surfaces. This observation is consistent with the results for the 10 NT551 Si_3N_4 valves that exhibited no subsurface damage after testing in the same cyclic-impact rig for up to 1000 hours (see annual report of this project for FY 2004). A few valves, however, showed apparent circumferential "wear scars" within the contact surface. A "wear scar" is seen in the laser-scatter image (Fig. 2) of SN235P exhaust valve #29 after the 20-h rig test. The scarred surface displays lower scatter intensity (darker) in the contact surface. Because defect/damage normally generates higher laser-scatter intensities, the reduction of scatter

intensity within the scarred area indicates that the "wear scar" is not damage, but likely due to surface contamination of embedded metal particles from the metal seat insert. Figure 3 shows a comparison of the laser-scatter image and the photomicrograph of the contact surface. It is evident that there was no apparent surface damage in the scarred area. The higher scatter-intensity spots in the laser-scatter image in Fig. 3 represent material inherent defects such as porosities with sizes typically smaller than 50 microns.

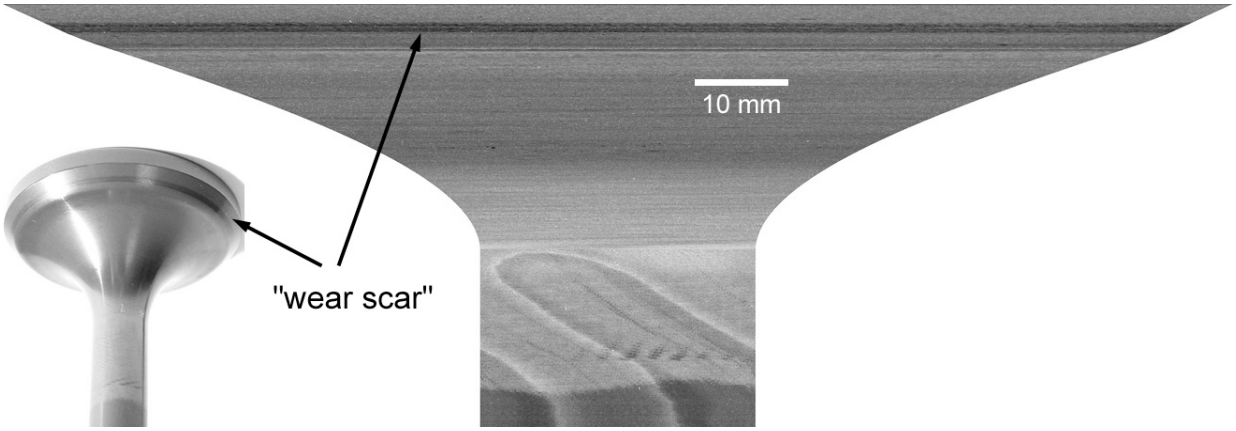

Fig. 2. Laser-scatter scan image of head surface of SN235P valve #29 after 20-h rig test.

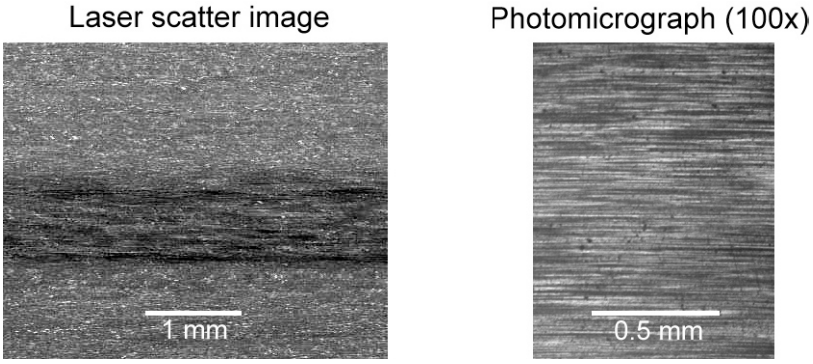

Fig. 3. Detailed laser-scatter image and photomicrograph of contact surface of SN235P valve #29 after 20-h rig test.

For the 5 TiAl intermetallic valves listed in Table 1, significant surface damage from the rig test was observed in the contact and stem surfaces, as seen in Fig. 4 which is a photograph of TiAl valve #1 after the 20-h rig test. The laser-scatter image of the valve-head surface of TiAl valve #1 is shown in Fig. 5. A gross variation of scatter intensity along the axial direction is noticeable, which is due to slight angle or focus-distance mismatch during the scan. The impact wear scar in the contact surface is signified with higher scatter intensities (brighter). Figure 6 shows a comparison of the detailed laser-scattering image and the photomicrograph of the wear scar in the contact surface. It is evident that the laser-scatter intensity is very sensitivity to the surface condition: surface damage, which may result in higher surface roughness, causes strong laser scatter from the surface. The wear damage in the contact areas of TiAl valves #3, #4 and #11 was less severe than that in TiAl valves #1 and #2, as seen in Fig. 7.

Fig. 4. Photograph of TiAl valve #1 after 20-h rig test.

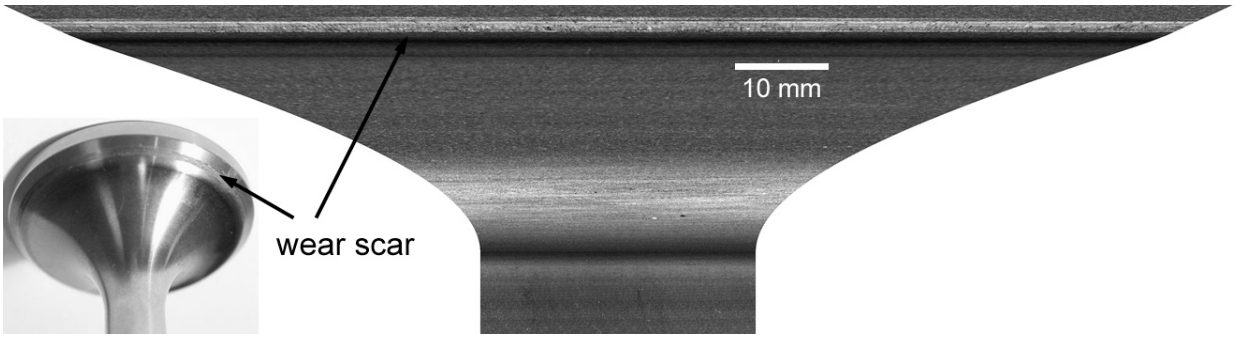

Fig. 5. Laser-scatter scan image of head surface of TiAl valve #1 after 20-h rig test.

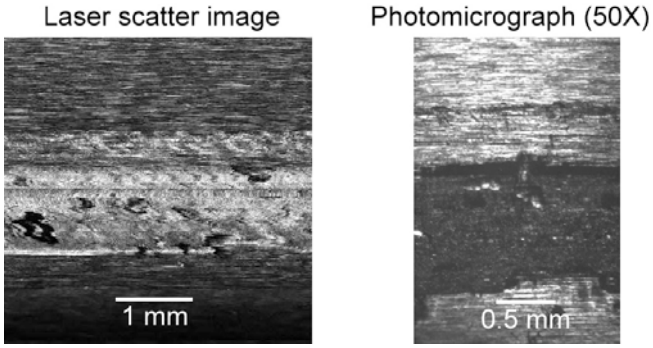

Fig. 6. Detailed laser-scatter image and photomicrograph in contact surface of TiAl valve #1 after 20-h rig test.

(a) 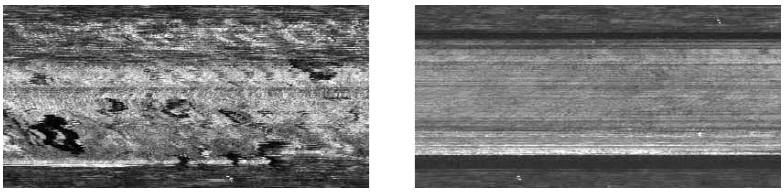 (b)

Fig. 7. Detailed laser-scatter images in contact surfaces of TiAl valves (a) #1 and (b) #3 after, respectively, 20-h and 25-h rig test. Image size is 4 mm x 2 mm.

Laser-scatter scans were also performed for the stem surfaces of all TiAl valves. The wear damage in stem surface is generally aligned in the axial direction as seen in Fig. 4. Figure 8 presents the laser-scatter scan image on the stem surface near the keeper groove of TiAl valve #1. In addition to the axial and circumferential wear stripes of higher scatter intensities, three features that also display higher scattering intensities are identified. These features were

examined under optical microscope. Figure 9 shows the photomicrographs of these features; they are apparently surface damages probably induced by scratch or indent.

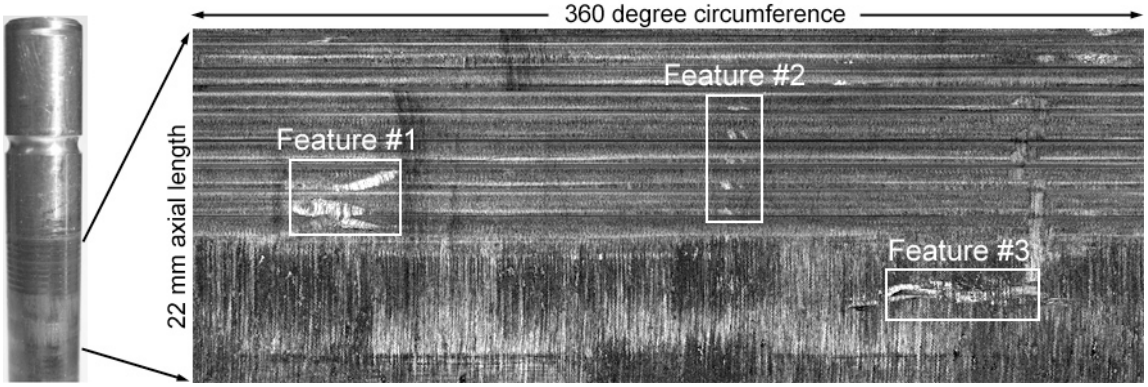

Fig. 8. Laser-scatter scan image of stem surface of TiAl valve #1 after 20-h rig test.

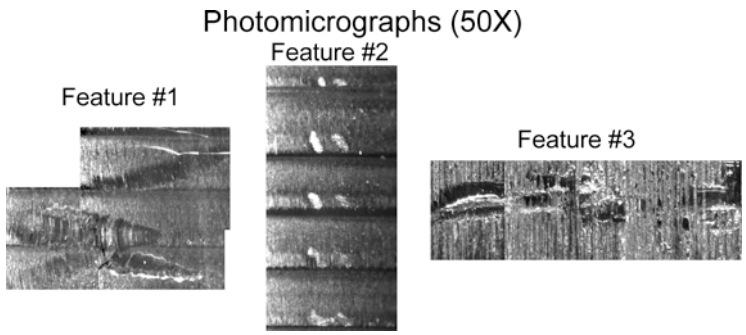

Fig. 9. Photomicrographs of features detected in the NDE data (Fig. 8) for TiAl valve #1 after 20-h rig test.

We have also received 8 TiAl and 4 Si_3N_4 valves that were bench tested for various duration in late Dec. 2005. These valves will be NDE scanned in the next period and results will be presented then. In addition, development of thermographic methods for detecting subsurface damage in intermetallic materials will be presented in the next report.

2. Development of a Confocal Laser-Scatter System for Measurement of 3D Subsurface Microstructure in Silicon Nitride Ceramics

Measurement of detailed 3D subsurface microstructure is critical in determining material properties. However, the laser-scatter method used for subsurface damage detection for ceramic valves can only image the 2D microstructure in the subsurface without the resolution of depth. This is because that the detector receives all subsurface backscatter that originates from all depths. To resolve the depth of the subsurface microstructure (or to selectively detect subsurface backscatter from individual depths), a cross-polarization confocal microscopy technology was developed at Argonne. This technology combines two well-established optical methods, the cross-polarization backscatter (or laser scatter) detection and the scanning confocal microscopy, and can achieve 3D subsurface imaging with sub-micron spatial resolutions, which is one order of magnitude smaller than currently available technologies.

A cross-polarization confocal system has been developed, and its detection sensitivity and resolution were evaluated with objective lenses of 10X, 20X, and 40X magnifications. The spatial resolution of the confocal system is represented by the size of the focus spot, which is determined from diffraction theory. With the 40X objective lens at an optical wavelength of 633 nm, the system resolution was found to be excellent: 2 μm in the axial (depth) direction and 0.6 μm in the lateral direction. Preliminary tests were conducted for NT551 silicon nitride ceramics, results will be presented in the next period.

Status of Milestones

Current ANL milestones are on schedule.

Communications/Visits/Travel

J. G. Sun plans to attend the 30th International Cocoa Beach Conference and Exposition on Advanced Ceramics & Composites, Cocoa Beach, FL, Jan. 22-27, 2006 to present a paper entitled "Nondestructive Evaluation of Machining Damage in Silicon-Nitride Ceramic Valves," and a talk on "Optical NDE Methods for Characterization of Subsurface Microstructure in Silicon Nitride Ceramics."

Problems Encountered

None this period.

Publications

None this period.

Life Prediction of Diesel Engine Components

H. T. Lin, T. P. Kirkland and A. A. Wereszczak
Oak Ridge National Laboratory

Jeremy Trethewey and Nan Yang
Caterpillar, Inc.

Objective/Scope

The valid prediction of mechanical reliability and service life is a prerequisite for the successful implementation of structural ceramics and advanced intermetallic alloys as internal combustion engine components. There are three primary goals of this research project which contribute toward that implementation: the generation of mechanical engineering data from ambient to high temperatures of candidate structural ceramics and intermetallic alloys; the microstructural characterization of failure phenomena in these ceramics and alloys and components fabricated from them; and the application and verification of probabilistic life prediction methods using diesel engine components as test cases. For all three stages, results are provided to both the material suppliers and component end-users.

The systematic study of candidate structural ceramics (primarily silicon nitride) for internal combustion engine components is undertaken as a function of temperature (< 1200°C), environment, time, and machining conditions. Properties such as strength and fatigue will be characterized via flexure and rotary bend testing.

The second goal of the program is to characterize the evolution and role of damage mechanisms, and changes in microstructure linked to the ceramic's mechanical performance, at representative engine component service conditions. These will be examined using several analytical techniques including optical and scanning electron microscopy. Specifically, several microstructural aspects of failure will be characterized:

(1) strength-limiting flaw-type identification;
(2) edge, surface, and volume effects on strength and fatigue size-scaling
(3) changes in failure mechanism as a function of temperature;
(4) the nature of slow crack growth; and
(5) what role residual stresses may have in these processes.

Lastly, numerical probabilistic models (i.e., life prediction codes) will be used in conjunction with the generated strength and fatigue data to predict the failure probability and reliability of complex-shaped components subjected to mechanical loading, such as a silicon nitride diesel engine valve. The predicted results will then be compared to actual component performance measured experimentally or from field service data. As a consequence of these efforts, the data generated in this program will not only provide a critically needed base for component utilization in internal combustion engines, but will also facilitate the maturation of candidate ceramic materials and a design algorithm for ceramic components subjected to mechanical loading in general.

Technical Highlights

Silicon nitride exhaust valves
Studies of optical fractography and SEM analysis on fracture surfaces of selected half-cylindrical valve stems after 500h bench rig test to determine the strength-limiting flaws were completed during this reporting period. Figure 1 and 2 show the representative fracture surface features of two specimens with fracture strength of 900 MPa (Fig. 1) and 1120 MPa (Fig. 2), respectively. Analysis showed that dominant strength-limiting flaws in these tested stems are those internal pores resulting from material processing steps rather than from those transverse surface machining grooves as speculated. The size of the flaws (internal pore) correlates well with the flexural strengths measured. In addition, SEM examinations on valve stem surfaces show that there were remnant features of transverse machining marks, and also the longitudinal markings resulting from the friction between the valve stem and valve guide became apparent, as shown in Fig. 3. Observations also suggest that there is smoothing effect from the repeating friction actions between stem and valve guide, which could possibly reduce the stress concentration values and sites in those transverse-machining flaws.

Preparation of the Caterpillar G3406 nature gas engine that will be used to test both the silicon nitride and TiAl exhaust valves is in progress and also at its final stage of completeness. Initially the engine will be proof-tested with metallic valves currently employed in the engine. After initial successful proof test both silicon nitride and TiAl valves will then be installed and tested under specified engine conditions.

TiAl intermetallic alloy
Studies of long-term creep of TiAl alloys manufactured by Daido and Howmet were initiated during this reporting period. Two types of TiAl specimens (i.e., one is HIP and the other one is Non-HIP) were manufactured by Daido. The test conditions specified are relevant to the temperature and stress profile encountered by TiAl turbo wheel under the application conditions. The database generated will also be used for probabilistic life prediction of turbo wheel under engine operation conditions. Preliminary creep result of Daido HIP TiAl material tested at 650°C at 240 MPa shows that the creep curve transitions into a steady state after a transient state of ~ 200h. The estimated creep rate is ~ 1.84×10^{-9} 1/s after 1000h of creep testing time. Creep test at different temperature and stress level will be initiated to provide insight into the creep mechanisms as function of temperature and stress level.

Status of Milestones
Milestone: "Complete testing and analysis of prototype silicon nitride valves after bench rig testing." Completed.

Communications / Visitors / Travel
Communication with Jeremy Trethewey at Caterpillar on the update of fractography and SEM results of half-cylindrical valve stems after 500 h bench rig test.

Monthly meeting with Jeremy Trethewey Caterpillar and Tim Theiss at NTRC on the updated status of engine preparation for the testing of Si_3N_4 and TiAl exhaust valves.
Communications with Jeremy Trethewey and Nan Yang at Caterpillar on the update of tensile creep tests for TiAl materials.

Problems Encountered
None.

Publications
None

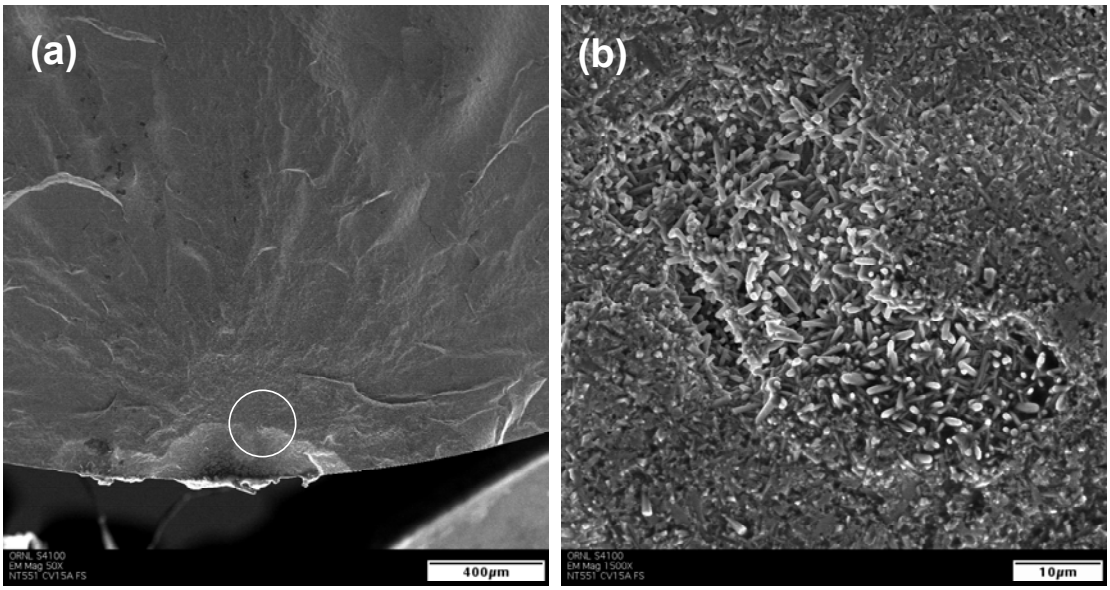

Figure 1. SEM micrographs of fracture surface of NT551 cylindrical valve stem with fracture strength of 900 MPa after 500h bench rig test.

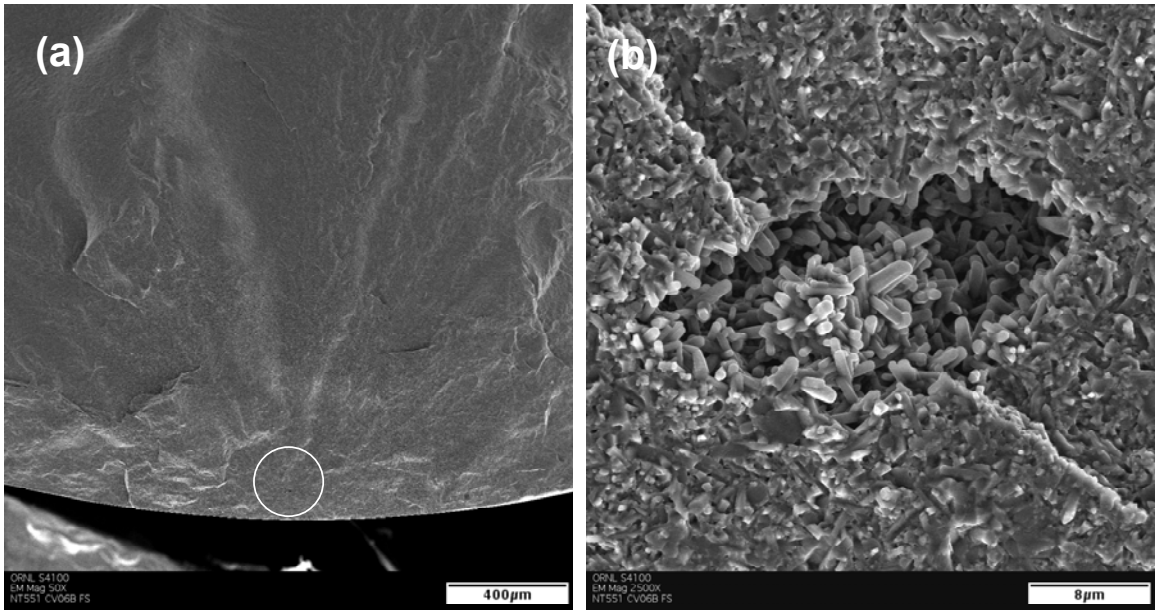

Figure 2. SEM micrographs of fracture surface of NT551 cylindrical valve stem with fracture strength of 1120 MPa after 500h bench rig test.

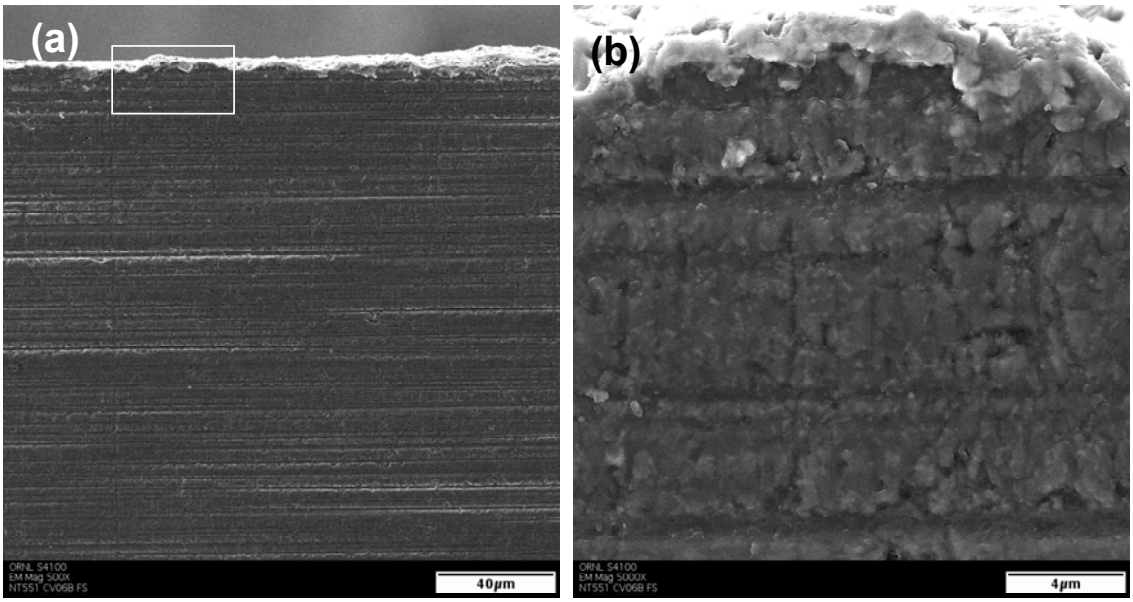

Figure 3. SEM micrographs of NT551 valve stem surface after 500h bench rig test.

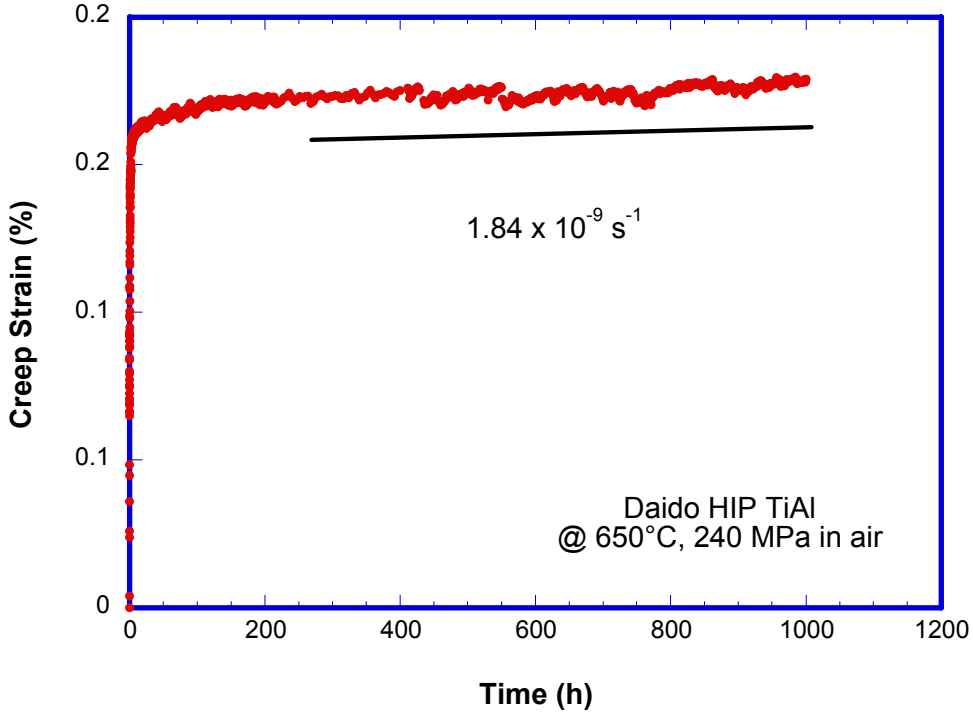

Figure 4. Creep strain versus time curve of Daido HIP TiAl material tested at 650°C and 240 MPa in air.

Lightweight Valve Train Materials

Jeremy S. Trethewey and Chad S. Logan
Caterpillar Inc.

Introduction

Valve train components in heavy-duty engines operate under high stresses and temperatures, and in severe corrosive environments. In contrast, the valve train components in the light-duty engine market require cost-effective reliable materials that are wear resistant and lightweight in order to achieve high power density. For both engine classes, better valve train materials need to be identified to meet market demand for high reliability and improved performance while providing the consumer lower operating costs.

Advanced ceramics and emerging intermetallic materials are highly corrosion and oxidation resistant, and possess high strength and hardness at elevated temperatures. These properties are expected to allow higher engine operating temperatures, lower wear, and enhanced reliability. In addition, the lighter weight of these materials (about 1/3 of production alloys) will lead to lower reciprocating valve train mass that could improve fuel efficiency. This research and development program is an in-depth investigation of the potential for use of these materials in heavy-duty engine environments.

The overall valve train effort will provide the materials, design, manufacturing, and economic information necessary to bring these new materials and technologies to commercial realization. With this information, component designs will be optimized using computer-based lifetime prediction models, and validated in rig bench tests and short-and long-term engine tests.

Program Overview

Information presented in this report is based on previous proprietary research conducted under Cooperative Agreement DE-FC05-97OR22579.

Ceramic Materials

Silicon nitride materials have been targeted for valve train materials in automotive and diesel industries since the early 1980's. Some silicon nitride material grades have reached a mature level of materials processing, capable of implementing into production. Commercial realizations have been reported in both automotive and diesel valve trains, with large-scale production underway. The silicon nitride valve train components in production are used in high rolling contact stress applications and have exhibited superior wear resistance, and longevity.

Intermetallic Materials

Titanium aluminide based intermetallics retain their strength at elevated temperature and are highly corrosion-resistant. They are lightweight, and posses high fracture toughness. These alloys are actively being investigated for several aerospace and automotive applications.

Sixteenth Quarter Summary

Engine testing of Titanium Aluminide, Silicon Nitride and production valves

One of the primary goals of this study is to evaluate the performance of ceramic (Si_3N_4) and intermetallic (TiAl) valves in an engine environment. As outlined in previous quarterly reports (see Oct-Dec 2004), arrangements have been made to perform parallel 1000-hour endurance tests on three valve materials: γ-TiAl, Si_3N_4 and the austenitic steel production valve. These tests will be performed at the National Transportation Research Center (NTRC) on a natural gas G3406 genset. Since the design of these "advanced material" valves was optimized for the less ductile nature of these materials, several modifications to the G3406 valvetrain components must be made. Significant progress has been made towards customizing the G3406 valvetrain. These modifications are outlined below:

- Seat inserts – Custom seat inserts were designed to account for the new head thickness and contact angle. These seat inserts have been fabricated by Caterpillar's supplier and are available for immediate installation.
- Valve guides – Modifications to existing production valve guides were made to account for the addition of a stem seal. Production valve guides have been modified and are available for immediate installation.
- Keeper locks – In order to mitigate the stress concentration at the keeper notch, a single keeper groove was used on the "advanced material" valve design. Production keeper locks have been modified and are available for immediate installation.
- Bridges – Custom bridges were designed to account for the shortened valve stem length. These bridges have been fabricated by Caterpillar's supplier and are available for immediate installation.

In order to begin the engine test at the NTRC, the progress of three activities must converge: custom valvetrain modifications (complete, as noted above), G3406 engine initialization at NTRC (in progress) and preliminary robustness testing on TiAl and Si_3N_4 valves (complete). Confidence that these valves will survive the heavy-duty engine environment has been established by accumulating hours on an in-house impact test rig. Each valve has been subjected to ≥ 20 hours of impact rig time with minimal detectable damage.

Pre-engine test valve characterization

Prior to subjecting the TiAl and Si_3N_4 valves to the full scale engine test, three characterization techniques have been used to gather baseline information about the valves' dimensions, material's surface quality and structural integrity. A coordinate measuring machine (CMM) profile scan was performed along the axis of each valve to verify that they meet the dimensional specifications.

In order to establish the pre-engine test surface condition, profilometry scans were performed on 5 key regions: keeper groove, Ti-6-4 stem, TiAl stem, fillet and the seat contact region. Figure 1 shows a series of roughness measurements for a single valve. It was confirmed that the surface roughness specification (Ra) was met for nearly all of the measured regions on all of the valves.

The most sophisticated set of data that was collected is the laser scatter scans performed by Dr. JG Sun at Argonne National Laboratory. The fundamental physics and experimental setup are detailed in the "NDE of Diesel Engine Components" quarterly reports. Scans were performed at

the fillet and keeper groove locations on all TiAl and Si_3N_4 valves. An additional scan of the weld region was also performed to determine if any cracks formed during the friction welding process. Figure 2 shows two scans of the fillet region of the same Si_3N_4 valve. Figure 2a shows the scan after poor finish machining. During the last quarter's efforts these valves were re-machined to meet the desired surface quality. Figure 2b shows the same valve after corrective finish machining. Valves with little or no detectable damage will be used for the engine test.

Development of a life prediction tool for advanced materials

The ongoing effort to predict the life expectancy of a heavy-duty valve subjected to typical engine loads had made significant progress in this past reporting period. The results of the first generation model were presented in a previous quarterly report (Jan-Mar 2005). Since then, the most significant accomplishment has been the shift from an axisymmetric model to a three-dimensional model. The additional degrees of freedom permit a more accurate representation of the valves deformation modes. In addition to the axisymmetric loads, the valve stem is permitted to bend and the valve head is permitted to deflect in a "pringle" deformation mode. Figure 3 shows the resultant stress field superimposed on a deformed valve. It is interesting to note that the maximum principal stresses observed on the 3D model is a factor of two greater than that observed on the preliminary axisymmetric model.

After applying the thermal and mechanical boundary conditions to the Si_3N_4-based 3D model the NASA/CARES probabilistic code was executed to examine the slow crack growth failure mode as a function of service time. Figure 4 shows the resulting life prediction curve for a Si_3N_4 valve experiencing slow crack growth under continuous G3406 genset operating conditions. Note that two curves are displayed; one represents a safety factor of one (i.e. loads are identical to those specified by the simulation-derived boundary conditions), the other represents a safety factor of two (i.e. applied loads were doubled). This 3D model is considerably more conservative than the preliminary axisymmetric model. The valve's lifetime predicted with this 3D model is substantially shorter than the lifetime predicted by the axisymmetric model (see Jan-Mar 2005 quarterly report). Even so, a probability of failure corresponding to ~0.01 ppm failed valves after one year of *continuous* operation in a heavy-duty engine is exceptional!

A couple of cautionary notes must be presented. This model relies on boundary conditions acquired from FEA simulations. Thus, they may not be exactly representative of field-tested engines. Also, this model only captures the probability of failure as a function of slow crack growth damage. As in any engineering system, several failure modes are acting simultaneously. This model focuses on the slow crack growth failure mode (prominent in ceramics). Other failure modes such as wear, impact and environmental resistance must be independently considered to gain a full perspective on the life prediction of a valve component.

Future work

The next critical milestone in this project is the execution of the engine tests at the National Transportation Research Center. At this point, the valves have been primed and the custom peripheral components have been fabricated. However there have been some struggles initializing the G3406 genset for durability testing. The multi-stage 1000-hour engine test will be performed in 1Q06. Thus, the next steps in the modeling effort include incorporating TiAl into the model and performing a sensitivity study through the use of PDS (Probabilistic Design

System). A third activity is the execution of the TiAl machining / stepped fatigue study. Materials have been procured and a test procedure has been established. Next, a test house must be selected and the test matrix must be performed. Results from this test are expected in 3Q06.

Presentations & relevant travel

None this quarter.

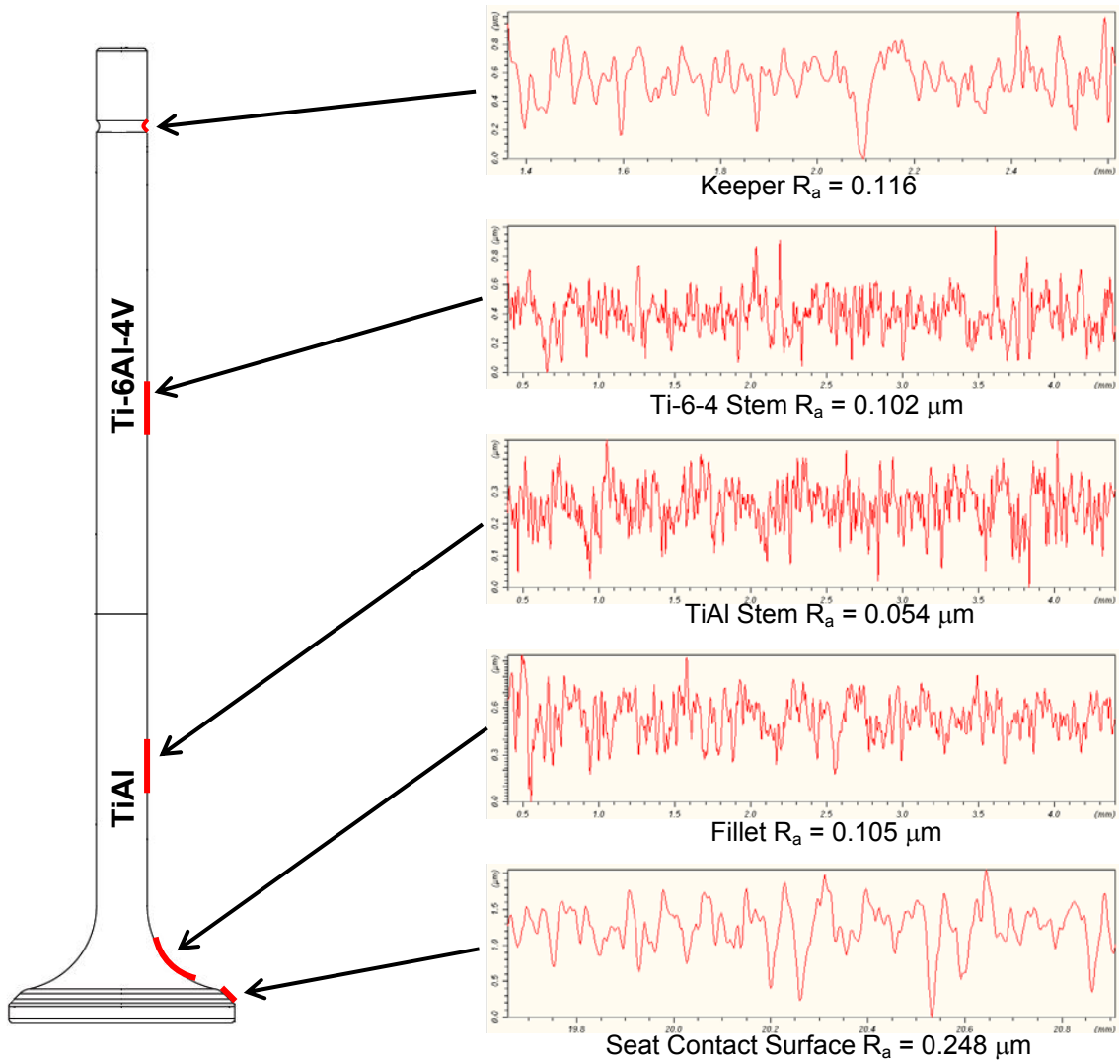

Figure 1: Surface roughness measurements on a TiAl valve. Note that scan fluxuation may not appear to correlate with the stated R_a value – this is because the plotted range for each scan is different.

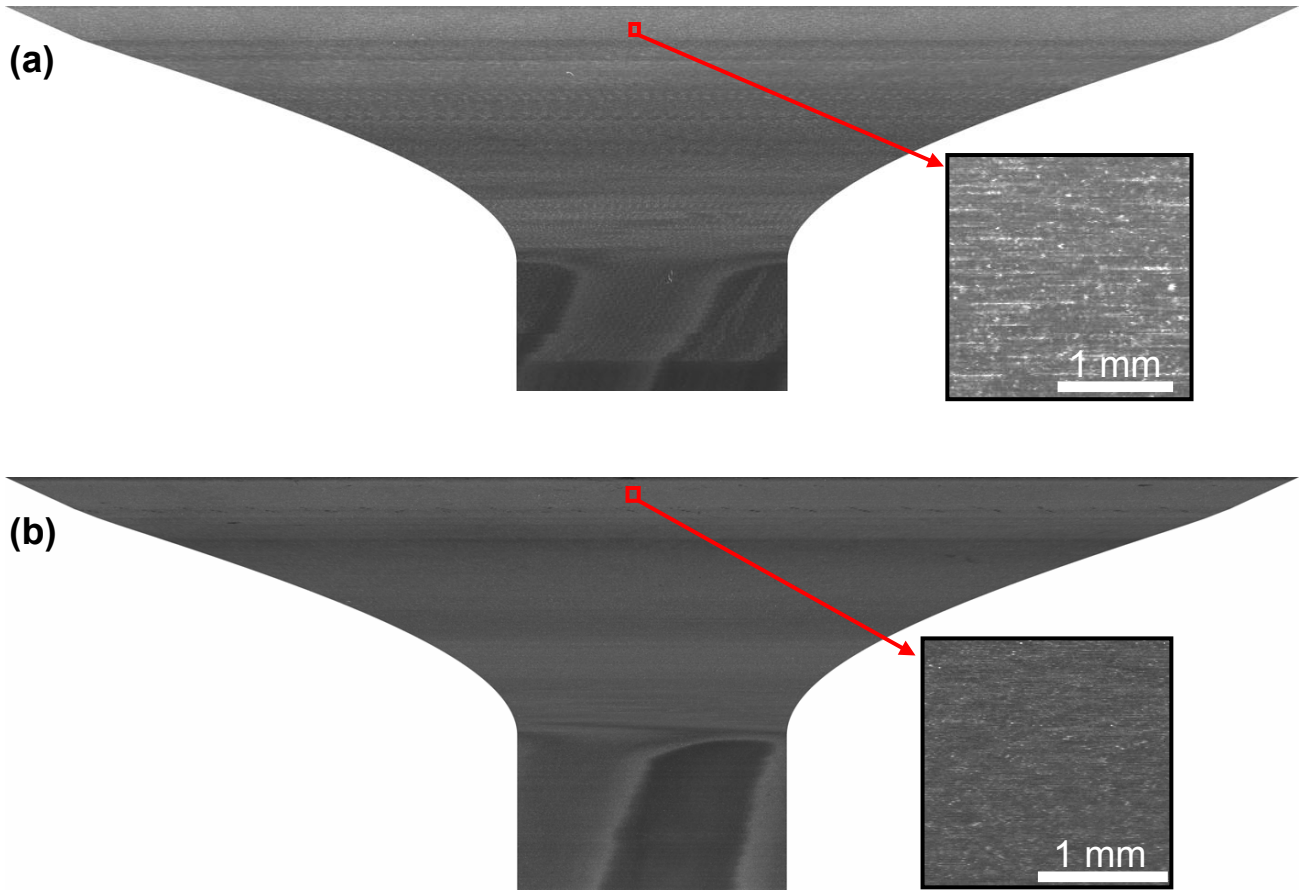

Figure 2: Laser scatter NDE scans of a Si_3N_4 valve (a) after incorrect finish machining and (b) after corrective finish machining. Note that the white streaks in (a-inset) that indicate subsurface damage have been removed by the corrective finish machining (b-inset).

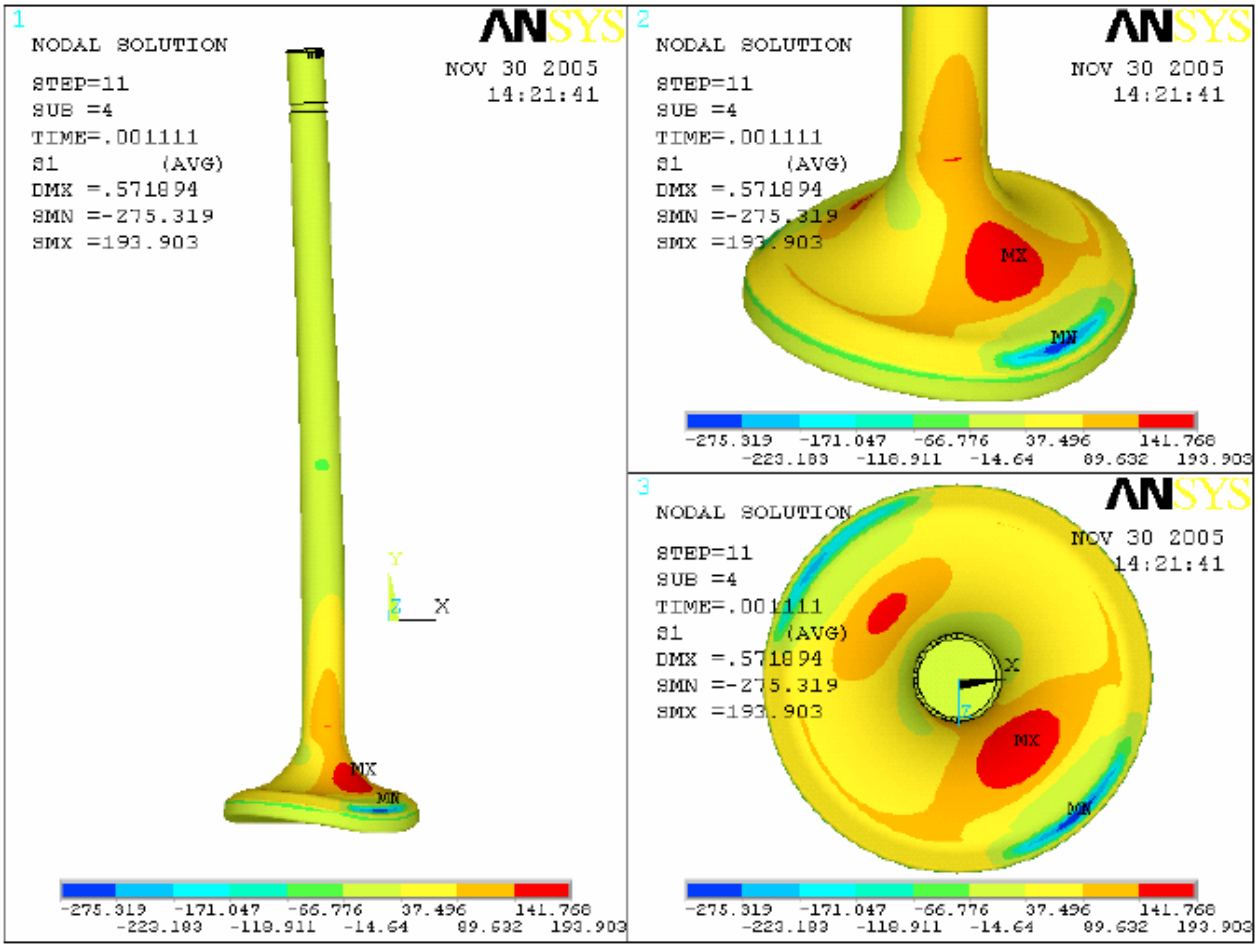

Figure 3: Principal stress field of the three-dimensional valve FEA model. Note the non-axisymmetric stem bending and "pringled" seat warping. The maximum stress observed in this 3D model is approximately a factor of two greater than the maximum stress observed in the axisymmetric model.

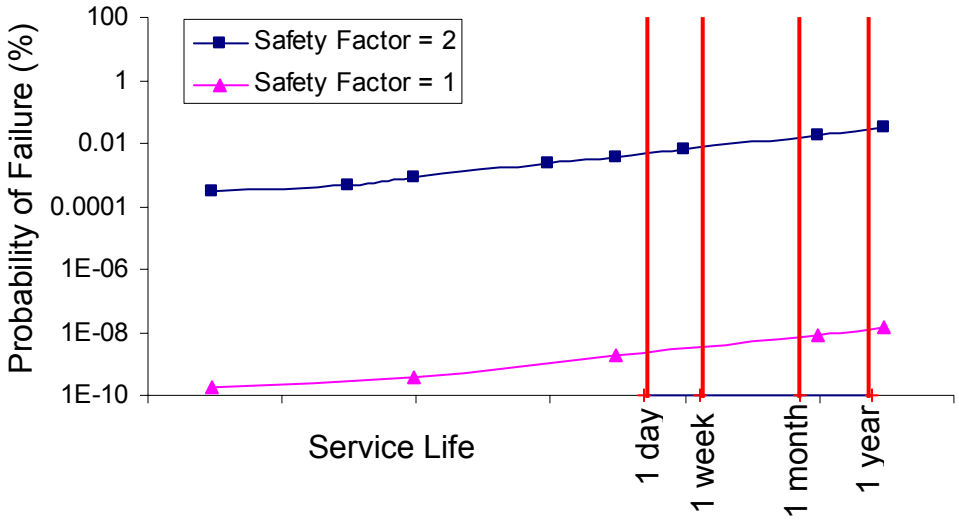

Figure 4: Life prediction curve for Si_3N_4 valve experiencing slow crack growth under *continuous* G3406 genset operating conditions using the 3D model. Note that the safety factor corresponds to a multiplication factor on the applied loads. As such, a load factor of two would generate more severe loading conditions resulting in a higher probability of failure.

Engineered Modification of Ceramics

Stephen Hsu, Huan Zhang, Yanan Liang and Charles Ying
National Institute of Standards and Technology

Objectives

- Develop design guidelines for surface texturing features that can reduce friction and enhanced durability for heavy duty diesel engine components.
- Develop cost-effective fabrication techniques for textural features
- Develop appropriate thin films and coatings to achieve synergistic and complementary relationship with texturing to enhance performance.
- Discover and develop surface chemistry for texture protection and improve friction reduction
- Develop theory and models to predict friction reduction in textured surfaces.

Approach

- Determine the effect of size, shape, pitch, and patterns of surface textural features on friction under 1) high speed, low load regime; 2) high load, high speed regime; 3) high load, low speed regime.
- Develop cost effective fabrication technologies for creating surface textural features on various surfaces including metals, ceramics, and coatings.
- Develop test methodology to measure the effects of the textures on friction
- Conduct research to develop an integrated system approach to combine the best practices in thin films, coating, and surface chemistry for performances unrealizable by individual approach alone.
- Concurrently, organize an international cooperative research program under the auspice of the International Energy Agency (IEA) to pool resources and share this energy conservation technology worldwide.

Accomplishments this quarter

- We further explored the various parameters involved in the high load, low speed contact regime. We found that number of dimples was a critical parameter under high load conditions. Many designs resulted in an increase in friction.
- To understand this phenomenon, we initiated an active modeling effort to quantify the source of friction increase. We developed an equivalent roughness concept to account for the increased stress concentration due to sharp edges from the textural features. By understanding the friction increase mechanism, we hope to device ways to consistently achieve friction reduction. This also paves the way for future design guideline development.
- The IEA IA-AMT Executive Committee was successfully convened in Porto on Oct. 11, 2005 with delegates from China, UK, Australia, Finland, Japan, Belgium, Portugal, and the US. Annex 2 was successfully concluded, annex 3 and 4 are continuing. We discussed two new activities in coatings and nanomaterials and the delegates would take the information back and seek their government's approval for formal participation in IA-AMT.
- A Special Symposium on Surface Texture was held in Porto in conjunction with COST 532 (European Cooperative Research Consortium on Triboscience and Tribotechnology) conference on Oct. 12-15, 2005 in Porto, Portugal. We had 15 speakers from 8 countries

representing academics, industry, and government laboratories describing their latest results in surface texturing in controlling friction.

Introduction

Frictional losses are inherent in most practical mechanical systems. The ability to control friction offers many opportunities to achieve energy conservation. Over the years, materials, lubricants, and surface modifications have been used to reduce friction in automotive and diesel engines. However, in recent years, progress in friction reduction technology has slowed because much obvious inefficiency has been eliminated. A new avenue is needed.

Designing surfaces specifically for friction and durability control has emerged as the last frontier in surface engineering. Recently, laser ablated dimples on surfaces have shown friction reduction properties and have been demonstrated successfully in conformal contacts such as seals where the speed is high and the load is low. The friction reduction mechanism in this regime appears to depend on the size, patterns, and density of dimples in the contact.

The objective of this project, therefore, is to develop an application specific engineered surface (combining surface textures, thin films, surface chemistry) tailored for the optimum friction reduction and durability.

Such technology is aimed at energy transmission components, cylinder liner ring contacts, cam and lifters, and overhead bearing components. To ensure that the durability criteria are met, the texture patterns have to be protected by thin films/coatings and appropriate lubricating chemistry over a broad range of operating conditions. The final outcome of the project will be a general design principle and guidelines for various engine components under a wide range of operating conditions. To achieve maximum energy conservation, this technology should be implemented worldwide through international cooperation such as the International Energy Agency Implementing Agreement on Advanced Materials for Transportation (IEA IA-AMT). Therefore, a concomitant international cooperative research under the auspice of the International Energy Agency is being conducted to pool resources from various countries to accelerate this technology development. Towards this end, UK, China, Australia, Finland, Sweden, Israel, and Japan have agreed to participate under the IEA annex IV on surface technology.

Approach

Previously, experiments were conducted to examine various surface textures on steel surfaces using photolithography and chemical etching. Using the same area coverage (% of area occupied by the surface textural features), surface features such as grooves, triangles, ellipses; circles were compared under high speed low load conditions similar to the seals operating conditions. Results suggested that: 1) surface texture size and shape had significant influence on friction; 2) orientation of the surface features with respect to the sliding direction changed the friction; 3) the primary effect of surface textures is to accelerate the transition into hydrodynamic lubrication regime. The fundamental friction reduction mechanisms in this regime, based on our work, are: a) cavitation induced pressure lift; b) back flow within the dimple; c) additional hydrodynamic lift due to the geometric shape of the dimples. There may be additional mechanisms that we have not discovered yet. Since this regime has the lowest friction, it is important to understand the

mechanisms so that when conditions are appropriate, lowest friction can be designed into the components.

From energy conservation point of view, most parasitic losses in engines take place under high load and medium to low speed conditions. Therefore, we need to extend the surface texturing concept to more severe contact conditions. However, when we ran the same surface texture patterns under boundary lubrication conditions, friction increased. A collaborative effort with Northwestern University using a sophisticated elastohydrodynamic friction model confirmed our experimental observations. Basically, under boundary lubricated conditions (high load low speed), the edge stresses around the dimple increase frictional losses as if the surface is much rougher. So there is a trade-off in this regime.

Technical Highlight

In the previous quarters, we developed a new surface textural feature with an inclined plane at the bottom of the feature to artificially generate a hydrodynamic wedge effect under plastic deformation loading; we called this elasto-plastic lubrication model. Experiments conducted demonstrated significant friction reductions for steel on steel.

L/D ratio and size effects

One of the critical issues in fabricating the new surface features was the effect of the slope at the bottom of the feature. In bearing applications, this typically was called the L/D ratio (bearing length over radius of the bearing) to estimate the lift force. We borrowed this concept and applied to our design in terms of the length over the depth of the slope fabricated at the bottom of the surface features. Another important factor was the size of the surface feature over the contact area. In boundary lubrication conditions, since the edges of the surface features served as rough spots increasing the friction, therefore, the optimum number of the features might be much smaller than the high speed low load regime. So we decided to conduct a series of experiments to investigate this effect.

We fabricate several surface features by varying the L/D ratio and the size of the surface features. Results showed that the classical wedge orientation has the highest friction reduction capacity, reducing the average friction coefficient of the untextured (UNT) from 0.09 to about 0.05, a 44% decrease in a 52100 bearing steel on 52100 bearing steel contact.

We continued our experimental approach by increasing the number density of the patterns and shrinking the sizes at the same time on steel on steel couples. Results were disappointing in that as the number of features increased, friction reduction tend to decrease or actually increase. Since the fabrication of tightly controlled samples was labor intensive, we decided to explore the theoretical modeling approach to identify the source of friction increase in parallel to the ongoing experimental optimization.

Theoretical model development

When one considers creating dimples or other features on the surface, there are several processes going on simultaneously under high load low speed conditions: a) removal of contact area, which

increases the mean contact pressure; b) contact stresses around the edges of the dimple increases under high contact pressure; c) fluid inside the dimple is squeezed and pushed from the deformation induced dimensional change in the sliding direction generating hydrodynamic and hydrostatic pressures inside the dimple providing lift. These processes involve contact mechanics, fluid dynamics, materials deformation, and fluid flow analyses. Conventional fluid mechanics model would not be able to describe and predict the friction reduction process.

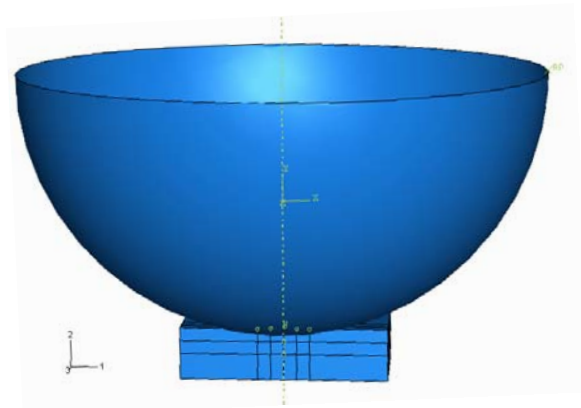

Fig. 1. Schematic of the contact under boundary lubrication regime

Our first attempt in developing a mechanistic model is to quantify the friction increase mechanisms due to increased mean contact pressure and the edge stresses. We developed a finite element model to describe the hydrostatic pressure and stress distribution of an elliptical dimple on a flat surface. Based on the stress distribution on the surface, we can then calculate "equivalent roughness" surface features that would generate similar stress patterns. Using this model, we can systematically examine the effects of geometric shapes on stress distribution and quantify the friction increase under boundary lubrication conditions.

With the surface profile of an elliptical dimple digitized on a regular grid, a numerical scheme was developed [1] to solve the following equations:

$$g_{ij} = h_{ij} + u_{ij} - u_0 \quad \text{or} \quad \mathbf{g} = \mathbf{h} + \mathbf{u} - u_0 \tag{1a}$$

$$u_{ij} = \sum_l \sum_k K_{k'+i-k,\, l'+j-l} p_{kl} \quad \text{or} \quad \mathbf{u} = \mathbf{A}\mathbf{p} \tag{1b}$$

$$\sum_i \sum_j p_{ij} = P_0 \quad \text{or} \quad \mathbf{q}^t\mathbf{p} = P_0 \tag{1c}$$

where **h** is the gap between the surfaces just prior to any deformation, **u** is the composite surface displacement under the applied force F_0, **g** is the gap after the deformation, **p** is the interfacial pressure, u_0 is the rigid normal approach of one body to the other, P_0 is defined by $F_0 = \Delta x \Delta y P_0$, **q** is a vector of ones, and **A** is the influence coefficient matrix. The influence coefficient $K_{k'+i-k,\, l'+j-l}$ describes the relationship between the normal displacement at the center of an element and constant pressure over another element.

Within the model, we accounted for the contact pressure increase due to the decrease in contact area and we calculate the hydrostatic stresses generated by the edge of the dimples without sliding.

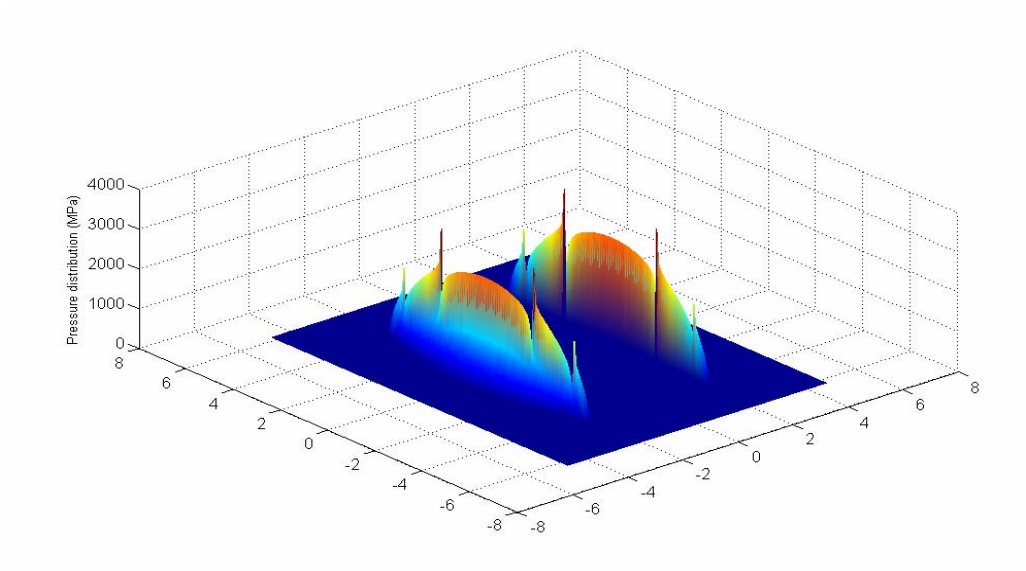

Fig. 2. Contact pressure profile associated with two elliptical dimples on a flat surface

Figure 2 shows the contact pressure calculated from the dimple edges using the numerical simulation model described above. Based on this contact pressure, one can then calculate the equivalent roughness that will generate such contact pressures. Figure 3 shows the reconstructed configuration for one and multiple (four) dimples.

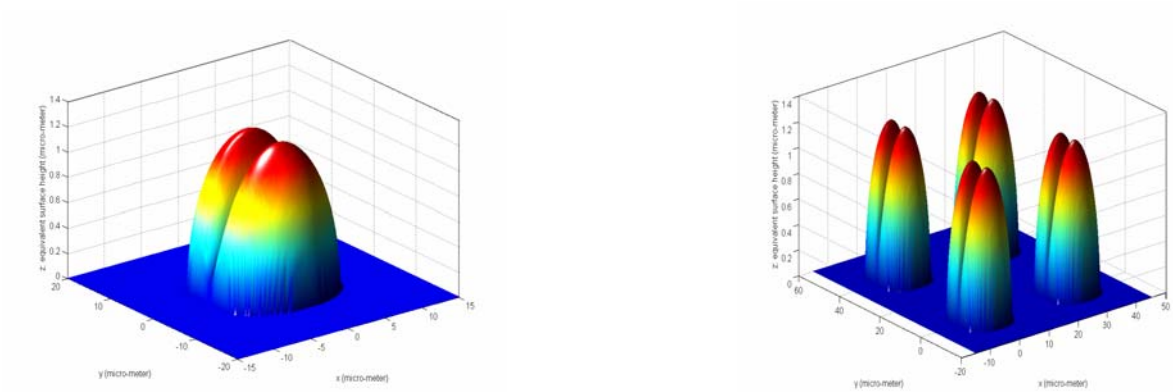

Fig. 3. Reconstructed surface roughness based on contact pressure for a) a single dimple; b) four dimples arranged in an equal distance pattern.

Translating these hypothetical bumps into a composite three dimensional roughness description creates multiple possible solutions depending on the roughness descriptors used as well as the trade-offs between height and frequency distributions. Based on our own data, as well as the theoretical model results from Eaton/Northwestern University virtual texturing program, we can correlate the equivalent roughness number increase over the baseline and quantify the friction increase using Fig. 4.

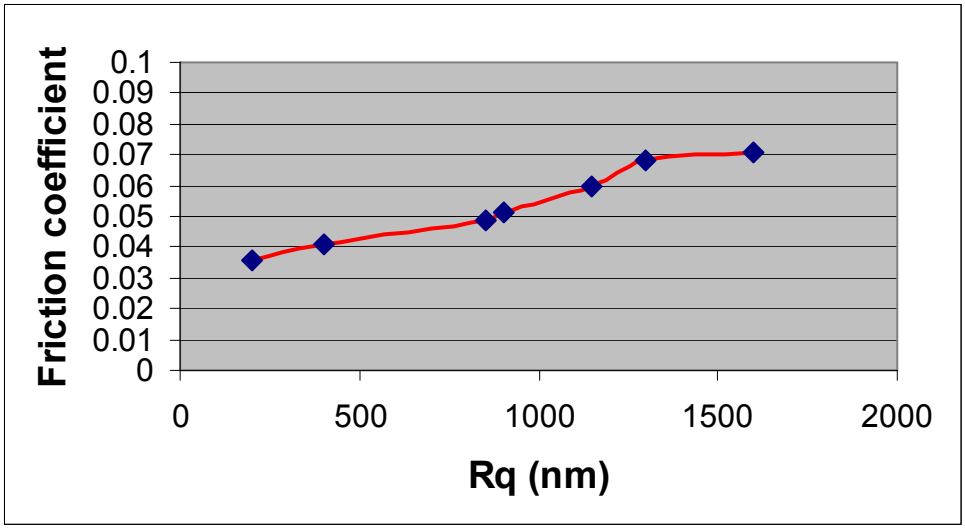

Fig. 4. Correlation plot of friction coefficient as a function of surface roughness Rq

Using one of our data set with a baseline untextured surface friction coefficient of 0.05 at a surface roughness Rq of 900 nm, the friction increase due to edge stresses for a typical pattern of 7% surface density coverage, the equivalent roughness would yield a coefficient of 0.58.

This model allows us to vary the angle of the dimple edge, size of the dimple, and distribution of the dimples inside the contact area to assess the intrinsic friction increase under boundary lubricated conditions. The next step will be to incorporate sliding directions and speed to include the kinetic effect.

Reference

[1] Allwood, J., 2005, "Survey and performance assessment of solution methods for elastic rough contact problems," *ASME J. of Tribology* **127**, pp.10–23.

Publications/Presentations

Presentations:

S. M. Hsu, "An integrated surface modification technology: project review," DOE project review, Oak Ridge National Laboratory, Oak Ridge, Tennessee, Sept. 13-15, 2005.

S. M. Hsu, “Integrated Surface Modification Technology: a progress report,” COST 532 symposium on surface textures, Porto, Portugal, Oct. 12, 2005.

Publications:

“Surface Texturing: Comparison of Various Geometric Shapes on Friction under High Speed Low Load Conditions,” Wang, X., Hsu, S.M., published in the proceeding of the International Tribology Conference, Kobe, Japan, May 29-June 2, 2005

“Surface Texturing: A New Design Principle for Friction Reduction Under Boundary Lubrication Conditions,” Wang, X., Hsu, S.M., published in the Proceedings of the International Tribology Conference, Kobe, Japan, May 29-June 2, 2005.

Testing Standards

George Quinn
National Institute of Standards and Technology

Objective/Scope

This task is to develop mechanical test method standards in support of the Propulsion Systems Materials Program. Test method development should meet the needs of the DOE engine community but should also consider the general USA structural ceramics community as well as foreign laboratories and companies. Draft recommendations for practices or procedures shall be developed based upon the needs identified above and circulated within the DOE engine community for review and modification. Round robins will be conducted as necessary. Procedures will be standardized by ASTM and/or ISO.

Technical Highlights

1. General

The first draft of a Guide to Practice for Fractography is now about complete. Work on split cylinder flexure testing concluded and a paper was prepared for the Cocoa Beach Ceramics Conference and for ASTM Committee C-28, Advanced Ceramics. Intensive work resumed on prestandardization testing of solid rods. A review paper on the shortcomings of the Vickers indentation crack length method for fracture toughness was prepared.

2. Fractography

The first draft of a NIST user-friendly "Guide to Best Practice" for fractographic analysis was completed. This document will be over 500 pages long when printed, and will be a valuable resource to engineers, researchers and student. It has 677 figures illustrating key fractographic markings in ceramics and brittle materials. It is very practical and is meant to help users solve problems. It will complement the ASTM standard C 1322, Standard Practice for Fractography and Characterization of Fracture Origins in Advanced Ceramics. It is now being reviewed at NIST. It is expected to be published by the summer of 2006, in time for the quinquennial conference on Fractography of Glasses and Ceramics organized by Alfred University and Mr. Quinn. An important spin off of the Guide to Practice is a detailed appendix on How to measure Fracture Mirrors. This appendix is meant to be a guide to users on how to measure these important fracture markings on broken brittle materials. **Figure 1** shows fracture mirrors in ceramics. The size of the mirror is inversely related to the stress in the part at fracture. Hence, the mirror size is an important

(a)

(b)

(c)

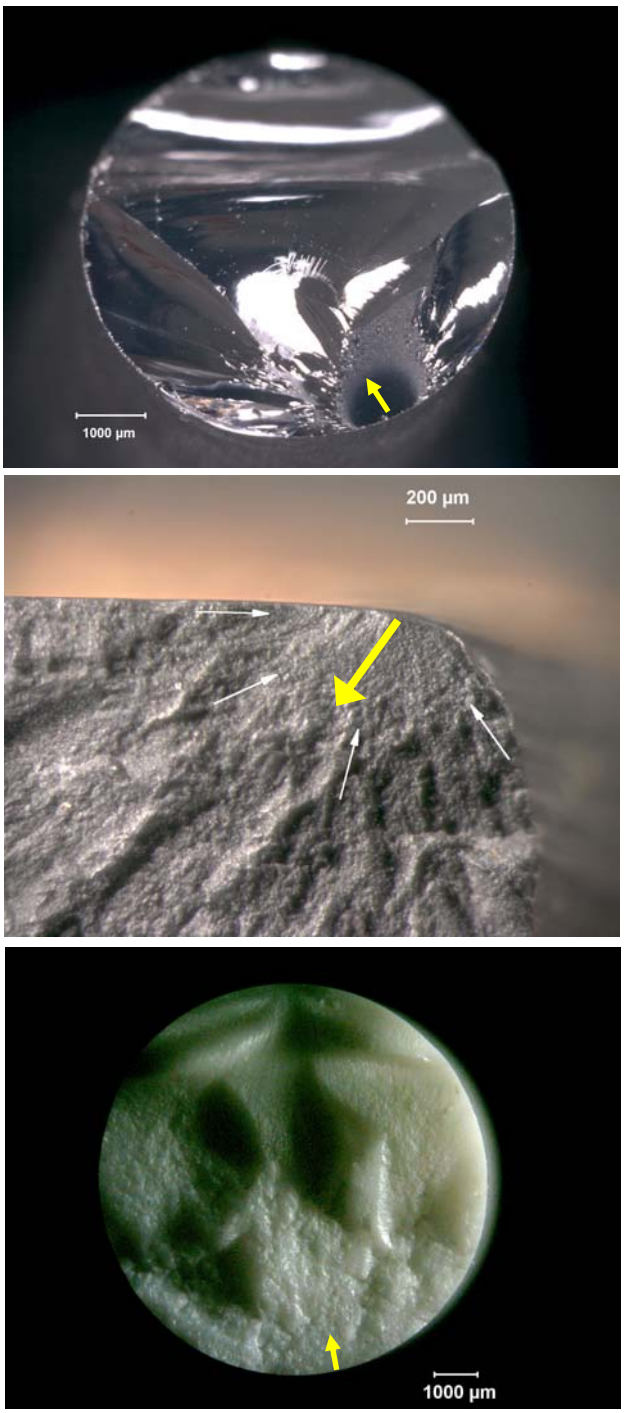

Figure 1. Mirrors in glass and ceramics. The size of the mirror can be used to accurately estimate the stress in the part at failure even if there is no other information available. Guidelines on how to judge the mirror size are included in the new NIST Guide to Practice. (a) shows a glass rod, (b) shows a silicon nitride model turbine rotor, (c) shows a zirconia fuel injector pin blank rod piece broken in 3-point flexure.

diagnostic and forensic tool to analyze the stresses in a broken part, even if the engineer has no other knowledge of how the part was loaded. Mirror measurements are also valuable for materials science research and material development.

The new Guidelines are the first step towards a possible ASTM standard. The Guidelines are being reviewed by a few selected expert fractographers. A paper on this topic will be presented at the July 2006 Fractography conference, at which time Mr. Quinn will solicit feedback and criticisms form the assembled world experts. If a consensus can be reached, then the guidelines will be written in ASTM standard format and submitted to ASTM Committee C-28 for review.

3. Flexural Strength Testing of Cylindrical Ceramic Specimens

Intensive work resumed on this subtask this quarter in conjunction with the split cylinder testing described in the next paragraph. In the last year, we learned that a shock–pulse in the fixture when the ceramic test pieces broke was the cause of the observed small deformations in the cradles used to distribute the load to the round test piece so as to avid severe contact stresses at the loading points. **Figure 2** shows our dedicated fixture for testing round specimens. It has been used extensively in a kind of "beta testing" program during

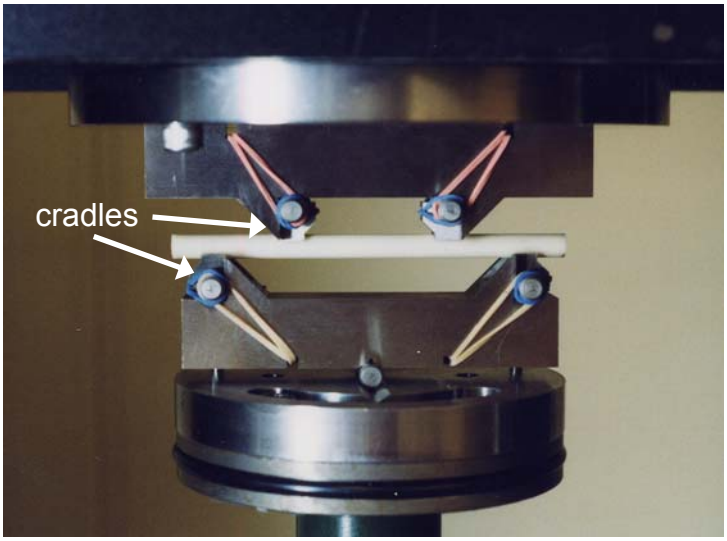

Figure 2 40 x 80 mm span flexural bend fixtures with a ceramic rod specimen in place. Four cradles apply load to the specimen and minimize contact stresses. This quarter we optimized the design of this fixture. Steel dowel rod dummy specimen in the same four-point bend fixtures that were used to test split cylinder specimens as described in section 5 below. Special cradles hold the round specimens in the fixtures that are normally used to test rectangular bend specimens. Slight deformations on the cradle edges were observed after the ceramic strengths tests described below.

the late 1990s when we were evaluating grinding and machining damage in engine grade ceramics. Drawings or schematics of the fixture have been given to ORNL (A. Wereszczak,), U.S. Army (Jeff Swab), NASA-Glenn (J. Salem) and GE Schenectady (Reza Sarrafi). Indications are that they have had positive experiences with the design. Our cradles were refined and we got some new ideas for how users could make their ordinary bend fixtures perform the same task if they use a simple modification.

4. Split Cylinder Flexural Strength Testing

We finished evaluating Carpenter company zirconia rod specimens that we received from Cummins. Some of these were split into two halves and each half was tested as shown in **Figure 3**. The four-point testing was with effective spans of 20 x 40 mm. The three-point was also with a 40 mm span. The strength outcomes are shown in **Figure 4**. Three-point strength numbers for the same batch of material that were obtained by Cummins on full cylindrical rods are also shown in **Figure 4** for comparison. **Figure 5** shows some fracture origins. The good news is that the 3-point strengths of the split rods are nearly identical to those of the full rods. The 4-point strengths are almost exactly the predicted shift in accordance with Weibull strength size scaling. We completed a full fractographic analysis of all these specimens. A full paper on this topic was prepared for the Engineering Ceramics Division meeting of the American Ceramics Society in Cocoa Beach in January 2006.

Figure 3 Split-cylinder strength tests were conducted on zirconia rods that had been sliced in two lengthwise.

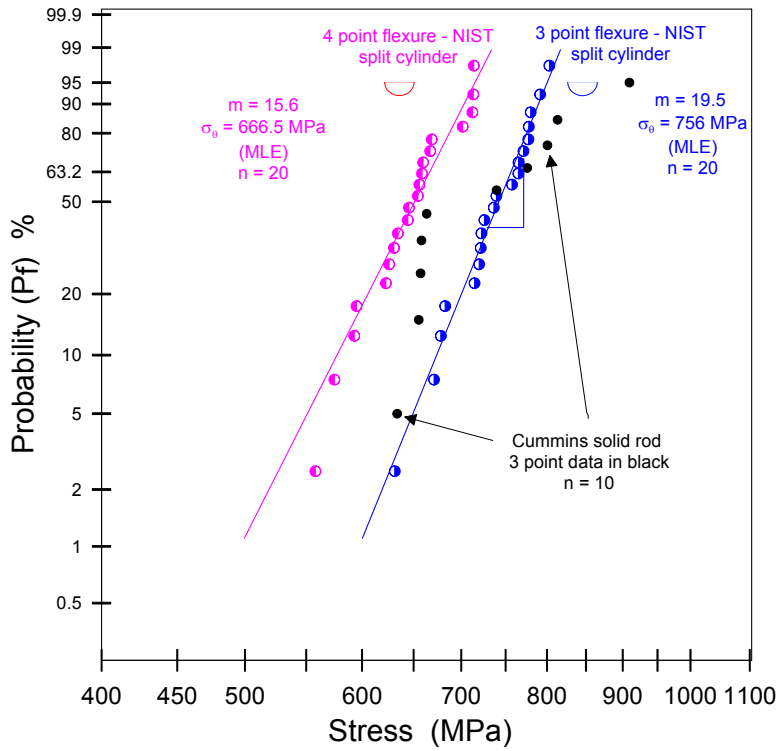

Figure 4 Flexural strengths of split zirconia rods tested measured at NIST and solid rods tested at Cummins. Maximum likelihood parameter estimates are noted. The two distributions are very similar and are shifted in accordance with the customary Weibull size effect. The three-point strengths are in superb agreement with the Cummins solid rod data.

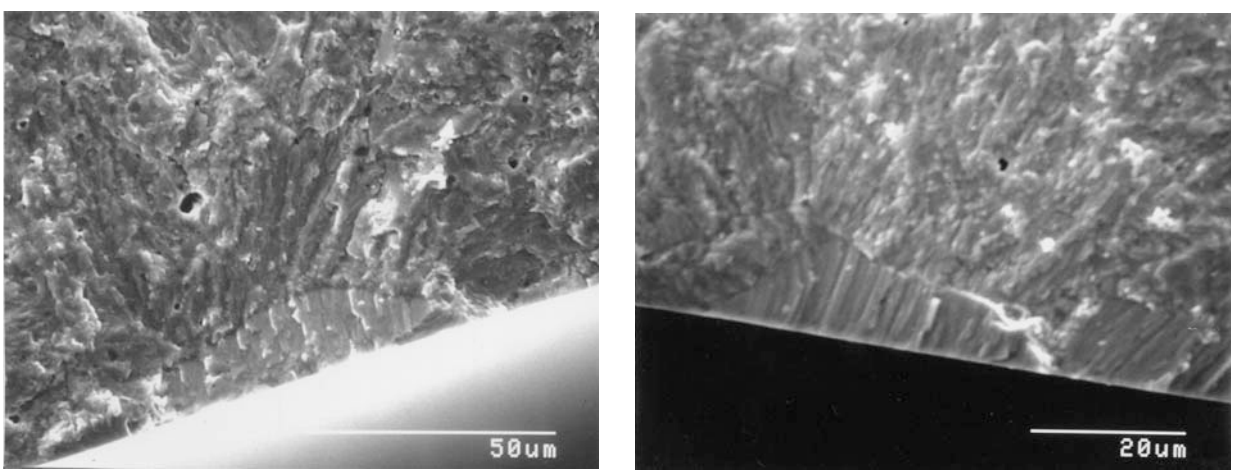

Figure 5. Fracture origins in a carpenter zirconia split rod specimen. Most of the fracture origins were faulted cubic zirconia grains located right at the surface. Evidently the aligned tetragonal precipitates in these cubic grains transformed to monoclinic phase, created the stacked deck of cradle appearance to the faulted grains. Flaw pockets were noted in the zirconia, but the surface grinding seems to have triggered some grains to transform and act as strength limiting flaws.

We also did many tests on rods of various materials and sizes and shapes. **Figure 6** shows some examples. In some cases we were simply trying to verify that our new fixture design was suitable for these alternative cases, but we also did a series of experiments with ordinary bend fixtures designed for rectangular bars. These fixtures were in conformance with ASTM C1161 and MIL STD 1954 ands ISIO 14704 for rectangular bars, and we reasoned that many users already have these and would be apt to use them on solid rods. We are becoming adept at interpreting the fracture patterns in these, both for valid breakages and invalid breakages. The latter have telltale characteristic and this will be valuable (in some sort of appendix) in our planned ASTM standard to help users understand whether or not their tests are successful. For example, **Figure 7** shows broken glass rods that were tested similar to solid rod zirconia fuel injector pins. The glass rods broke 50% of the time from the <u>outer loading</u> pins, even though in principle there is negligible stress at that location. The cause of fracture was cone cracks generated by the crossed roller configuration (round specimen resting on a round roller).

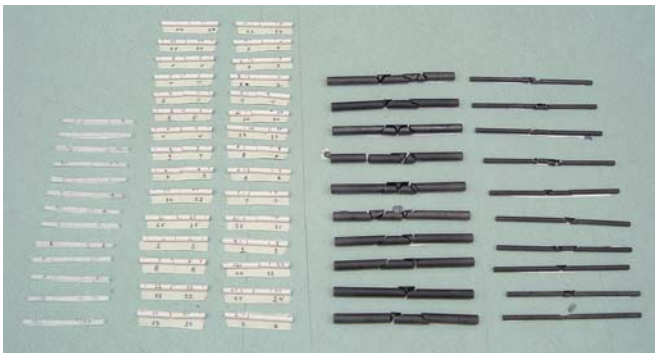

Figure 6. Broken rods.

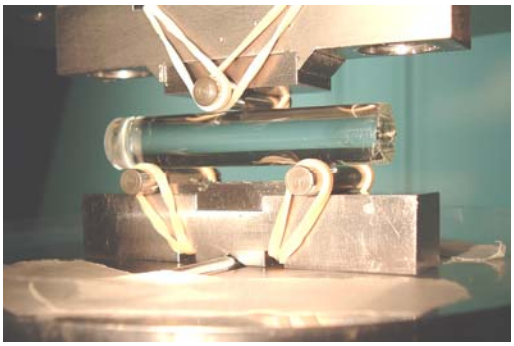

Figure 7 Broken glass rods. The first on the right was a legitimate break, but the other three were invalid. They broke from the outer loading points due to contact cracks. An even larger contact crack formed in the middle from the mid loading rollers, but since it was on the compression side of the specimen it was relatively harmless. See the next **Figure 8** for a three dimensional view.

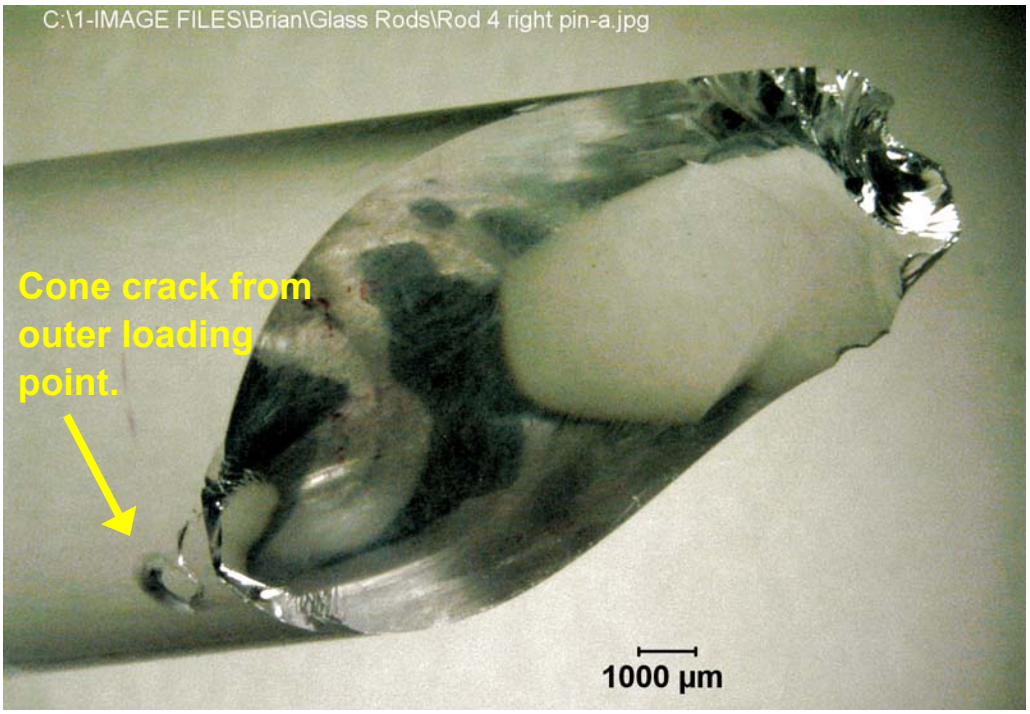

Figure 8. Invalid broken glass rod

Incidentally, such invalid breaks were not detected in the zirconia rods of similar size and shape, since they were much stronger and resistant to cracking. The zirconia rods did have cone cracks at the middle top loading point, but these were docile. Our goal with these tests was not to measure the strength of glass, but instead to explore the bounds of valid testing configurations. This is an essential step in crafting a standard.

We also tested a number of alpha silicon carbide rods left over from the ceramic machining consortium program. We have hundreds of these in the as-fired state, and they may be suitable for a round robin if one is needed for the ASTM standard. We broke 30 test pieces in the fixture with cradles and 30 in the fixture without cradles. Both sets produced nearly identical results. This plus, what we have learned about the testing of the large chunky zirconia rods is leading us to believe that cradles may not always be necessary. If so then user will be able to go right ahead and test rods on their normal test fixtures. Our final work on this task should be complete in the next 3 months, at which time we except to have the answers to these questions. Ultimately, the ASTM standard will allow uses to either:

a. Test using their normal fixtures with a simple cradle adaptor,
b. Test using their normal fixtures without any adaptations or cradles.
c. Test using a specially designed fixture for round rods,

5. Diametral Compression

No progress this quarter.

6. Fracture Toughness

A review paper was prepared for the Cocoa Beach meeting. It is very critical of the Vickers indentation cracks length method. The goal of the paper is to alert users to the drawbacks and inaccuracies of this method. This should be a controversial presentation. Dr. Edgar Lara-Curzio of ORNL invited Mr. Quinn to make this presentation.

Status of Milestones

412149 Prepare ballot-ready first ASTM draft of cylindrical rod flexure strength test — Overdue, New schedule May 2006

412151 Prepare review paper on flexural testing of cylindrical rods. — Overdue, New schedule Fall 2006

Communications/Visits/Travel

G. Quinn communicated with Cummins engineers regarding strength testing of round zirconia rods.

Mr. Quinn participated in the DOE Heavy Duty Vehicle Materials Program, review at ORNL in September 2005 and met wit a variety of engine company engineers and ORNL personnel.

Publications and Presentations

1. G. D. Quinn, "Segmented Cylinder Flexural Strength Test," submitted to Ceramic Eng. and Sci. Proc., Jan 2006, Proceedings of the Cocoa Beach January 2006 Conference.

2. G. D. Quinn, "Fracture Toughness of the Vickers Indentation Crack Length Method; A Critical Review," submitted to Ceramic Eng. and Sci. Proc., Jan. 2006 Proceedings of the Cocoa Beach January 2006 Conference.

IEA Annex on Materials for Transportation Applications

M. J. Lance and A. A. Wereszczak
Oak Ridge National Laboratory

Objective/Scope

Next generation thermal barrier, tribological, and environmental barrier coatings will enable enhanced diesel engine performance, higher operating efficiency, longer engine lifetimes, and lower emission of NO_x and particulates. Unfortunately techniques for assessing properties, particularly with respect to coating interface, are unproven. The sought attributes (thermal protection, improved wear resistance, and environmental barrier) of any of these coating applications can only be realized if their architecture is appropriately designed to withstand operating or service stress states. This project explores new, innovative, and promising test and characterization techniques that crosscut all these coating systems and whose results and interpretations will expedite their development and exploitation in the heavy vehicle sector.

Technical Highlights

Coating Evaluation Test Techniques

Several test and analytical techniques are being surveyed and explored to characterize coating performance. Their prospective utility will be described at the next IEA Executive Committee Meeting (to be held in May in Calgary), and potential collaborations and round robin testing with IEA IA-AMT members and participants will be solicited. In the initial stages, the use of in-house coating characterization capabilities at ORNL will be advocated. These include:

- *PiezoRaman spectroscopy*. Raman spectra are non-destructively collected on coatings comprised of ionic or covalently bonded materials. Peak shifting in the spectra are linked to stress enabling the coating manufacturer or end-user to better understand stress states (e.g., residual, etc.) in their coatings and improve them. The technique can measure stress states at fine resolutions facilitating the evaluation of thin films and coatings.
- *Laser shock spallation*. A shock pulse (e.g., ~ 20 ns peak width) is impacted on a substrate sending a compressive shock wave through it to the opposite end that has a thermal barrier, tribological, or environmental barrier on it. The compressive shock transmits through the coating and reflects off the free surface as a tensile stress wave. If the magnitude of the tensile wave is sufficiently high, then coating spallation is produced. The size of the spall and shock pulse conditions can be married to shock wave modeling to determine interfacial strength.
- *Microindentation of innovative test coupons of coatings*. Instrumented indentation test facilities can be combined with special designed coating test coupons to evaluate interfacial properties. Facilities can be extended to in-situ indentation whereby deformation processes are examined under an indenter with the indenter also serving as the objective lens to a microscope or PiezoRaman spectroscope.
- *Scratch adhesion testing*. Instrumented scratch testing facilities have the potential to be adapted to measure adhesion properties of coatings. The pendulum-based scratch tester is equipped with two high frequency load cells that monitor normal and transverse forces on the scratch tester's diamond tool. Those force responses can be used to interpret coating properties and scratch adhesion.

- *Hot hardness testing*. The hardness of coatings can be measured at elevated temperatures to assess how temperature affects contact damage resistance.
- *μ-FEA*. Microstructural finite element analysis can be used to assess stress states and coating architecture through the simple input of digital pictures capturing the coating microstructure. Knowledge of service boundary conditions or imposed or measured boundary conditions (e.g., those measured with an infrared camera) can be combined to effectively predict stress states and identify problematic coating architecture designs.

Survey
A questionnaire is under development to distribute to materials and coating scientists working at diesel engine manufacturers or component OEMs. Goals are to use the information from survey responses to identify pressing contemporary needs in the area of coating evaluation and performance.

Status of FY 2006 Milestones
Survey innovative test techniques that facilitate the coating performance and evaluation of thermal and tribological coatings. [09/06] *On schedule.*

Communications/Visits/Travel
Wereszczak participated in the 2005 IEA Executive Committee Meeting held 11 October 2005 by giving three presentations that overviewed IEA Annex II efforts, IEA Annex III on rolling contact fatigue, and proposed a new annex on coating evaluation and performance. Participants from other US federal agencies (USDOE, NIST, NSF), Belgium, United Kingdom, China, Finland, Japan, Portugal, Australia, and Switzerland attended the IEA meeting.

Publications

- Burner Rig Round Robin - Subtask 13, Final Report, M. K. Ferber, Oak Ridge National Laboratory, September 2005.
- Co-Operative Program on Ceramics for Advanced Engines and Other Conservation Applications, Final Report, Oak Ridge National Laboratory, M. K. Ferber, September 2005.
- International Energy Agency Implementing Agreement for a Programme of Research and Development on Advanced Materials for Transportation Applications, 2004-2005 Annual Report, M. K. Ferber.

References
None.

IEA - Rolling Contact Fatigue

A. A. Wereszczak, H. -T. Lin, and M. J. Lance
Oak Ridge National Laboratory

W. Wang
Bournemouth University

O. M. Jadaan
University of Wisconsin-Platteville

Objective/Scope

The understanding and control of contact damage behavior of ceramics under rolling and sliding conditions are enablers to more widespread utilization of ceramics in hybrid bearings, cam followers, valves, valve seats, and other important transportation-related components. International interest exists to understand the fundamentals of rolling contact fatigue (RCF) of ceramics and coated metals because greater control (or minimization) of RCF will result in longer life of such components. Rolling contact fatigue is internationally studied through a variety of test methods and analytical approaches; interest exists in the present project to link their measured performances. Toward that, RCF studies (primarily of Si_3N_4) involving both international and domestic interactions are being pursued in Annex III of the International Energy Agency (IEA) agreement.

Technical Highlights

C-Sphere Analysis

Silicon nitride (Si_3N_4) balls for use in hybrid bearings have been shown to extend rolling contact fatigue (RCF) lifetime, reduce the dynamic loading in high-speed roller element applications because of their lower density (compared to historically used steel balls), and enable bearing use in more corrosive and higher temperature environments [1-3]. Many parameters such as density, hardness, elastic modulus, fracture toughness, 3- and 4-pt flexure strength and Weibull modulus, crushing strength, grain size and secondary phase morphology, porosity, and surface finish have been extensively studied in an effort to improve or predict RCF performance of Si_3N_4 balls [1-7]. As an outcome of many of those studies, ASTM F2094 [8] was developed and that specifies allowable minimums and maximums of many of those properties and finish conditions.

Surprisingly little or no study has been devoted to the quantification of sub-surface inhomogeneities (e.g., damage due to machining, residual effects from glass encapsulation used during hot-isostatic-pressing, etc.) and what effect they could have on RCF performance. Such sub-surface inhomogeneities usually play a dominant role in the performance (strength, fatigue, etc.) of structural ceramics. Their study in structural ceramics is typically facilitated using simple tensile or flexure strength specimen geometries that enable the concurrent measurement of strength and strength-limiting flaw size (latter identified through fractographical practices). However, for ceramic spheres, a likely historical barrier of their use to study strength-flaw-size relationships is the inherent geometry of the sphere itself; namely, it is nearly impossible to mechanically load a ceramic ball in a manner to produce a predictable tensile stress field at the sphere's surface sufficient to cause its fracture. Loading a ceramic sphere diametrally produces

two Hertzian contacts and ring- and cone-crack initiation can occur and ultimate fracture can result if the contact stresses are sufficiently high; however, the evolution of ultimate fracture with this test makes the study of strength limitation from inherent flaws or other inhomogeneities located at the surface nearly impossible. Additionally, the fracture of brittle spheres from diametral compression occurs at such high loads (i.e., a great deal of stored energy exists in the sphere at fracture) that the test coupon disintegrates into fine rubble [9] rendering fractography nearly impossible, and thus, inhibiting the study of the relationship of strength-flaw size.

A new test coupon called the "C-sphere" flexure strength specimen was developed at Oak Ridge National Laboratory (ORNL) under the Heavy Vehicle Propulsion Materials Program to enable the study of and measurement of a strength and linked flaw size. Enabling the identification of a flaw type (usually surface- or near-surface-located) and measurement of its size in finished ceramic balls is indeed important for the study of strength, but more importantly, for the study and predictability of RCF performance (a response limited by surface- or near-surface-located flaws or in changes thereof). Hadfield [10] reported that a critical depth of ring cracking in RCF is 5-20 microns below the surface; the C-sphere specimen is ideal for studying that near-surface depths.

The C-sphere specimen is produced through the controlled slotting of a ceramic sphere. It is then diametrally loaded (or flexed) to initiate fracture at the sphere's surface. The C-sphere is analogous to a "C-ring" flexure specimen that is produced through the slotting of a ceramic ring. A description of the C-sphere flexure strength specimen follows and a comparison of the C-sphere flexure strength distributions of two commercially available Si_3N_4 bearing grade materials is presented.

To work toward an optimized C-sphere geometry, a finite element analysis (FEA) model was created in ANSYS. The testing of the common ball diameter of 12.7 mm (0.50 in.) was the focus. Candidate slot widths of 3.175 mm (0.125 in.) and 6.35 mm (0.25 in.) were considered because they are common sizes for grinding wheel thicknesses, and the C-sphere machining would therefore likely be economical and have associated quick turn-around time. Slot depth was varied until a slot-width-slot-depth combination produced at least a 10-times higher outer-fiber surface tensile (hoop) stress than any other surface tensile stress located elsewhere on the coupon. The geometry of the final C-sphere is shown in Fig. 1. An offset between the original ball's center-line and the center-line of the 3.175 mm radius was deemed necessary; if the offset is zero or too small, then significant tensile stresses are created on the C-sphere's interior and a high likelihood that fracture would be initiated there because of both the high tensile stress and relatively rough surface finish produced by the grinding wheel. The final offset size (0.635 mm) produced a C-sphere that, when diametrally compressed (see Fig. 1), produced an outer-fiber tensile stress much larger than that on the ground interior and therefore a high likelihood that fracture would (desirably) occur there.

A quarter symmetry model for the C-sphere flexure strength specimen was optimized and is shown in Fig. 2. Solid95 tetrahedral elements were used and a 100 N point load was applied to the C-sphere's apex. Several iterations of mesh density were evaluated. The resulting mesh contained 52703 elements and 76682 nodes, and a fine mesh density in the region where high tensile stresses would develop gradually getting coarser towards the area where the load was applied and in the overhang portion.

The issue of artificially high stress concentration within the narrow zone under the applied point load and its effect on the computed effective sizes was considered. This is an idealization of what physically takes place where distributed load acting over a narrow area is actually applied. In other words, as the mesh gets finer the stress under the load will increase indefinitely making the model and hence the effective sizes mesh dependent. To understand the issue of stress singularity under the point load, both nodal and element first principal stress distributions were studied. A nodal plot smoothes the stress distribution by averaging the stresses at that point in all the elements having that node in common. This smoothing is masking the very high stresses taking place within the individual elements, which if not removed would yield erroneous effective size calculations. This is because when the effective size is computed, the stress distribution is normalized with respect to the maximum effective stress in the component. If this maximum effective stress were incorrect, due for example to a localized stress concentration, as is the case for this model, then the computed value would be incorrect. In order to unmask the high nodal stresses, element stress plots are used which display the actual nodal stresses as computed for each element.

In order to take out the effect of localized stress concentration on the effective size calculations, the artificially high stressed elements under the load point were removed. The remaining elements, comprising the vast majority of the specimen, were then used to assess the specimen's effective area and effective volume. The nodal and element stress distribution plots for the C-sphere model, with the highly stressed elements carved out are shown in Fig. 3. One would then observe from these plots how the maximum tensile stress of 132 MPa shifts back to the side of the specimen where it should be. The fact that both the nodal and element stress plots yield the same stress distribution indicates that the suspect elements were successfully removed and that the remaining model can now be used to compute the effective sizes. Hence, it is the model shown in Fig. 3 that was utilized to compute the effective area and effective volume for the C-sphere specimen. Additionally, for Si_3N_4 C-spheres with the geometry shown in Fig. 1, the relationship between compressive load and outer-fiber maximum tensile stress can be determined from this model as well and is shown in Fig. 4.

Efforts are underway to validate predicted stresses from the model with experimentally produced stresses. Photo-stimulated luminescence spectroscopy (PSLS) was used with a compressively loaded alumina C-sphere to measure mean hydrostatic stress at the outer-fiber. The outer fiber tensile stress gradient is shown in Fig. 5 and compared to that predicted from the C-sphere FEA model. Predicted 1st Principal stress is expected to be higher than average hydrostatic stress for a given location, so this observed trend is not surprising. Comparison of predicted pressures is underway and that result will enable a fairer comparison of stress with experimental PSLS values. Additionally, a strain-gaged specimen is under preparation.

The effective area and effective volume as function of Weibull modulus for the C-sphere flexure strength specimen are shown in Fig. 6. The effective sizes were computed using the following equations [11]:

$$A_e = \left(\frac{\sigma_o}{\sigma_e}\right)^m \ln\left(\frac{1}{1-P_f}\right) \tag{1}$$

$$V_e = \left(\frac{\sigma_o}{\sigma_e}\right)^m \ln\left(\frac{1}{1-P_f}\right) \tag{2}$$

where A_e is the effective area, V_e is the effective volume, s_0 is the scale parameter, m is the Weibull modulus, s_e is the maximum effective stress (computed by CARES/Life[1]), and P_f is the probability of failure (also computed by CARES/Life). The effective sizes are independent of the scale parameter since they only vary with geometry, loading, and the Weibull modulus.

NBD200 and SN101C balls with 12.7 mm diameter were machined[2] into C-sphere flexure strength specimens (Fig. 7). Manufacturer[3] reported properties for these two Si_3N_4 grades are shown in Table 1 and microstructural images of both are shown in Fig. 8. Elastic properties of the two materials were measured with Resonant Ultrasound Spectroscopy [analysis method described in Ref. 12] and found to be close to the manufacturer's reported values (Fig. 9). The static and dynamic hardnesses of both materials were recently quantified [13].

C-sphere flexure specimens were monotonically and compressively loaded to failure using an electromechanical universal testing machine[4] at a crosshead displacement rate of 0.5 mm/min. A special jig was used to horizontally align the C-sphere slot prior to loading. Load to fracture was recorded and used to determine C-sphere flexure strength according to Fig. 4. Weibull strength distributions were determined using commercially available software[5]. Optical fractography was conducted on all specimens to identify failure location and the fracture surfaces of a select few specimens were examined with scanning electron microscopy.

---

[1] NASA Glenn Research Laboratory, Cleveland, OH.
[2] Bomas Machine Specialties Inc., Somerville, MA.
[3] Saint-Gobain Ceramics, East Granby, CT.
[4] Instron Corp, Canton, MA.
[5] WeibPar, Connecticut Reserve Technologies, Cleveland, OH.

Table I. Manufacturer reported information for the two tested Si_3N_4 materials [www.cerbec.com].

Property	NBD 200	SN 101C
Sintering Aid	MgO	Y_2O_3 - Al_2O_3
Density (g/cm^3)	3.16	3.21
RT Flexure Strength (MPa)	> 900	> 1000
Weibull Modulus	> 15	> 25
Elastic Modulus (GPa)	320	310
Poisson's Ratio	0.26	0.27
Vickers Hardness, HV10	1550	1600
Fracture Toughness (MPa√m)	> 5.5	> 6.5

The C-sphere characteristic strength of the SN101C was approximately 20% higher than that for the NBD200 (805 MPa versus 670 MPa) while their Weibull moduli were statistically equivalent (5.9 and 7.2, respectively). This difference is illustrated in Figs. 10-11. Optical fractography showed that failure always initiated at the surface but not necessarily always right at the apex of the outer fiber (i.e., at zero position in Fig. 5). An example of one of those failure locations is shown in Fig. 12. According to the effective area dependence on Weibull modulus shown in Fig. 6, the effective area for the C-sphere specimen having a Weibull modulus between 5.9 and 7 is approximately 20 mm^2. As a comparison, the effective area for an ASTM C1161B bend bar [14] is approximately 100 mm^2 for the same range of Weibull modulus. For a hypothetical situation where the same surface-type strength-limiting flaw is operative in both specimen geometries, the characteristic strength of that bend bar geometry should be ~ 80% of the C-sphere or ~ 650 MPa for the SN101C and ~ 530 MPa for the NBD200.

Work is ongoing as to how to interpret the meaning of C-sphere strength and fractography and how that may be related to potential RCF performance. For a strength of 770 MPa, a fracture toughness of 6 MPa√m, and a crack geometry factor of 1.5, the estimated Griffith flaw size for the specimen shown in Fig. 13 would be approximately 30 microns. That is of the size scale that Hadfield [10] had indicated to be a critical size for crack penetration during RCF. Many parameters have been studied and measured, and attempts have been made to link them to RCF performance. Could this C-sphere strength be a more useful and relevant parameter for Si_3N_4 ball manufacturers? C-sphere development work continues at ORNL.

Miscellaneous

Wereszczak participated in the 2005 IEA Executive Committee Meeting held 11 October 2005 by giving three presentations that overviewed IEA Annex II efforts, IEA Annex III on rolling contact fatigue, and proposed a new annex on coating evaluation and performance. Participants from other US federal agencies (USDOE, NIST, NSF), Belgium, United Kingdom, China, Finland, Japan, Portugal, Australia, and Switzerland attended the IEA meeting. The mission of the IEA Implementing Agreement, past and present activities were overviewed, and its potential future was discussed among the participants. Wereszczak then attended COST 532 Conference on Triboscience and Tribotechnology on 12 October 2005.

Status of FY 2006 Milestones

Develop the C-sphere test coupon and its ability to exploit the characterization of subsurface damage in finished ceramic balls and link that damage to RCF performance. [09/06]
On schedule.

Communications/Visits/Travel

- Discussions with Mark Hadfield (Bournemouth University, UK) occurred regarding the RCF testing and characterization of bearing grade Si_3N_4's.
- Numerous discussions with Vimal Pujari (Saint-Gobain Advanced Ceramics, Northboro, MA) occurred regarding the RCF testing and characterization of their bearing grade Si_3N_4's.
- Wereszczak is planning on visiting Cerbec within the next few months. Additionally, the PI is planning to visit Bournemouth University (UK) in the 2nd quarter to discuss collaborative rolling contact fatigue work on silicon nitride.

Publications

- A. Wereszczak, W. Wang, O. M. Jadaan, M. J. Lance, and H. -T. Lin "Strength of a C-Sphere Flexure Specimen", submitted to the January 2006 Cocoa Beach conference.
- Y. Wang, M. Hadfield, W. Wang, and A. A. Wereszczak, "Rolling Contact Fatigue of Ceramics," in internal review, to be published as a DOE/ORNL Technical Memorandum.

References

[1] L. -Y. Chao and D. K. Shetty, J. H. Adair, J. J. Mecholsky, Jr., "Development of Silicon Nitride For Rolling-Contact Bearing Applications: A Review," *J. Mater. Educ.*, **17**, 245-303 (1995).

[2] L. Wang, R. W. Snidle, L. Gu, "Rolling Contact Silicon Nitride Bearing Technology: A Review of Recent Research," *Wear*, **246**, 159-173 (2000).

[3] Y. Wang and M. Hadfield, "Rolling Contact Fatigue of Ceramics," Vol. 11, Section 6E, ASM Handbook, 2002.

[4] H. I. Burrier, Jr., "Optimizing the Structure and Properties of Silicon Nitride for Rolling Contact Bearing Performance," *Trib. Trans.*, **39**, 276-285 (1996).

[5] J. Kang, M. Hadfield, and R. T. Cundill, "Rolling Contact Fatigue Performance of HIPed Si_3N_4 with Different Surface Roughness," *Ceram. Intl.*, **27**, 781-794 (2001).

[6] M. Ichikawa, T. Takamatsu, T. Matsuo, N. Okabe, and Y. Abe, "Ring Crack Initiation Load of Silicon Nitride Bearing Balls," *JSME Intl. J. A: Mech. Mat. Engrg.,* **38**, 226-30 (1995).

[7] R. T. Cundill, "Impact Resistance of Silicon Nitride Balls, pp. 556-61 in *Proc. 6th Intl. Symp. Ceram. Matls. Comp. Engines*, (1997).

[8] "Standard Specification for Silicon Nitride Bearing Balls," ASTM F 2094-03a, Vol. 01.08, ASTM International, West Conshohocken, PA (2004).

[9] B. A. Kschinka, S. Perrella, H. Nguyen, and R. C. Bradt, "Strengths of Glass Spheres in Compression," *J. Am. Cer. Soc.*, **69**, 467-72 (1986).

[10] M. Hadfield, "Failure of Silicon Nitride Rolling Elements with Ring Crack Defects," *Ceram. Intl.*, 24, 379-86 (1998).

[11] J. B. Wachtman, Mechanical Properties of Ceramics, John Wiley & Sons, New York, 1996.

[12] A. A. Wereszczak, "Elastic Property Determination of WC Spheres and Estimation of Compressive Loads and Impact Velocities That Initiate Their Yielding and Cracking," to be published in *Cer. Engrg. Sci. Proc.* (2006).
[13] H. Wang and A. A. Wereszczak, "Mechanical Responses of Silicon Nitrides Under Dynamic Indentation," *Cer. Engrg. Sci. Proc.,* **26**, 275-283 (2005).
[14] "Standard Test Method for Flexural Strength of Advanced Ceramics at Ambient Temperature," ASTM C 1161, Vol. 15.01, ASTM International, West Conshohocken, PA (2004).

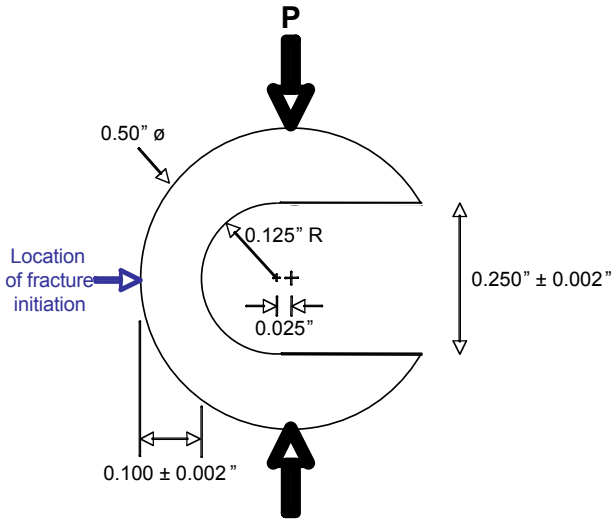

Figure 1. Schematic of the "C-Sphere" test specimen and its diametral compressive loading. Fracture will initiate at the outer surface and propagate radially inward.

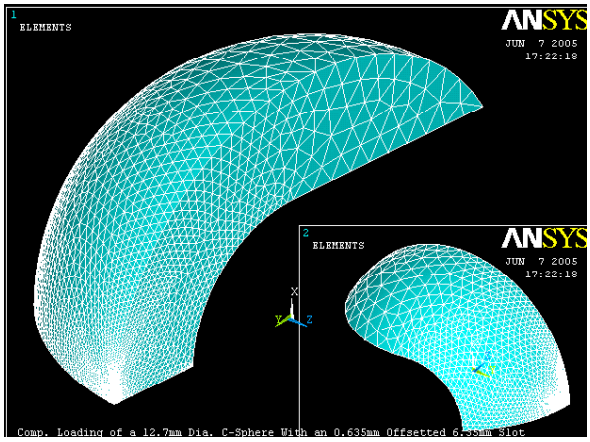

Figure 2. Mesh distribution for ¼ symmetry model of the C-sphere specimen, having 52703 elements and 76682 nodes.

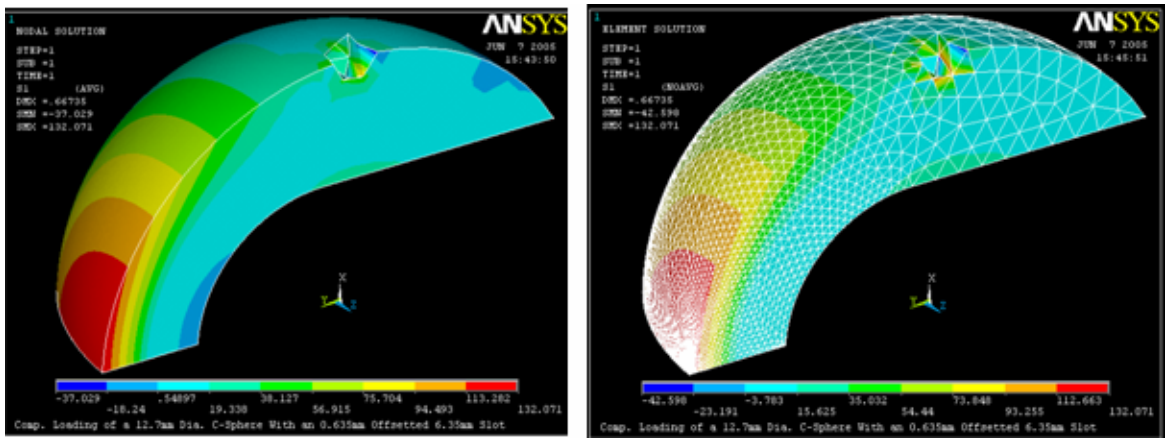

Figure 3. Nodal first principal stress distribution (left) and element first principal stress distribution (right) for the C-sphere specimen with the elements within the high stress concentration zone (under the load) carved out.

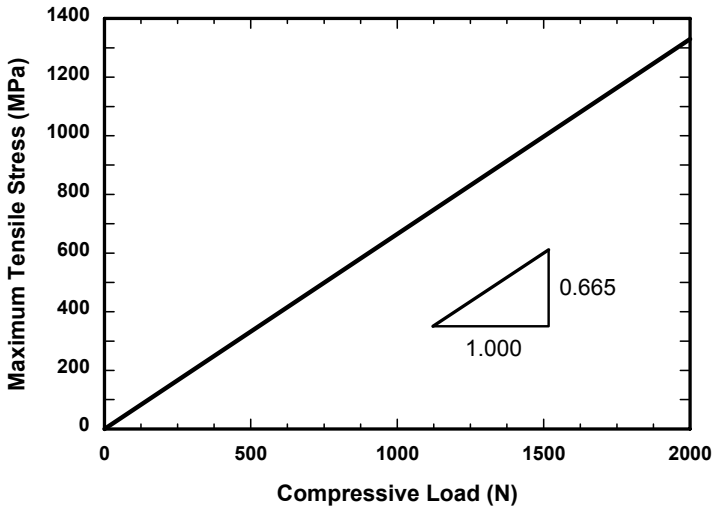

Figure 4. Maximum tensile stress (located at outer fiber shown in Fig. 1) as a function of diametral compressive load for the Si_3N_4 C-sphere geometry.

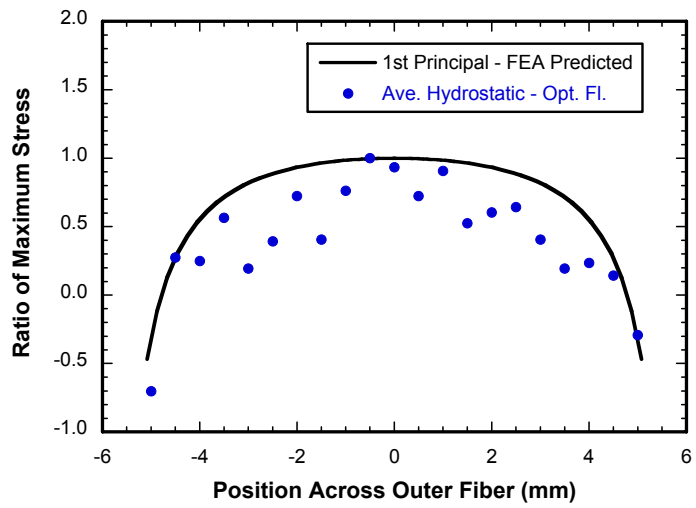

Figure 5. Comparison of predicted outer fiber stress and PSLS-measured average hydrostatic stress. Predicted 1st Principal stress is expected to be higher than average hydrostatic stress for a given location, so this observed trend is not surprising.

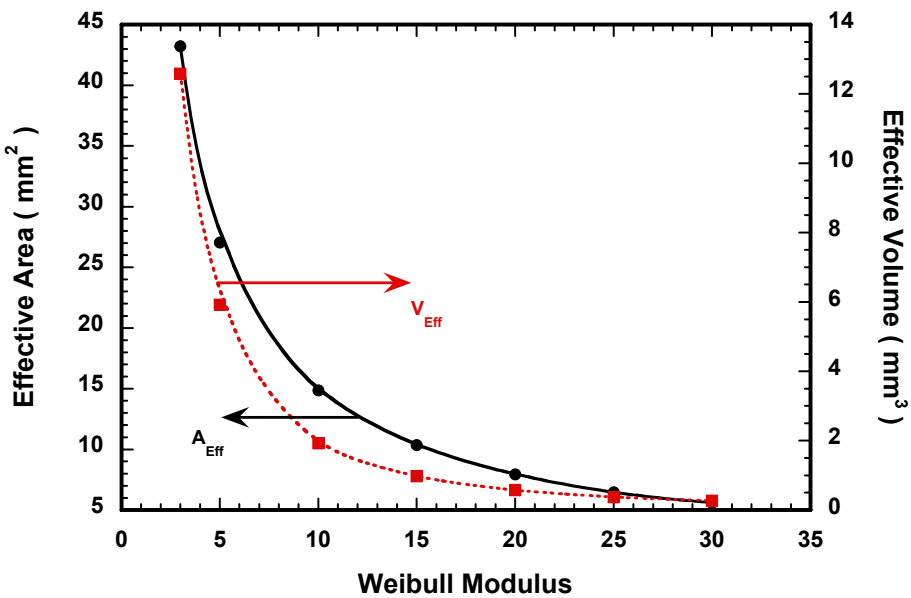

Figure 6. Effective area and effective volume as a function of Weibull modulus for the C-sphere flexure strength specimen.

Figure 7. Si_3N_4 C-sphere flexure strength specimens.

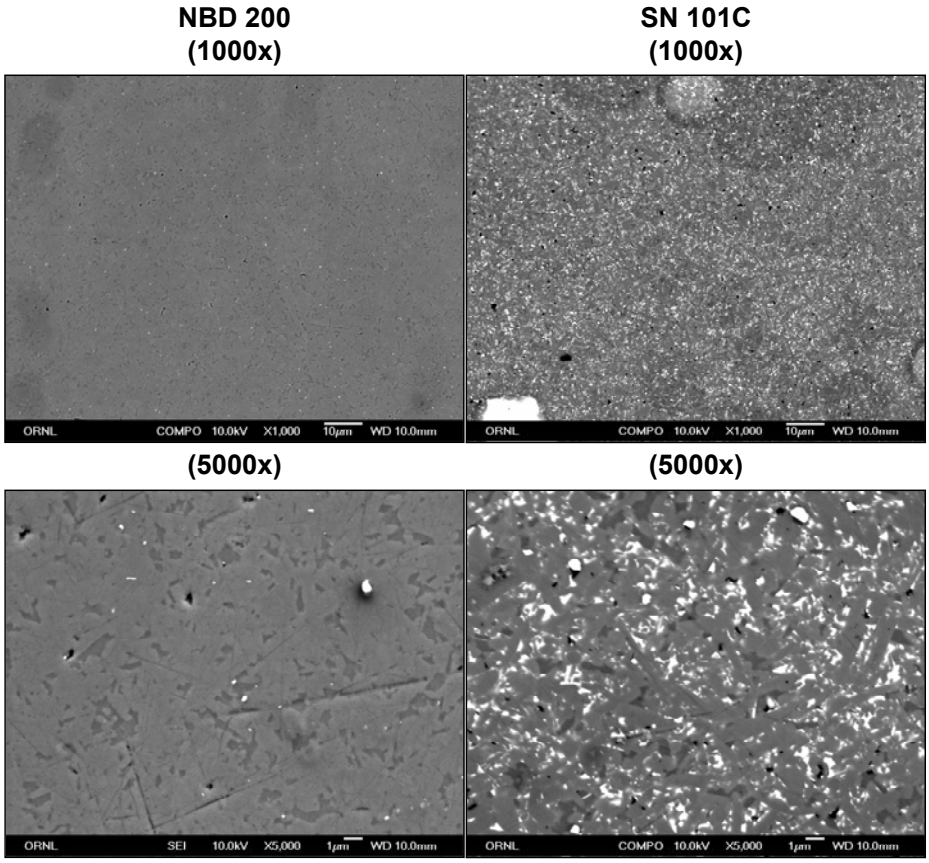

Figure 8. BS-SEM microstructure on finished ball surfaces of NBD200 and SN101C.

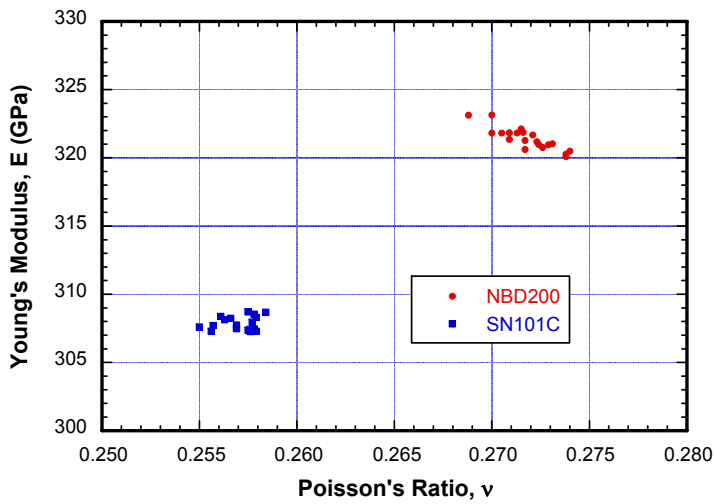

Figure 9. Elastic properties of NBD200 and SN101C measured using Resonance Ultrasound Spectroscopy.

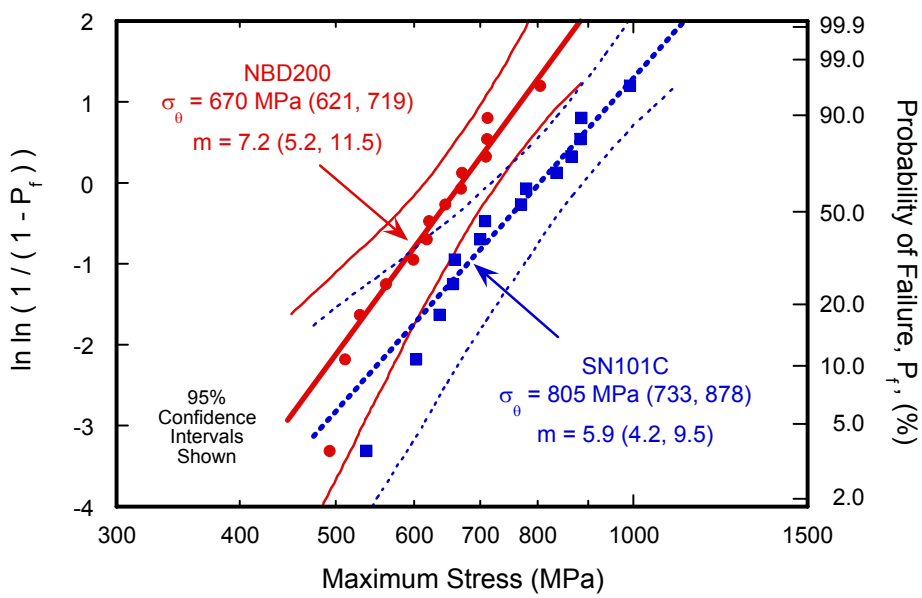

Figure 10. C-sphere Weibull strength distribution comparison of NBD200 and SN101C.

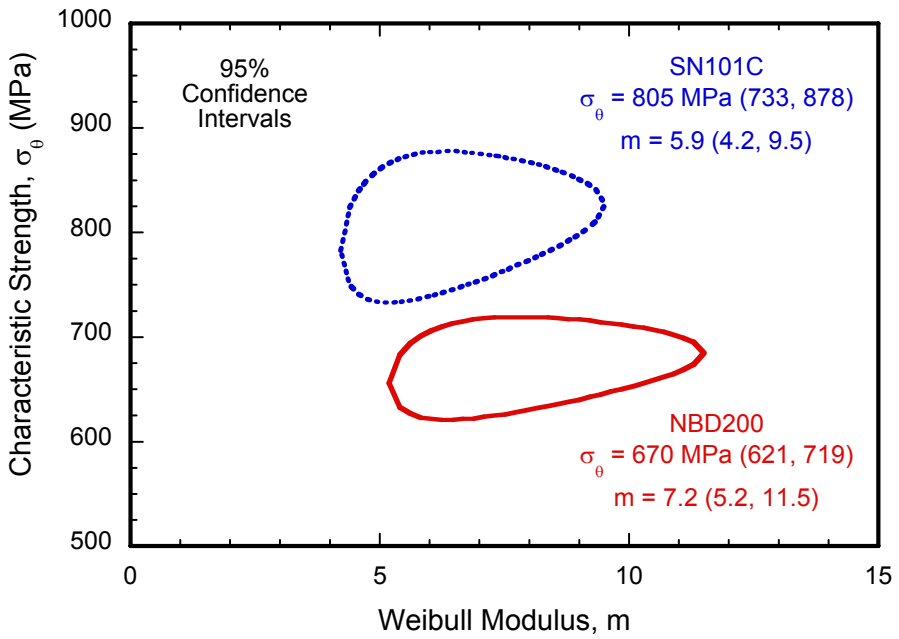

Figure 11. 95% confidence ratio ring comparison of NBD200 and SN101C C-sphere strengths.

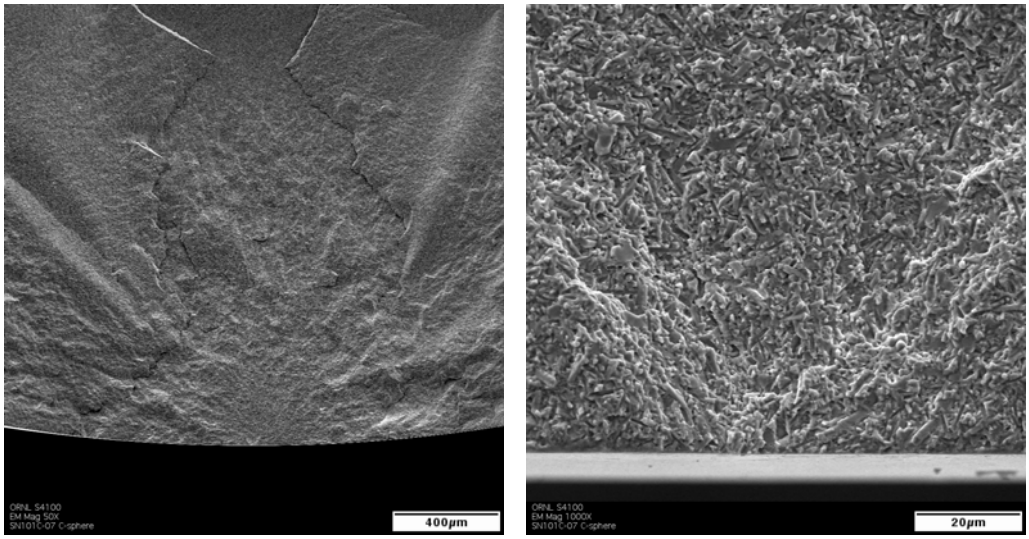

Figure 12. Example of a surface-located strength-limiting flaw in a SN101C C-sphere flexure strength specimen. This specimen had a strength of 770 MPa.

Mechanical Characterization – Nanoengineered Matereials

J. Sankar, Z. Xu, G. Rajaram and S. Yarmolenko
North Carolina A & T State University

Objective/Scope

To use the optimization technique to study the properties of the solid oxide fuel cell (SOFC) anode material.

Task

Develop a design matrix to fabricate the anode material with different ratios of the raw materials and different sintering temperatures. The obtained anode material will be used for porosity and conductivity studies.

Technical Highlights

A solid oxide fuel cell is an energy conversion device that produces electricity by electrochemically combining fuel (from anode) and oxidant (from cathode). The two most common designs of SOFCs are the tubular and the planar [1]. Planar cells are capable of generating high power densities in comparison with the tubular cells. Anode supported planar cells provide very high cycle efficiency and pollution free energy. However, the microstructure of the cell degrades with respect to time due to the high temperature operating conditions. This leads to the deterioration of the fuel cell [2] and subsequent decomposition. This problem causes the major concern towards the commercialization of the fuel cells. The current study was to improve the life and performance of the anode cell for the SOFCs in a long run. In the earlier studies, Muller *et al*. [3] and Lee *et al*. [4] did extensive studies on the porosity and the electrical measurements for anode material with varying proportions of size and mol. % of the raw materials and the sintering temperature. Takehisa *et al.* [5] have used varying sizes of NiO-YSZ composite particles to fabricate a porous anode structure. Clemmer *et al.* [6] have observed dramatic improvements in electrical conductivity with increase in Ni content. Lee *et al.* [7] have investigated the effect of microstructure on anode substrate on the unit cell performance. However, the earlier investigators have studied the effect of individual process variables on the performance of the anode material. It is imperative to consider all the contributing factors that affect the anode material performance. So, it was decided to use the statistical method to study the individual effects and the combined effects of the different processing parameters on the output variable.

The anode material was prepared by mixing the raw materials (graphite, NiO and YSZ) in different proportions, compacted uniaxially, sintered in air and finally reduced in H_2/Ar atmosphere. The graphite powder ratios and sintering temperatures used for the fabrication is shown in the Table 1. The NiO/YSZ ratio was 57.5/42.5 and the compaction pressure was 150 MPa. The sintered samples were reduced at 1000 °C. The different powder ratios, compaction pressure, the sintering temperatures and the reduction temperature were decided based on the literature. The different powders used were mixed together using ball milling technique. The die used for powder compaction was half-inch steel die. The measured output variables were porosity and the electrical conductivity.

Table 1. Composition and process parameters used for the experimental design

Independent variable	Treatment level		
	0 Low	1 Medium	2 High
Graphite volume fraction (vol. %)	30	35	40
Sintering temp (°C)	1200	12500	1350

Results and Discussion

The different powders (NiO, YSZ and graphite) were weighed based on the volume calculation and mixed together for homogeneity using the horizontal ball milling. The graphite was used to obtain the desired porosity. The ball milled mixture was weighed for individual samples and then poured into the half inch steel die for powder compaction. The green samples were sintered in air for one hour at the maximum temperatures. Finally, in order to reduce to NiO into Ni, the electrically conductive material in the anode cell, the sintered samples were placed in the reduction furnace under 4% H_2/Ar atmosphere at 1000 °C for one hour. The reduced samples were used for the porosity calculations and conductivity measurements. The porosity calculations were based on the weigh and size measurements of the sample followed by the actual and the theoretical volume calculations. The four-point probe method was used for the conductivity measurements. The porosity and the conductivity results are shown in the Table 2. For each sample, three replicates were used and the results shown were averaged to one value.

Table 2. Porosity and the Conductivity results for the different processing conditions

Sintering Temp (°C)	Graphihte Vol. %	Porosity Vol. %	Conductivity (Ω^{-1} cm^{-1})
1200	30	56.06	69.59
	35	56.85	69.27
	40	58.96	58.53
1250	30	52.53	147.99
	35	55.41	94.39
	40	57.66	81.70
1350	30	41.35	744.87
	35	37.08	686.19
	40	41.01	733.46

The results show that the sintering temperature was the major variable that controls the porosity and the conductivity of the cell. Graphite content also had a role in controlling the porosity but it mostly depends on the sintering temperature values. Both graphite and the sintering temperature almost had a linear effect on the porosity and the conductivity values (Fig 1). For the samples sintered at 1200°C, with 30 vol. % of graphite content, the porosity value was 56.06 and for 40 vol. % of graphite content, the porosity was 58.96. But the porosity and the conductivity values had an inverse effect for the given sintering temperature. The reason was, the graphite oxidizes at lower temperature (~ 1000°C) compared to the maximum temperatures used and it directly leads

to the formation of pores. So the difference in the graphite vol. % had some effect on the pore volume at the lower temperature sintering (i.e., at 1200°C). But at 1350°C, the difference in the graphite volume did not make much of a difference in the porosity volume. This was because of the fact that at higher sintering temperature, the particle growth and particle fusion started taking place and it leads to reduced porosity and improved inter-particle connectivity. This replicates on the conductivity of the cell. At lower sintering temperatures, the inter particle connectivity was poor and that leads to poor electrical charge carrying paths. Whereas, at higher sintering temperature, the conductivity increases drastically due to the fact that it has more electron conducting path. Thus, the conductivity and the porosity values obtained for the samples sintered at 1350°C were more suitable for the SOFC application.

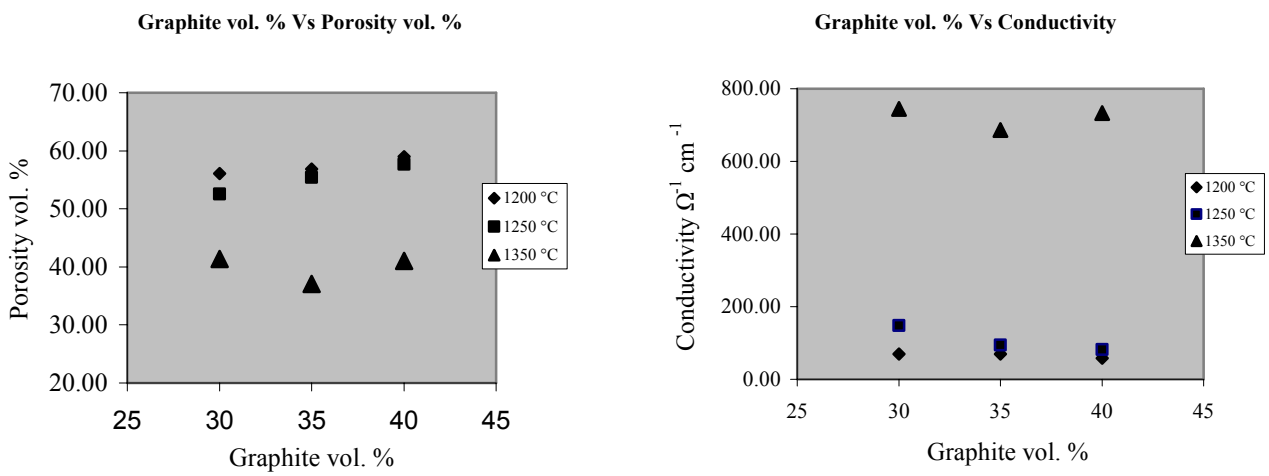

(a) b)

Figure 1. (a) Comparison of porosity values for different sintering temperatures (b) Comparison of Conductivity values for different sintering temperatures

Conclusions

The design matrix was developed and successfully used to develop the anode material for SOFC application. The results showed that the processing variables and their levels had a strong impact on the output variables. The porosity values had a controlling effect on the conductivity values. It indicates that the electrode performance can be optimized by controlling the porosity in order to achieve desired conductivity. The current work sparkle the idea of changing the ratios of NiO in the mixture to study the changes in conductivity values and also in the microstructure of the electrode.

References

1. Singhal, S.C. (2002). Solid oxide fuel cells for stationary, mobile and military applications. Solid State Ionics, 152-153: 405-410.
2. Jorgensen, M.J., Holtappels, P. and Appel, C.C. (2000). Durability test of SOFC cathodes. Journal of Applied Electrochemistry, 30: 411-418.
3. Muller, A.C., Herbstritt, D. and Tiffee, E.I. (2002). Development of a multilayer anode for solid oxide fuel cells. Solid State Ionics. 152-153: 537-542.

4. Lee, J.-H., Moon, H., Lee, H.-W., Kim, J., Kim, J.-D., and Yoon, K.-H (2002). Quantitative analysis of microstructure and its related electrical property of SOFC anode, Ni – YSZ cermet. Solid State Ionics, 148: 15-26.
5. Takehisa Fukui, Murata, K., Ohara, S., Abe, H., Naito, M., and Nogi, K. (2004). Morphology control of Ni-YSZ cermet anode for lower temperature operation of SOFCs. Journal of Power Sources, 125: 17-21.
6. Clemmer, R. M. C, Corbin S. F, (2004). Influence of porous composite microstructure on the processing and properties of solid oxide fuel cell anodes. Solid State Ionics, 166: 251-259
7. Lee, J. H., Heo J. W., Lee, D. S., Kim, J. Kim, G. H., Lee, H. W., Song, H. S., and Moon, J. H. (2003) The impact of anode microstructure on the power generating characteristics of SOFC, Solid State Ionics, 158: 225-232.

Communications/Visitors/Travel

None

Problems Encountered

None

Nanocrystalline Materials via Machining

S. Chandrasekar, K. P. Trumble, and W. D. Compton
Purdue University

Objective/Scope

Work continued on low-temperature consolidation routes for ultrafine-grained alloy particulate produced by machining. The focus this quarter was on powder deformation and polymer bonding routes. Work also continued on machining of precipitation-hardened alloys in the solution-treated condition as a means of achieving higher levels of thermal stability. The original work on aluminum alloys has been extended to titanium and a nickel-based superalloy.

Technical Highlights

Low-temperature consolidation

Additional consolidation trials via powder extrusion were conducted using nanostructured Al 6061-T6 and OFHC copper particulates. Densification and bonding in these specimens are currently being evaluated. A related study of room temperature flat-rolling aluminum-canned 6061-T6 machining chip particulate was also completed. A high degree of densification was achieved and significant interparticle bonding occurred when pure aluminum powder was blended with the alloy powder, as in direct extrusion. Mechanical properties evaluations of these materials are in progress. We are anxiously awaiting the results of extrusion trials initiated last summer in the Materials Processing Lab at ORNL, where a larger press will enable thick-canned samples to be extruded with much higher stress than we can currently achieve.

Earlier work on epoxy-bonding of Al-6061-T6 chip particulate by die pressing pre-mixed epoxy/particulate mixtures was extended to pressure infiltration of epoxy after die pressing the dry particulate to different relative densities. This enabled pressures up to 210 MPa to be imposed on the epoxy, compared to only atmospheric pressure (0.1 MPa) in the earlier route. Figure 1 shows the microstructure after 210-MPa infiltration of a preform pressed at 800 MPa (relative density 0.92). Prior particle boundaries are just visible and pockets of epoxy in larger prior pores indicate good penetration. Density measurements, however, indicated 5 vol. % porosity, most likely due to closed pores in the preform. Hardness measurements revealed a primary effect of the metal relative density with Vickers hardness of 120 ± 20 kg/mm^2 for the highest metal density. In comparison, the starting chip particulate has a hardness of about 150 kg/mm^2 and that of the bulk 6061-T6 alloy before machining 107 kg/mm^2. Even though this structure is still not completely optimized, progress is sufficient that larger specimens will be produced for tensile testing.

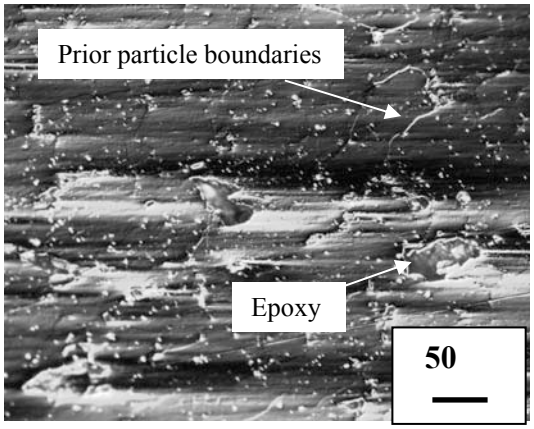

Figure 1. Optical micrograph showing epoxy-bonded Al-6061-T6 chip particulate produced by infiltrating a 0.92 dense preform at 210 MPa applied pressure (isostatic).

Highly-Stable Nanostructured (HSN) Alloys

Another avenue of investigation has focused on creation of high-strength, high-temperature nanostructured materials such as titanium and nickel-based alloys, with exceptional thermal stability of the microstructure. In this context, we have demonstrated a means of extending the temperature range for structural applications of nanomaterials through the introduction of a dispersion of second phase precipitates, whose thermal stability determines the temperature at which the strength deteriorates. Precipitate-stabilized nanostructured materials synthesized from solution-treated Inconel 718 are shown to be extremely stable and hard even after prolonged heat treatment for 500 hours at temperatures as high as one-half of the melting point; we designate them as "Highly-Stable Nanostructured (HSN) materials." The enhanced thermal stability of the material's strength results from retention of both the fine microstructure and the fine precipitate phase coexisting at the high temperatures. This novel microstructure was created by first deforming solution-treated Inconel 718 to a large shear strain by machining, followed by thermal ageing of the chip to create fine-scale precipitates. The microstructure evolution as a function of strain is being characterized together with measurements of mechanical properties on large nanostructured chip samples created by machining. The mechanical properties are being measured using uni-axial tension test and will provide an estimate of maximum realizable strengths in bulk samples fully consolidated from machining chips.

Problems Encountered

None

Status of Milestones

"Evaluate a range of consolidation and densification routes that enable bulk monolithic and composite materials to be produced from nanostructured machining chip particulate without significant coarsening." On schedule.

Publications

1) S. Swaminathan, M. Ravi Shankar, S. Lee, J. Hwang, A.H. King, R.F. Kezar, B.C. Rao, T.L. Brown, S. Chandrasekar, W.D. Compton and K.P. Trumble, Large Strain Deformation and Ultra-Fine Grained Materials By Machining, *Materials Science and Engineering* A, **410-411**, 358-363, 2005.

2) M. R. Shankar, S. Chandrasekar, A. H. King, W.D. Compton, Microstructure and Stability of Nanocrystalline Aluminum Created by Large Strain Machining, *Acta Materialia,* **53**, 4781-4793, 2005.

3) M. Ravi Shankar, S. Chandrasekar, W.D. Compton and A.H. King, Characteristics of Aluminum 6061-T6 Deformed to Large Strains by Machining, *Materials Science and Engineering A*, **410-411**, 364-368, 2005.

Visitors

Visitors to the lab in the first quarter of FY06 for research discussions on findings related to the project included Dr Paul Becker from ORNL/UTenn, Sam Truesdale from Rolls Royce Corporation, Indianapolis, IN, Bob Bondaruk from the Air Force Propulsion Environmental Working Group, Dayton, OH, and Dr PinYang and colleagues from the Sandia National Labs, Albuquerque, NM.

Student Graduated

Srinivasan Swaminathan successfully completed his PhD thesis in December on creation of nanostructured solid solutions by large-strain machining.

Deformation Processes for the Next Generation Ceramics

Paul F. Becher
Oak Ridge National Laboratory

Objective/Scope

In addition to lower specific weight, ceramics have a number of attractive properties for application as components in various heavy vehicle systems such as electrochemical properties needed to develop advanced sensors and wear resistance and low coefficients of friction to increase life in moving components. Significant new opportunities are beginning to evolve with the advent of nanocrystalline materials. Initial findings show that nanocrystalline ceramics have substantially improved electrochemical properties, which are being explored in sensors for combustion and emissions controls, and auxiliary power sources. Studies have also revealed that ceramics with grain sizes < 100 nanometers can exhibit very high hardness, which may translate to greater wear resistance either in the form of coatings or components (e.g., for valve train components) or to create low friction surfaces to enhance engine performance.

The goal being to develop the technology to form "green" (unfired) bodies of nanocrystalline particles to allow one to devise pressureless sintering profiles to produce dense monolithic bodies with grain sizes < 100 nm. This is aimed at finding approaches to produce sizeable monolithic bodies for subsequent evaluation. The second thrust focuses on the mechanical and wear behavior of nanocrystalline ceramics and the influence of external parameters (e.g., stressing rate, temperature, environment (e.g., air, vacuum), and electric fields (in collaboration with researchers at North Carolina State University) on the plastic deformation behavior.

Technical Highlight

The deformation studies carried out in conjunction with Prof. Conrad at North Carolina State University indicate that electric field effects on the onset of deformation may be influenced by the sign of the applied stress (i.e., greater in tension than in compression). To this point, the current electric field effect studies have been conducted using compression testing. Currently, samples are being prepared for tensile tests to test this hypothesis. The changes in funding will slow progress towards this end. Super plastic flow was shown to occur under compression loading; under these conditions cavitation may be substantially suppressed. Characterization studies will be conducted to assess the cavitation behavior.

Status of Milestones

New project

Communications/Visits/Travel

Continued weekly teleconferences with Prof. Jim Adair, Pennsylvania State University, to discuss processing of nanocrystalline ceramics. Discussion have been held with Prof. Hans Conrad of North Carolina State University on how the sign of the applied stress can influence the electric field effects on the onset of plasticity in ceramics.

Publications

None